Design of Cavitating Propeller Blades in Non-Uniform Flow by Numerical Optimization

by

SHIGENORI MISHIMA

B.S., The University of Tokyo (1986)
M.S., The University of Tokyo (1988)

Submitted to the Department of Ocean Engineering
in partial fulfillment of the requirements for the degree of

Doctor of Philosophy

at the

MASSACHUSETTS INSTITUTE OF TECHNOLOGY

September 1996

Author .....
Department of Ocean Engineering
June 30, 1996

Certified by .....
Spyros A. Kinnas
Assistant Professor
Department of Civil Engineering, The University of Texas at Austin
Thesis Supervisor

Accepted by .....
A. Douglas Carmichael
Chairman, Departmental Committee on Graduate Students

Design of Cavitating Propeller Blades in Non-Uniform Flow by Numerical Optimization

by

SHIGENORI MISHIMA

Submitted to the Department of Ocean Engineering
on June 30, 1996, in partial fulfillment of the
requirements for the degree of
Doctor of Philosophy

Abstract

High-speed propulsor blades often experience moderate to substantial amounts of unsteady cavitation, and up to now have been designed via design methods for non-cavitating blades combined with methods for the analysis of cavitating flows in a trial-and-error manner.

In this thesis a numerical non-linear optimization algorithm is developed for the *automated, systematic design* of cavitating blades. The objective and constraint functions in the optimization process are expressed in terms of the design variables via linear approximations of the results from an existing lifting-surface analysis method, in the first stage of the algorithm, and quadratic approximations in the final stage. In this way the number of required geometries to be analyzed and the associated computational effort are minimized. The developed methodology is implemented in a modular manner so that future improvements in the modeling of cavitating flows can be readily incorporated. The proposed algorithm is validated with several known non-linear optimization test problems.

The method is first applied to the design of efficient two-dimensional partially and supercavitating hydrofoil sections and the results are compared to those from a previously developed optimization procedure.

Then, the method is applied to the design of propeller blades in uniform flow. The blade mean camber surface is defined via a cubic B-spline polygon net in order to facilitate the handling of the geometry, and to reduce the number of the design parameters. Non-cavitating blade geometries designed by the present method are directly compared to those designed via an existing lifting-line/lifting-surface design approach.

Finally, the optimization algorithm is applied to the design of cavitating blades in *non-uniform* flow. The objective of the design is to obtain maximum propeller efficiency for given conditions by allowing *controlled* amounts of sheet cavitation. Several constraints on the *unsteady* cavity characteristics, such as the area of cavity planform and the amplitudes of the cavity volume velocity harmonics, are incorporated in the optimization technique. The effect of the constraints on the efficiency of the propeller

design is demonstrated with various test cases.

Thesis Supervisor: Spyros A. Kinnas
Title: Assistant Professor
Department of Civil Engineering, The University of Texas at Austin

Acknowledgments

There are a lot of contributions from many people to this thesis work. I first would like to express my greatest possible gratitude to my thesis supervisor, Professor Spyros Kinnas, at the University of Texas at Austin. He has always been encouraging me and giving me invaluable advices in every situation, even on weekends. I got several pieces of email every week from him and I knew he cared about my work. This pushed me to keep working hard. His contribution is so large that I almost feel as if he were a co-author of this thesis.

I would also like to thank my "step" supervisor at MIT, Professor Jake Kerwin, for his insightful and friendly advices on both good (rarely) and bad (mostly) results. He made comments always in a humorous way. I sometimes didn't realize the funny point until Todd Taylor explained it for me.

Professor Dimitris Bertsimas of the Sloan School of Management accepted to become a member of my thesis committee as an expert in optimization. He attended all the committee meetings and gave many useful comments from an optimization point of view, which I would have missed without him.

Dr. Ki-Han Kim of DTMB traveled all the way from Washington D.C. sometimes via Minneapolis to MIT and provided many practical suggestions, which I believe made this thesis more valuable.

I was really lucky to get to know smart Propnut members: Dr. Dave Keenan, Dr. Charlie Mazel, Dr. Ching-Yeh Hsin, Dr. Neal Fine, Dr. Mike Hughes, Dr. Tatsuro Kudo, Ms. Beth Lurie, Mr. Todd Taylor, Mr. Scott Black, Mr. Bill Milewski, Mr. Cedric Savineau, Mr. Wes Brewer, Dr. Bill Ramsey, Mr. Rich Kimball, Mr. Gerard Mchugh, Ms. Dianne Egnor, and Ms. Barbara Smith. Weekly group meetings were very helpful to get useful hints in my own research and to know other researches that were going on.

Bill Milewski took time to review my thesis draft and gave me good suggestions on it.

Dr. Takashi Maekawa has been a good friend and I enjoyed talking with him over

lunch.

Mr. Tatsuo Mori and Mr. Hideki Shimizu deserve credit for their friendship with me.

I would like to thank my former supervisors at the University of Tokyo, Professors Koichiro Yoshida, Hiroharu Kato, and Hideyuki Suzuki for their encouragements.

Professor Toshikazu Murakami of Tokai University is the person who made me consider studying at MIT, without whom I wouldn't even have started hydrodynamics research.

Special thanks go to my host family, Dr. and Mrs. Seigo Matsuda, who made my stay in Boston always much easier and more enjoyable.

Finally I would like to thank my wife, Naomi, for everything. I owe too much to her.

Much of the computation was performed remotely on "cavity", a DEC Alpha 600(5/266) computer of the Ocean Engineering Group in the Department of Civil Engineering at the University of Texas at Austin.

This research was supported by an international consortium of the following companies and research centers: Daewoo Heavy Industries Ltd., David Taylor Model Basin, El Pardo Model Basin, Hamburg Ship Model Basin, Hyundai Heavy Industries Co., Ltd., Ishikawajima-Harima Heavy Industries Co., Ltd., KaMeWa AB, Mercury Marine, Michigan Wheel Corporation, Outboard Marine Corporation, Rolla SP Propellers SA, Sulzer-Escher Wyss GmbH, Ulstein Propeller AS, Volvo-Penta of the Americas, and Wärtsilä Propulsion

Financial support for my stay at MIT was provided by the Technical Research & Development Institute, Japan Defense Agency.

Contents

List of Figures

List of Tables

NOMENCLATURE

c	blade section chord length
$\boldsymbol{c}$	penalty parameter vector
C_f	frictional drag coefficient
C_D	drag coefficient : $= D/(0.5\rho U_\infty^2 c)$
C_D^i	inviscid cavity drag coefficient
C_D^v	viscous drag coefficient
C_L	lift coefficient : $= L/(0.5\rho U_\infty^2 c)$
C_p	pressure coefficient : $= (p - p_\infty)/(\rho n^2 D^2)$
$\boldsymbol{d}$	search direction in the quasi-Newton method
$\boldsymbol{d}$	B-spline control point (vertex)
D	propeller diameter
D	sectional drag
$\boldsymbol{D}$	positive definite matrix
$\boldsymbol{e}_i$	unit vector whose i-th element is 1
$f(\boldsymbol{x})$	objective function for the minimization problem
f	blade section camber
f_o	maximum camber
F	objective function for the *unconstrained* minimization problem
F_n	Froude number : $= n^2 D/g$
g	accelaration of gravity
$g_i(\boldsymbol{x})$	i-th inequality constraint for the minimization problem
G	nondimensional circulation : $= \Gamma/(2\pi R V_s)$
$\boldsymbol{G}$	gradient vector
h	cavity height
h_{10}	cavity height at 10% from the leading edge of the foil
$h_i(\boldsymbol{x})$	i-th equality constraint for the minimization problem
$\boldsymbol{H}$	Hessian matrix
$\boldsymbol{I}$	identity matrix
J_s	advance coefficient based on ship speed : $= V_s/(nD)$

k	order of B-splines
K_T	thrust coefficient : $= T/(\rho n^2 D^4)$
K_{T0}	required thrust coefficient
$\bar{K}_T$	circumferential mean K_T
K_Q	torque coefficient : $= Q/(\rho n^2 D^5)$
$\bar{K}_Q$	circumferential mean K_Q
l	cavity length
l	number of equality constraints
L	sectional lift
$\mathcal{L}$	augmented Lagrangian penalty function
m	number of inequality constraints
n	number of design variables
n	propeller rotational speed
$N_{i,k}$	i-th B-spline basis of order k
N_u	number of chordwise B-spline vertices
N_w	number of spanwise B-spline vertices
p	pressure on the blade
p_{shaft}	pressure at the propeller shaft far upstream
p_v	vapor pressure
p_∞	pressure at infinity
P	propeller pitch
$P_{0.7}$	propeller pitch at $r/R = 0.7$
$\boldsymbol{P}$	point in space defined by B-splines
Q	propeller torque
r	radial coordinate
r	spanwise spacing required by *HPUF-3A*
r_h	propeller hub radius
R	propeller radius
R_{uw}	radius of the ultimate wake
Re	Reynolds number : $= U_\infty c/\nu$

$\mathcal{R}^n$	n-dimensional Euclidean space
s	non-dimensional chordwise coordinate
s	chordwise spacing required by *HPUF-3A*
$\boldsymbol{s}$	slack variable vector for converting inequality constraints to equality constraints
t	knot vector for B-splines
t	blade section thickness
t_o	maximum thickness
T	propeller thrust
T	B-spline knot sequence
u	chordwise parameter for B-splines
$\boldsymbol{u}$	Lagrange multiplier vector corresponding to the inequality constraints
U_∞	inflow velocity
$\boldsymbol{v}$	Lagrange multiplier vector corresponding to the equality constraints
V	cavity volume
V_s	ship speed
w	spanwise parameter for B-splines
x	propeller rake
$\boldsymbol{x}$	design variable vector
$\bar{\boldsymbol{x}}$	optimum solution vector
Z	number of propeller blades
z_{min}	minimum section modulus of the foil
α	angle of attack
α	step length in the quasi-Newton method
Γ	circulation
δ	maximum allowed change of design variables at each iteration
ε	tolerance for convergence
η	propeller efficiency: $= (J/2\pi)(K_T/K_Q)$
θ	propeller skew
θ	propeller angle

λ	perturbation of each variable for the initial linear approximation of the functions
μ	viscosity of the fluid
ν	kinematic viscosity $= \mu/\rho$
ρ	fluid density
σ	cavitation number based on inflow : $= (p_\infty - p_v)/(0.5\rho U_\infty^2)$
σ_n	cavitation number based on propeller rotational speed : $= (p_{shaft} - p_v)/(0.5\rho n^2 D^2)$
ϕ	propeller pitch angle
ϕ_{tw}	pitch angle of the transition wake
ϕ_{uw}	pitch angle of the ultimate wake
Φ	parameter for constructing initial B-spline polygon net
ω	propeller angular velocity
SK	skew at the tip
CA	maximum back cavity area / blade area
FA	maximum face cavity area / blade area
VV	blade rate cavity volume velocity harmonics / nR^3
SKMAX	allowable maximum skew at the tip
CAMAX	allowable maximum back cavity area / blade area
CAMAX	allowable maximum face cavity area / blade area
VVMAX	allowable maximum blade rate cavity volume velocity harmonics / nR^3
CAVOPT-3D	CAVitating propeller design OPTimization program
HPUF-3A	cavitating Propeller Unsteady Force analysis program (with Hub effect) by a vortex-lattice method [47]
PBD-10	non-cavitating Propeller Blade Design program in steady flow by a vortex-lattice method [25]
PLL	Propeller blade design program by a vortex-lattice Lifting Line method [10]

Chapter 1

Introduction

Cavitation has always been a major concern to the propeller designers and researchers mainly because of its undesirable nature. In most applications, marine propellers operate in a spatially non-uniform flow field behind the hull of an ocean vehicle. This non-uniformity causes periodic growth and collapse of cavities which result in cyclic pressure fluctuation on the hull and vibratory forces on the propeller shaft. When the cavity collapses, extremely high pressures arise either in the vicinity of the trailing edge of the blade or on other hydrodynamic devices (e.g. rudder) downstream of the blade. These pressures can often lead to pitting and serious erosion on the propeller blade. In addition, excessive fluctuating pressures on the hull may cause undesirable noise or even structural failure of the hull panels.

In the past, the propeller design philosophy has been to avoid cavitation for the widest possible range of operating conditions. However, the recent demands for higher ocean vehicle speeds and higher propeller loads have made this design philosophy practically impossible to achieve. The performance of a propeller designed to be cavitation free decreases appreciably once it starts cavitating. Most importantly, the efficiency of a non-cavitating high speed propeller is relatively low due to large frictional losses associated with the required large blade area.

The alternative is to allow for *controlled* amounts of *sheet* cavitation, which is less harmful than other types of cavitation, and design propellers with small blade area.

1.1 Objectives

The objective of this work is to develop a computationally efficient optimization method for the automated design of cavitating lifting surfaces. Analysis methods are used in a systematic way via coupling with a numerical optimization algorithm.

An important consideration in the course of development is to implement the methodology in a modular form so that upgrades in the analysis method or new design constraints can be readily incorporated.

1.2 Previous Research

1.2.1 Two Dimensional Section Design

Design of efficient two dimensional sections is required in many applications such as airplanes, hydrofoil crafts, and sailboat keels. Most of the current methods for the design of cavitating propellers are essentially based on the design of two dimensional cavitating blade sections.

The two dimensional design is usually performed by applying a two dimensional analysis method in a trial-and-error manner until the section with the "smallest" drag is found for the specified design condition, as in Kikuchi et al [36], Kamiirisa and Aoki [30], Vorus and Mitchell [73], and Ukon et al [69].

Tulin was the first to apply linearized cavity theory for the analysis [68] and systematic design [67] of supercavitating hydrofoils at zero cavitation number, by using a conformal mapping technique. He expressed the foil geometry (i.e. the pressure side of the supercavitating sections) and the foil lift and drag in terms of a Taylor series expansion. Optimum sections (i.e. sections with the highest lift to drag ratio) were determined by considering the first two or five terms in the Taylor series expansion. The two-term supercavitating sections are widely known as the *Tulin* sections, and the five-term sections as the *Johnson* [29] sections. These sections are optimum only in the limit of zero cavitation number.

Some design methods are based on charts, like those of Rutgersson [59], which

are obtained from systematic model tests on cavitating hydrofoils. This approach works well for design conditions, for which the charts are available. However, the applicability of the method is limited to geometries which are close to those in the charts.

A popular way of designing hydrofoil sections is the so called *inverse design method*, where a designer specifies the pressure distribution on the foil and solves for the foil geometry. This method has been applied for example to aerofoils in transonic flow by Giles and Drela[23], and to super-cavitating hydrofoils by Ukon et al[69]. However, it is difficult, especially in the case of cavitating hydrofoils, to know *a priori* the pressure distribution that leads to a desired global performance of the foil. As a result, this method relies highly on the designer's skill.

An alternative to the inverse design methods, is a numerical *optimization* technique used in combination with a flow analysis method, as described by Dulikravich[17]. The analysis method is used first to evaluate the characteristics of an initial foil geometry. Then, the optimization algorithm searches for an improved foil geometry, which meets all the specified requirements, using information provided by the analysis method. In most cases, analyzing the flow field is much more time consuming than the numerical optimization process. This is in particular true when the analysis method is based on computationally intensive Navier-Stokes equation solvers or coupled Euler and boundary layer equation solvers, like those implemented by Lee and Eyi [48], and Eyi et al [20], respectively. An efficient way of using an analysis code coupled with the optimization algorithm, is to approximate the foil characteristics from a relatively small number of runs of the analysis code, and update them, as the optimization iterations proceed, with additional analysis code runs. This approach has been applied to the design of airfoils by Vanderplaats [72].

Black [4] used a numerical optimization technique combined with a coupled inviscid panel method/boundary layer method for the hydrofoil design. His attention was on the cavitation-free performance, which is unique for hydrofoils. He compared his designs to those of the inverse design method of Eppler and Shen [19, 62] and Shen [61].

Kinnas and Mishima [41] applied a numerical optimization technique to the design of partially cavitating sections. For any cavity length, the lift and drag coefficient, the cavitation number, and the cavity area are expressed in terms of quadratic expansions of the parameters that define the foil geometry, and the operating angle of attack. The coefficients of these functions are obtained, in a least squares sense, from the results of applying a non-linear cavity analysis method to a wide range of values of the involved parameters. The foil geometry and angle of attack are determined from the optimization algorithm by minimizing the drag for the specified requirements and constraints. The method was also applied to the design of supercavitating hydrofoils by Kinnas et al [43] and Mishima and Kinnas [52].

1.2.2 Propeller Blade Design

Propeller design based on experimentally obtained charts are still in common use for typical ship propellers. They are also useful in helping the designer understand the influence of various factors to the propeller performance. Among those charts is the *B-series* of MARIN [71].

Current theoretical design involves two steps.

1. The optimum radial circulation distribution is determined to produce the desired forces.

2. For the radial circulation and a given chordwise load distribution, the actual blade geometry is designed to develop this load distribution.

Betz [3] established the linearized condition for the minimum kinematic energy loss of a propeller in uniform inflow. He analyzed the trailing vortex system far downstream of the propeller and found the *Betz condition*, that the induced inflow on the lifting line must have a radially constant pitch.

Goldstein [24] studied the finite number of trailing vortex sheets and obtained the *Goldstein reduction factor*, which is the ratio of the circumferential mean tangential induced velocity and the local tangential induced velocity at the lifting line. The Goldstein factor is a function of the number of blades, the pitch to diameter ratio of

the helix, and the radius r/R. Computed values for a number of their combinations were published by Tachmindji and Milan [66].

Kramer [44] used the Goldstein factor to compute systematically the thrust coefficient for different number of blades, advance coefficient, and ideal efficiency and made a concise chart, known as the *Kramer diagram.*

Eckhart and Morgan [18] published a design method which utilized the Kramer diagram.

Lerbs [49], from similar considerations to Betz's, derived the *Lerbs criteria* for the optimum propeller in the case of radially varying axisymmetric inflow. In this case, the pitch of the induced inflow on the lifting line is required to be proportional to the square root of the inflow velocity.

Sparenberg [65] and Slijper and Sparenberg [63] determined the optimum circulation on a propeller with a shroud of finite length, as a function of the tip clearance and the hub diameter.

More recently, de Jong developed a circulation optimization/blade design technique for propellers with end plates [13].

Yim [75] included frictional drag and cavity drag in his analysis of optimum radial load distribution. He formulated the Euler differential equation for the variational problem and applied Munk's displacement theorem [33] to it.

Coney [10, 9] developed a vortex lattice lifting line method for the determination of the optimum radial circulation distribution. This method is applicable to multi-component propulsors, such as ducted propellers and a propeller-stator combination.

Kinnas and Coney [38] developed a generalized image model to include the hub and duct effects.

For high aspect ratio propellers, as often seen in aircraft applications, Prandtl's lifting line concept has been a great success. It states that a three dimensional problem may be regarded as, locally at each radius, a two dimensional problem with the inflow altered by the induced velocity.

Van Dyke [70] developed a rigorous lifting line theory based on matched asymptotic expansions.

When the aspect ratio is not high, the variation of the induced velocity over the chord (from the leading edge to the trailing edge) is not negligible and results in a virtual change in camber and angle of attack. This motivated the work for the lifting surface corrections to camber and angle of attack, for example by Morgan et al [53].

Several lifting surface procedures appeared [57, 32] in early 1960's as the computers became commonly available. A very recent review of the mathematical aspects of the propeller design was published by Sparenberg [64]. Almost in parallel to the development of the computer capability both in speed and memory, substantial modifications have been made to the numerical lifting surface methods, including wake alignment [25].

Greeley and Kerwin [25] used the vortex lattice method to solve the lifting surface problem. Continuous singularities on the lifting surface are represented by a set of vortex/source lattices. A part of the geometry is given, that is the radial distribution of chord length, rake, skew, and thickness. From the cavitation consideration, the chord length distribution (blade area) is usually determined empirically, for example by Burrill's diagram [7]. For the same reason, circulation distribution may need to be modified from the optimum distribution. Starting from an initial trial surface, the method adjusts the surface to satisfy the kinematic boundary condition. Thickness effect is included by the linear theory and superimposed on the vortex system. The method assumes that the given inflow is the *effective wake*, which includes the interaction of the generally vortical ship wake in the absence of the propeller and the propeller induced irrotational velocity field.

Huang and Groves [27] developed a method to estimate the axisymmetric effective wake using a simplified Euler equation.

Kerwin et al [31] recently coupled the axisymmetric *RANS* (Reynolds Averaged Navier-Stokes) calculation and the vortex lattice design method. The effective wake necessary for the vortex lattice design method is provided by the *RANS* computation. The propeller force is then transmitted as the body force to the *RANS* domain. Most methods design propellers in uniform inflow or axisymmetric inflow.

Blade skew properly matched to the ship wake is known to improve the unsteady

performance of the propeller. It can decrease the unsteady forces and/or retard the cavitation inception substantially. A common way of including skew is to first use a steady lifting surface method and then analyze the designed propeller using an unsteady lifting surface *analysis* method [35] in a given wake field to find a skew distribution. This skew becomes a new input to the steady lifting surface design method. SKEWOPT by Parsons and Greenblatt [54] is a skew design program which utilizes a numerical optimization technique combined with an unsteady lifting line analysis program.

Kuiper and Jessup [46] developed an unsteady propeller design method, which intended to optimize the cavitation inception speed. They focused on the blade section design based on the method of Eppler and Shen [19, 62] and Shen [61]

Dai et al [12] used an artificial intelligence for the preliminary propeller design. They discussed numerical optimization, knowledge based systems, and genetic algorithms.

1.2.3 Present Design Method

The present design method couples a numerical nonlinear optimization method and a vortex/source lattice cavitating flow analysis method. Typical design methods based on numerical optimization and analysis require the computation of the gradient of the objective function in order to determine the search direction for the next iteration. This is done by differentiating the function either analytically, if possible, or numerically using a finite difference scheme.

For the present application (three-dimensional propeller problem), the evaluation of the gradient of the objective function (e.g. propeller torque) is computationally prohibitively expensive. Therefore, in the present method, the objective function and also the constraint functions are approximated by polynomial expansions. This requires only 1 function evaluation, which corresponds to 1 analysis program run, compared to $1+n$ if the one-sided finite difference scheme were used for the numerical derivatives.

The algorithm is first validated by applying it to some known test functions taken

from literature. It is then applied to the design of two-dimensional cavitating hydrofoil sections and the results are compared with another design. Finally, the method is applied to the design of cavitating propeller blades in non-uniform flow.

Chapter 2

Numerical Optimization Method

The general nonlinear constrained optimization problem is defined as follows.

Problem P :

$$\begin{aligned} \text{minimize} \quad & f(\boldsymbol{x}) \\ \text{subject to} \quad & g_i(\boldsymbol{x}) \leq 0 \quad i = 1, 2, \ldots, m \\ & h_i(\boldsymbol{x}) = 0 \quad i = 1, 2, \ldots, l \end{aligned} \tag{2.1}$$

where $f(\boldsymbol{x})$ is the *objective function* defined on $\mathcal{R}^n$. $\boldsymbol{x}$ is the solution vector of n components. $g_1(\boldsymbol{x}) \leq 0, \ldots, g_m(\boldsymbol{x}) \leq 0$ are *inequality constraints* defined on $\mathcal{R}^n$ and $h_1(\boldsymbol{x}) = 0, \ldots, h_l(\boldsymbol{x}) = 0$ are *equality constraints* also defined on $\mathcal{R}^n$. A vector $\boldsymbol{x} = [x_1, x_2, \ldots, x_n]^T$ satisfying all the constraints is called a *feasible solution* or a *feasible point* to the problem. Thus, the problem is to find a feasible point $\bar{\boldsymbol{x}}$ such that $f(\boldsymbol{x}) \geq f(\bar{\boldsymbol{x}})$ for each feasible point $\boldsymbol{x}$.

2.1 The Method of Multipliers

The method of multipliers is used to solve the constrained minimization problem [2]. For convenience, the inequality constraints are converted into equality constraints by introducing a new variable vector $\boldsymbol{s} = [s_1, \ldots, s_m]^T$.

$$\begin{aligned} & g_i(\boldsymbol{x}) \leq 0 \qquad i = 1, 2, \ldots, m \\ \Longleftrightarrow \quad & g_i(\boldsymbol{x}) + s_i^2 = 0 \quad i = 1, 2, \ldots, m \end{aligned} \tag{2.2}$$

Let us define the *augmented Lagrangian penalty function*

$$\begin{aligned} \mathcal{L}(\boldsymbol{x}, \boldsymbol{s}; \boldsymbol{u}, \boldsymbol{v}, \boldsymbol{c}, \tilde{\boldsymbol{c}}) \equiv f(\boldsymbol{x}) & + \sum_{i=1}^{m} u_i [g_i(\boldsymbol{x}) + s_i^2] + \sum_{i=1}^{l} v_i h_i(\boldsymbol{x}) \\ & + \sum_{i=1}^{m} \frac{1}{2} \tilde{c}_i [g_i(\boldsymbol{x}) + s_i^2]^2 + \sum_{i=1}^{l} \frac{1}{2} c_i h_i^2(\boldsymbol{x}) \\ = f(\boldsymbol{x}) & + \sum_{i=1}^{m} \frac{1}{2} \tilde{c}_i \left[g_i(\boldsymbol{x}) + s_i^2 + \frac{u_i}{\tilde{c}_i} \right]^2 - \sum_{i=1}^{m} \frac{u_i^2}{2\tilde{c}_i} \\ & + \sum_{i=1}^{l} v_i h_i(\boldsymbol{x}) + \sum_{i=1}^{l} \frac{1}{2} c_i h_i^2(\boldsymbol{x}) \end{aligned} \tag{2.3}$$

where $\boldsymbol{u} = [u_1, \ldots, u_m]^T$ and $\boldsymbol{v} = [v_1, \ldots, v_l]^T$ are the Lagrange multiplier vectors corresponding to the equality and inequality constraints, respectively and $\boldsymbol{c} = [c_1, \ldots, c_l]^T$ and $\tilde{\boldsymbol{c}} = [\tilde{c_1}, \ldots, \tilde{c_m}]^T$ are the penalty parameter vectors corresponding to the equality and inequality constraints, respectively.

The constrained minimization problem thus reduces to an unconstrained minimization problem for the function $\mathcal{L}(\boldsymbol{x}, \boldsymbol{s}; \boldsymbol{u}, \boldsymbol{v}, \boldsymbol{c}, \tilde{\boldsymbol{c}})$. This new minimization problem is solved over $[\boldsymbol{x}, \boldsymbol{s}]^T$ with $[\boldsymbol{u}, \boldsymbol{v}, \boldsymbol{c}, \tilde{\boldsymbol{c}}]^T$ fixed, and then $[\boldsymbol{u}, \boldsymbol{v}, \boldsymbol{c}, \tilde{\boldsymbol{c}}]^T$ are updated in an appropriate manner, as will be discussed in the next section.
Let the resulting minimized function be $\theta(\boldsymbol{u}, \boldsymbol{v}, \boldsymbol{c}, \tilde{\boldsymbol{c}})$

$$\theta(\boldsymbol{u}, \boldsymbol{v}, \boldsymbol{c}, \tilde{\boldsymbol{c}}) \equiv \min_{\boldsymbol{x}, \boldsymbol{s}} \mathcal{L}(\boldsymbol{x}, \boldsymbol{s}; \boldsymbol{u}, \boldsymbol{v}, \boldsymbol{c}, \tilde{\boldsymbol{c}}) \tag{2.4}$$

In computing $\theta(\boldsymbol{u}, \boldsymbol{v}, \boldsymbol{c}, \tilde{\boldsymbol{c}})$, the minimization of $\mathcal{L}(\boldsymbol{x}, \boldsymbol{s}; \boldsymbol{u}, \boldsymbol{v}, \boldsymbol{c}, \tilde{\boldsymbol{c}})$ over $[\boldsymbol{x}, \boldsymbol{s}]^T$ can be done first by minimizing $[g_i(\boldsymbol{x}) + s_i^2 + \frac{u_i}{\tilde{c}_i}]^2$ over s_i in terms of $\boldsymbol{x}$ for each $i = 1, 2, \ldots, m$, and then by minimizing the resulting expression over $\boldsymbol{x}$.

The function $[g_i(\boldsymbol{x}) + s_i^2 + \frac{u_i}{\tilde{c}_i}]^2$ takes its minimum value when:

$$\begin{aligned} s_i^2 = & \quad -\left[g_i(\boldsymbol{x}) + \tfrac{u_i}{\tilde{c}_i}\right] \quad \text{if this is non} - \text{negative} \\ s_i^2 = & \quad 0 \qquad\qquad \text{otherwise} \end{aligned} \tag{2.5}$$

Thus,

$$\theta(\boldsymbol{u}, \boldsymbol{v}, \boldsymbol{c}, \tilde{\boldsymbol{c}}) = \min_{\boldsymbol{x}} F(\boldsymbol{x}; \boldsymbol{u}, \boldsymbol{v}, \boldsymbol{c}, \tilde{\boldsymbol{c}}) \tag{2.6}$$

where

$$\begin{aligned} F(\boldsymbol{x}; \boldsymbol{u}, \boldsymbol{v}, \boldsymbol{c}, \tilde{\boldsymbol{c}}) \equiv & \; f(\boldsymbol{x}) + \sum_{i=1}^{m} \frac{1}{2} \tilde{c}_i \max^2 \left\{ g_i(\boldsymbol{x}) + \frac{u_i}{\tilde{c}_i}, 0 \right\} \\ & - \sum_{i=1}^{m} \frac{u_i^2}{2\tilde{c}_i} + \sum_{i=1}^{l} v_i h_i(\boldsymbol{x}) + \sum_{i=1}^{l} \frac{1}{2} c_i h_i^2(\boldsymbol{x}) \end{aligned} \tag{2.7}$$

Note that each constraint has its own penalty parameter c_i or $\tilde{c}_i$ so that constraint violations can be monitored individually.

2.2 Lagrange Multiplier and Penalty Parameter Update Scheme

After the minimization of the function $F(\boldsymbol{x}; \boldsymbol{u}, \boldsymbol{v}, \boldsymbol{c}, \tilde{\boldsymbol{c}})$ over $\boldsymbol{x}$ is done, the Lagrange multiplier vectors $\boldsymbol{u}$ and $\boldsymbol{v}$ and the penalty parameter vectors $\boldsymbol{c}$ and $\tilde{\boldsymbol{c}}$ are updated. When $\boldsymbol{x}_k$ minimizes the augmented Lagrangian penalty function at k-th iteration, the following condition holds:

$$\begin{aligned}\nabla F(\boldsymbol{x}_k;\bar{\boldsymbol{u}},\bar{\boldsymbol{v}},\boldsymbol{c},\tilde{\boldsymbol{c}}) &= \nabla f(\boldsymbol{x}_k)+\sum_{i=1}^{m}\tilde{c}_i\max\left[g_i(\boldsymbol{x})+\frac{\bar{u}_i}{\tilde{c}_i},0\right]\nabla g_i(\boldsymbol{x}_k)\\ &\quad+\sum_{i=1}^{l}\bar{v}_i\nabla h_i(\boldsymbol{x}_k)+\sum_{i=1}^{l}c_i h_i(\boldsymbol{x}_k)\nabla h_i(\boldsymbol{x}_k)\\ &= \nabla f(\boldsymbol{x}_k)+\sum_{i=1}^{m}[\bar{u}_i+\max\{\tilde{c}_i g_i(\boldsymbol{x}),-\bar{u}_i\}]\nabla g_i(\boldsymbol{x}_k)\\ &\quad+\sum_{i=1}^{l}\bar{v}_i\nabla h_i(\boldsymbol{x}_k)+\sum_{i=1}^{l}c_i h_i(\boldsymbol{x}_k)\nabla h_i(\boldsymbol{x}_k)=0 \qquad (2.8)\end{aligned}$$

where $\bar{\boldsymbol{u}}=[\bar{u}_1,\ldots,\bar{u}_m]$, $\bar{\boldsymbol{v}}=[\bar{v}_1,\ldots,\bar{v}_l]^T$, $\tilde{\boldsymbol{c}}=[\tilde{c}_1,\ldots,\tilde{c}_l]^T$, and $\boldsymbol{c}=[c_1,\ldots,c_l]^T$ are the current values of the Lagrange multiplier vectors and the penalty parameter vectors, respectively. On the other hand, for $\boldsymbol{x}_k$, $\bar{\boldsymbol{u}}_{new}$ and $\bar{\boldsymbol{v}}_{new}$ to be an optimum solution to the original problem P, the following necessary conditions must hold [1] [2]:

$$\nabla f(\boldsymbol{x}_k)+\sum_{i=1}^{m}(\bar{u}_{new})_i\nabla g_i(\boldsymbol{x}_k)+\sum_{i=1}^{l}(\bar{v}_{new})_i\nabla h_i(\boldsymbol{x}_k)=0 \qquad (2.9)$$

$$\bar{\boldsymbol{u}}_{new}^T\boldsymbol{g}(\boldsymbol{x}_k)=0 \qquad (2.10)$$

$$\bar{\boldsymbol{u}}_{new}\geq\mathbf{o} \qquad (2.11)$$

Comparing equations (2.8) and (2.9) suggests the following Lagrange multiplier update scheme

$$(\bar{v}_{new})_i=\bar{v}_i+c_i h_i(\boldsymbol{x}_k)\quad i=1,2,\ldots,l \qquad (2.12)$$

and

$$(\bar{u}_{new})_i=\bar{u}_i+\max\{\tilde{c}_i g_i(\boldsymbol{x}_k),-\bar{u}_i\}\quad i=1,2,\ldots,m \qquad (2.13)$$

In order to impose larger penalties to terms whose constraint violations are larger,

[1] These are known as Karush-Kuhn-Tucker (KKT) necessary conditions

the following update formulas for the penalty parameters are used. The first task is to determine the term whose constraint violation is largest by computing

$$\max_i[\max\{g_i(\boldsymbol{x}_k), 0\}, |h_i(\boldsymbol{x}_k)|]$$

Then, for the term corresponding to the largest constraint violation,

$$(c_{new})_i \text{ or } (\tilde{c}_{new})_i = 4c_i \text{ or } 4\tilde{c}_i$$

For other terms,

$$(c_{new})_i \text{ or } (\tilde{c}_{new})_i = 2c_i \text{ or } 2\tilde{c}_i \tag{2.14}$$

2.3 Quasi-Newton Method for the Unconstrained Minimization Problem

As mentioned in the previous section, the minimization of the function $F(\boldsymbol{x}; \boldsymbol{u}, \boldsymbol{v}, \boldsymbol{c}, \tilde{\boldsymbol{c}})$ must be accomplished over $\boldsymbol{x}$. This minimization problem is solved iteratively. We start with an initial solution vector $\boldsymbol{x}_o$, updated at the $(k+1)$-th iteration:

$$\boldsymbol{x}_{k+1} = \boldsymbol{x}_k + \alpha_k \boldsymbol{d}_k \tag{2.15}$$

where $\boldsymbol{d}_k$ is a search direction vector and α_k is a step length.

In the Broyden-Fletcher-Goldfarb-Shanno (BFGS) method [2] , which falls under the general quasi-Newton procedures, $\boldsymbol{d}_k$ is determined in the following way:

$$\begin{aligned} \boldsymbol{d}_k &= -\boldsymbol{D}_k \nabla F(\boldsymbol{x}_k) \\ \boldsymbol{p}_k &= \boldsymbol{x}_{k+1} - \boldsymbol{x}_k \\ \boldsymbol{q}_k &= \nabla F(\boldsymbol{x}_{k+1}) - \nabla F(\boldsymbol{x}_k) \end{aligned}$$

$$
\begin{aligned}
\boldsymbol{D}_{k+1} &= \boldsymbol{D}_k + \frac{\boldsymbol{p}_k \boldsymbol{p}_k^T}{\boldsymbol{p}_k^T \boldsymbol{q}_k} - \frac{\boldsymbol{D}_k \boldsymbol{q}_k \boldsymbol{q}_k^T \boldsymbol{D}_k}{\boldsymbol{q}_k^T \boldsymbol{D}_k \boldsymbol{q}_k} + \tau_k \boldsymbol{v}_k \boldsymbol{v}_k^T \\
\boldsymbol{v}_k &= \boldsymbol{p}_k - \frac{1}{\tau_k} \boldsymbol{D}_k \boldsymbol{q}_k \\
\tau_k &= \frac{\boldsymbol{q}_k^T \boldsymbol{D}_k \boldsymbol{q}_k}{\boldsymbol{p}_k^T \boldsymbol{q}_k}
\end{aligned}
\tag{2.16}
$$

where

$\boldsymbol{D}_o$: arbitrary positive definite matrix (e.g. $\boldsymbol{D}_o \equiv \boldsymbol{I}$)

The step length α_k is determined by using some one-dimensional line search algorithm, as described in Appendix A.

$$
\min_{\alpha_k} F(\boldsymbol{x}_k + \alpha_k \boldsymbol{d}_k), \quad \alpha_k \geq 0 \tag{2.17}
$$

It can be shown that by using the described update scheme, $\boldsymbol{D}_k$ preserves the positive definiteness, thus, $\boldsymbol{d}_k$ is in a direction of descent. $\boldsymbol{D}_k$ is an approximation of the inverse of the Hessian matrix $\boldsymbol{H}^{-1}(\boldsymbol{x}_k)$, where the Hessian matrix is the matrix of second partial derivatives of $F(\boldsymbol{x})$, $H_{ij}(\boldsymbol{x}) = \frac{\partial^2 F(\boldsymbol{x})}{\partial x_i \partial x_j}$. For quadratic functions, $\boldsymbol{D}_k$ becomes the exact Hessian matrix within n steps.

Application of this algorithm requires calculations of ∇f, ∇g, and ∇h. In the event ∇f, ∇g, and ∇h are given in terms of known functions, then ∇f, ∇g, and ∇h may be determined analytically. However, if ∇f, ∇g, and ∇h are not explicitly known in terms of the variables, one approach is to approximate them in terms of polynomial expansions.

2.4 Scaling and Stopping Criterion

From the numerical point of view, it is important for all terms of the objective function to be of the same order of magnitude. Otherwise, a small error relative to other terms could be missed. Therefore, all the constraint functions are normalized with respect to their typical values.

An equally important issue is the stopping criterion of the iterative algorithm. Let ε be a prescribed tolerance. The stopping criterion in the iterative process to

minimize $F(\boldsymbol{x})$ via the quasi-Newton method, is provided by Dennis and Schnabel [14]:

$$\begin{aligned} |\boldsymbol{x}_{k+1} - \boldsymbol{x}_k| &\leq \varepsilon \\ \text{and} & \\ |\nabla F(\boldsymbol{x}_k)| &\leq \varepsilon \end{aligned} \tag{2.18}$$

The stopping criterion in the iteration for the penalty parameters is defined as:

$$\sum_{i=1}^{m} |\max\{g_i(\boldsymbol{x}), 0\}| + \sum_{i=1}^{l} |h_i(\boldsymbol{x})| \leq \varepsilon \tag{2.19}$$

This simply means that all the imposed constraints are satisfied within a tolerance.

2.5 Validation

The numerical optimization algorithm described in the previous sections has been implemented to a computer program. The program is tested for several known functions taken from Hock and Schittkowski [26] and Shittkowski [60].

2.5.1 Unconstrained Optimization Problem

Unconstrained minimization problems are tested first. The number of iterations required for the converged solutions is summarized in Table 2.1. Convergence history of the test problem No. 2-3 is shown in Figure 2-1.

Problem number	Number of variables,n	Number of iterations
2-1	2	20
2-2	2	20
2-3	6	35
2-4	10	201

Table 2.1: Performance of the optimization program for unconstrained optimization test problems

Test Problem No. 2-1	
Objective function	$f(\boldsymbol{x}) = 4(x_1 - 5)^2 + (x_2 - 6)^2$ $\boldsymbol{x} = (x_1, x_2)^T$
Equality constraints	none
Inequality constraints	none
Starting point	$\boldsymbol{x}_o = (8, 9)^T$ $f(\boldsymbol{x}_o) = 45$
Solution from [60]	$\bar{\boldsymbol{x}} = (5, 6)^T$ $f(\bar{\boldsymbol{x}}) = 0$
Present method	$\bar{\boldsymbol{x}} = (5.000, 6.000)^T$ $f(\bar{\boldsymbol{x}}) = 0.000$

Test Problem No. 2-2	
Objective function	$u_1^2 + u_2^2 + u_3^2$ $u_i = c_i - x_1(1 - x_2^i)$ $c_1 = 1.5, c_2 = 2.25, c_3 = 2.625$ $\boldsymbol{x} = (x_1, x_2)^T$
Equality constraints	none
Inequality constraints	none
Starting point	$\boldsymbol{x}_o = (2, 0.2)^T$ $f(\boldsymbol{x}_o) = 0.5298$
Solution from [60]	$\bar{\boldsymbol{x}} = (3, 0.5)^T$ $f(\bar{\boldsymbol{x}}) = 0$
Present method	$\bar{\boldsymbol{x}} = (3.000, 0.5000)^T$ $f(\bar{\boldsymbol{x}}) = 0.000$

Test Problem No. 2-3	
Objective function	$f(\boldsymbol{x}) = 10 \sum_{i=1}^{6} (16 - i)(x_i - 1)^2$ $\boldsymbol{x} = (x_1, x_2, x_3, x_4, x_5, x_6)^T$
Equality constraints	none
Inequality constraints	none
Starting point	$\boldsymbol{x}_o = (0, 0, 0, 0, 0, 0)^T$ $f(\boldsymbol{x}_o) = 750$
Solution from [60]	$\bar{\boldsymbol{x}} = (1, 1, 1, 1, 1, 1)^T$ $f(\bar{\boldsymbol{x}}) = 0$
Present method	$\bar{\boldsymbol{x}} = (1.000, 1.000, 1.000, 1.000, 1.000, 1.000)^T$ $f(\bar{\boldsymbol{x}}) = 0.000$

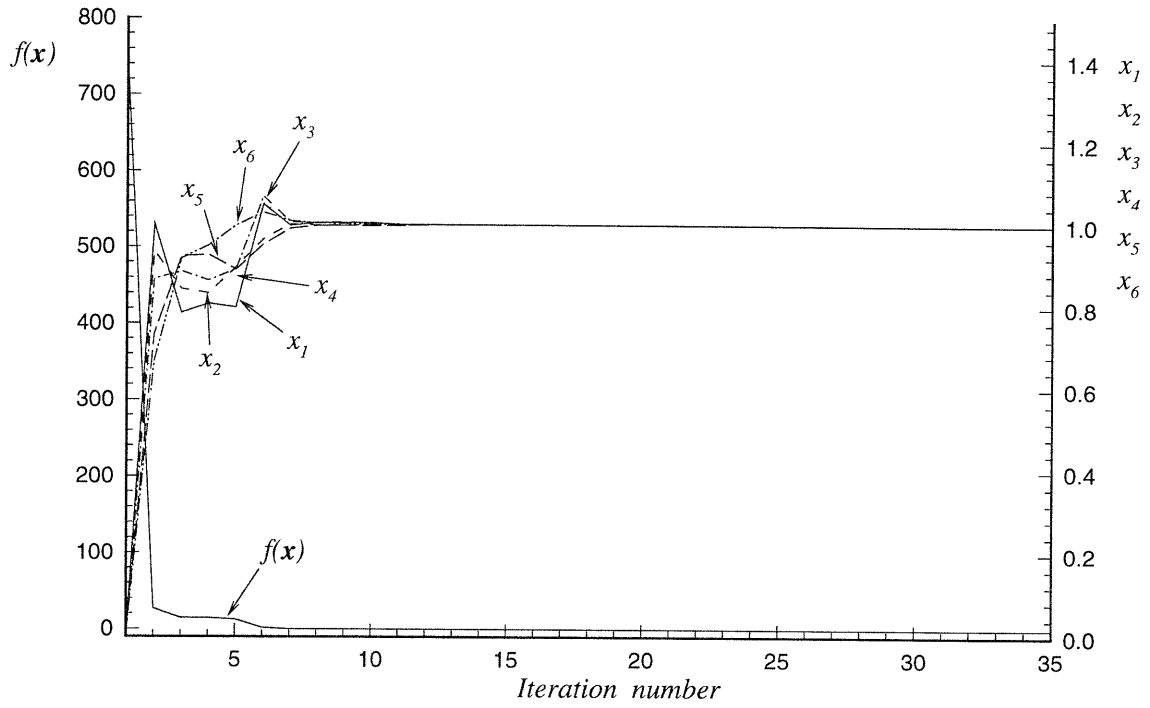

Figure 2-1: Convergence history of the present method for test problem No. 2-3

Test Problem No. 2-4	
Objective function	$f(\boldsymbol{x}) = \left[\sum_{i=1}^{10} i^3 (x_i - 1)^2\right]^{1/3}$ $\boldsymbol{x} = (x_1, x_2, x_3, x_4, x_5, x_6, x_7, x_8, x_9, x_{10})^T$
Equality constraints	none
Inequality constraints	none
Starting point	$\boldsymbol{x}_o = (0, 0, 0, 0, 0, 0, 0, 0, 0, 0)^T$ $f(\boldsymbol{x}_o) = 14.4624$
Solution from [60]	$\bar{\boldsymbol{x}} = (1, 1, 1, 1, 1, 1, 1, 1, 1, 1)^T$ $f(\bar{\boldsymbol{x}}) = 0$
Present method	$\bar{\boldsymbol{x}} = (1.000, 1.000, 1.000, 1.000, 1.000,$ $1.000, 1.000, 1.000, 1.000, 1.000)^T$ $f(\bar{\boldsymbol{x}}) = 0.000$

2.5.2 Constrained Optimization Problem

Several constrained optimization test problems are used to test the performance of the program in this section. Table 2.2 summarizes the test problems used.

Test Problem No. 2-5	
Objective function	$f(\boldsymbol{x}) = 9 - 8x_1 - 6x_2 - 4x_3 + 2x_1^2 + 2x_2^2 + x_3^2$ $+2x_1x_2 + 2x_1x_3$ $\boldsymbol{x} = (x_1, x_2, x_3)^T$
Equality constraints	none
Inequality constraints	$g_1(\boldsymbol{x}) = x_1 + x_2 + 2x_3 - 3 \leq 0$ $g_2(\boldsymbol{x}) = -x_1 \leq 0$ $g_3(\boldsymbol{x}) = -x_2 \leq 0$ $g_4(\boldsymbol{x}) = -x_3 \leq 0$
Starting point	$\boldsymbol{x}_o = (0.5, 0.5, 0.5)^T$ $f(\boldsymbol{x}_o) = 2.25$
Solution from [26]	$\bar{\boldsymbol{x}} = (1.3333, 0.7778, 0.4444)^T$ $f(\bar{\boldsymbol{x}}) = 0.1111$
Present method	$\bar{\boldsymbol{x}} = (1.3333, 0.7778, 0.4444)^T$ $f(\bar{\boldsymbol{x}}) = 0.1111$

Test Problem No. 2-6	
Objective function	$f(\boldsymbol{x}) = (x_1 - 1)^2 + (x_2 - 2)^2 + (x_3 - 3)^2 + (x_4 - 4)^2$ $\boldsymbol{x} = (x_1, x_2, x_3, x_4)^T$
Equality constraints	$h_1(\boldsymbol{x}) = x_1 - 2 = 0$ $h_2 = x_3^2 + x_4^2 - 2 = 0$
Inequality constraints	none
Starting point	$\boldsymbol{x}_o = (1, 1, 1, 1)^T$ $f(\boldsymbol{x}_o) = 14$
Solution from [26]	$\bar{\boldsymbol{x}} = (2, 2, 0.8485, 1.1314)^T$ $f(\bar{\boldsymbol{x}}) = 13.8579$
Present method	$\bar{\boldsymbol{x}} = (2.0000, 2.0000, 0.8485, 1.1314)^T$ $f(\bar{\boldsymbol{x}}) = 13.8579$

Test Problem No. 2-7	
Objective function	$f(\boldsymbol{x}) = \sum_{i=1}^{16} \sum_{j=1}^{16} a_{ij}(x_i^2 + x_i + 1)(x_j^2 + x_j + 1)$ $\boldsymbol{x} = (x_1, x_2, \ldots, x_{16})^T$
Equality constraints	$h_i(\boldsymbol{x}) = \sum_{j=1}^{16} b_{ij} x_j - c_i = 0$ $i = 1, \ldots, 8$ a_{ij}, b_{ij}, and c_i are given in Appendix B
Inequality constraints	$g_i(\boldsymbol{x}) = -x_i \leq 0$ $g_{i+16}(\boldsymbol{x}) = x_i - 5 \leq 0$ $i = 1, \ldots, 16$
Starting point	$\boldsymbol{x}_o = (10, 10, 10, 10, 10, 10, 10, 10, 10, 10, 10, 10, 10, 10, 10, 10)^T$ $f(\boldsymbol{x}_o) = 566766$
Solution from [26]	$\bar{\boldsymbol{x}} = (0.03985, 0.7920, 0.2029, 0.8444, 1.1270, 0.9347, 1.6820,$ $0.1553, 1.5679, 0, 0, 0, 0.6602, 0, 0.6743, 0)^T$ $f(\bar{\boldsymbol{x}}) = 244.8997$
Present method	$\bar{\boldsymbol{x}} = (0.03985, 0.7920, 0.2029, 0.8444, 1.2699, 0.9347, 1.6820,$ $0.1553, 1.5679, 0, 0, 0, 0.6602, 0, 0.6742, 0)^T$ $f(\bar{\boldsymbol{x}}) = 244.8997$

Problem no.	No. of variables n	No. of equality constraints l	No. of inequality constraints m
2-5	3	0	4
2-6	4	2	0
2-7	16	8	32

Table 2.2: Constrained optimization test problems

Chapter 3

Analysis of Cavitating Propellers by Vortex Lattice Method

The analysis of the flow around a cavitating propeller subject to non-uniform inflow is required at each design optimization iteration. Since this analysis is made a number of times in the course of optimization, it *MUST* be computationally efficient. For this reason, a vortex lattice method was chosen. A vortex lattice analysis method for cavitating propellers in nonuniform flow developed at MIT is *HPUF-3A*. A brief description of *HPUF-3A* is given in this chapter.

3.1 Vortex Lattice Method

The presence of a propeller is represented by the distribution of singularities (vortices and sources) on the blade mean camber surface and its assumed wake surface. The unknown strength of the singularities is determined by applying the kinematic and dynamic boundary conditions at some appropriate control points.
The basic assumptions are :

- Linearized boundary conditions are satisfied on the blade mean camber surface

- The wake consists of the *transition* wake, where the roll up and and contraction occur, and the *ultimate* wake, where the trailing vortices become a concentrated tip vortex. This is illustrated in Figure 3-1.
- There is no roll up in the transition wake.
- Given inflow is an effective wake, which is the difference between the total velocity in the presence of the propeller and the propeller induced velocity.
- Sources representing the blade thickness are independent of time and determined by a spanwise application of thin wing theory.
- The formation and decay of the cavity occurs instantaneously depending only on whether the pressure exceeds the vapor pressure.
- Cavity starts at the leading edge of the blade and vanishes at the cavity trailing edge.
- Cavity thickness is constant across each strip in the spanwise direction and varies linearly along each cavity panel in the chordwise direction.
- There are no spanwise effects in the cavity closure condition.
- Viscous force is computed based on the frictional drag coefficient, C_f, which is applied uniformly on the wetted surface of the blade.

HPUF-3A has been continuously modified since its first version by Lee [47] in 1979. The major modifications include:

1. Nonlinear leading edge correction to the cavity solution [37].
2. Inclusion of the hub effect via images [38].
3. Supercavitating sections, which have finite trailing edge thickness [45].
4. Blade geometry representation by B-splines [51].
5. Wake alignment [58]. This is the version that has been used in the present optimization program.

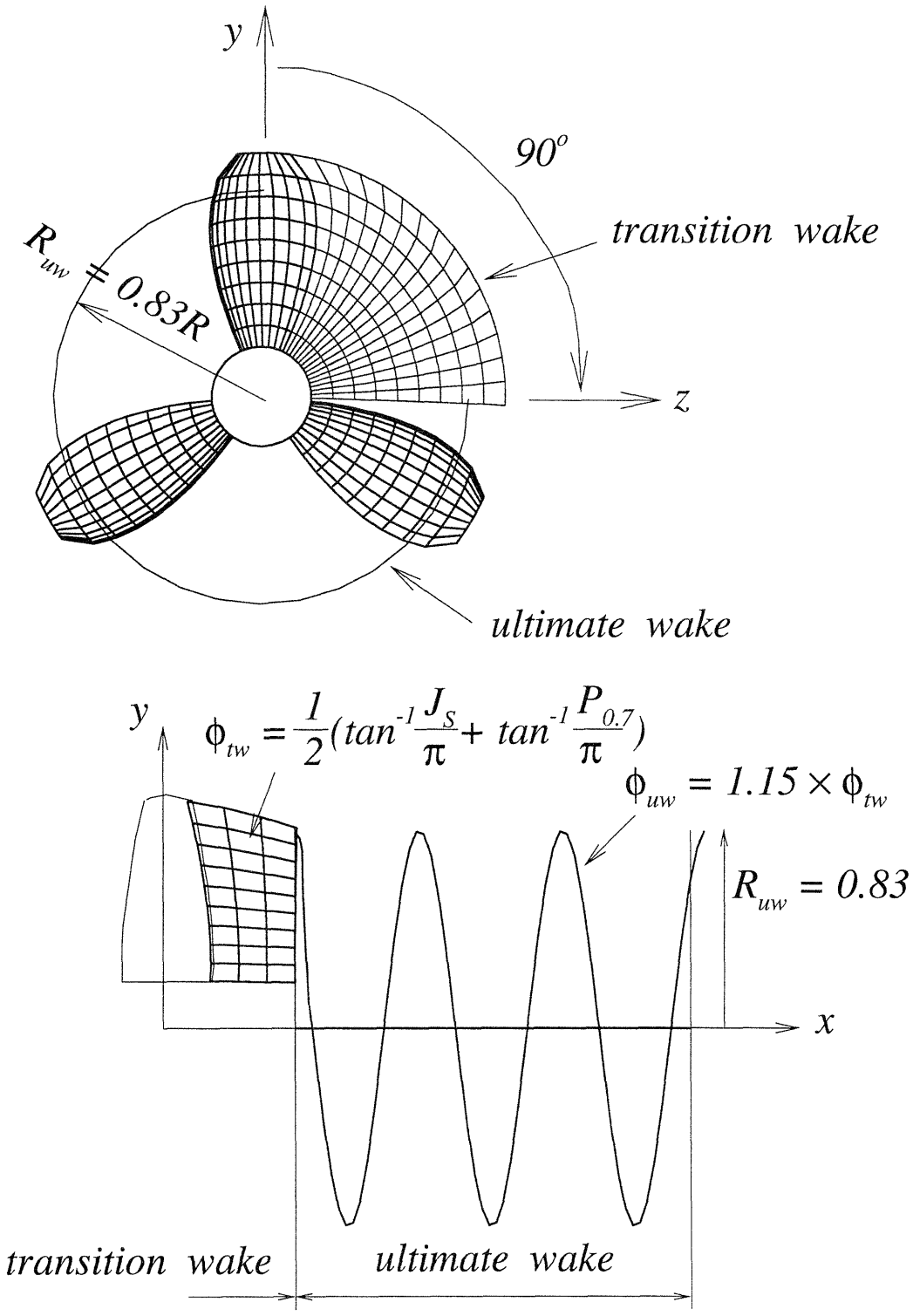

Figure 3-1: Wake model used in *HPUF-3A*

3.2 Blade Geometry

The coordinate systems and the propeller geometrical notation are shown in Figure 3-2. A propeller-fixed cartesian coordinate system is first defined with the x axis positive downstream. The y axis is normal to x axis at any angular orientation relative to the *key blade*. The z axis completes the right hand system. A cylindrical coordinate system is defined in the usual way.

$$\begin{aligned} x &= x \\ r &= \sqrt{y^2 + z^2} \\ \theta &= \tan^{-1}\frac{z}{y} \end{aligned} \tag{3.1}$$

The radial distributions of skew, $\theta_m(r)$, and rake, $x_m(r)$, define the mid-chord line of the blade as illustrated in Figure 3-3. The leading and trailing edges of the blade are constructed by passing a helix of pitch angle $\phi(r)$ through the mid-chord line.

$$\begin{aligned} x_{l,t}(r) &= x_m(r) \mp \frac{c(r)}{2}\sin\phi(r) \\ \theta_{l,t}(r) &= \theta_m(r) \mp \frac{c(r)}{2}\cos\phi(r) \\ y_{l,t}(r) &= r\cos\theta_{l,t}(r) \\ z_{l,t}(r) &= r\sin\theta_{l,t}(r) \end{aligned} \tag{3.2}$$

where $c(r)$ is the chord length at the radius r , and the subscripts l and t denote the leading and trailing edges, respectively.

The camber $f(r,s)$ is measured on the cylindrical surface of radius r normal to the nose-tail helix, where s is a non-dimensional chordwise coordinate, which is 0 at the leading edge and 1 at the trailing edge.

Finally, the thickness $t(r,s)$ is added symmetrically to the camber line on the cylinder in the normal direction to the mean camber surface. This is shown in Figure

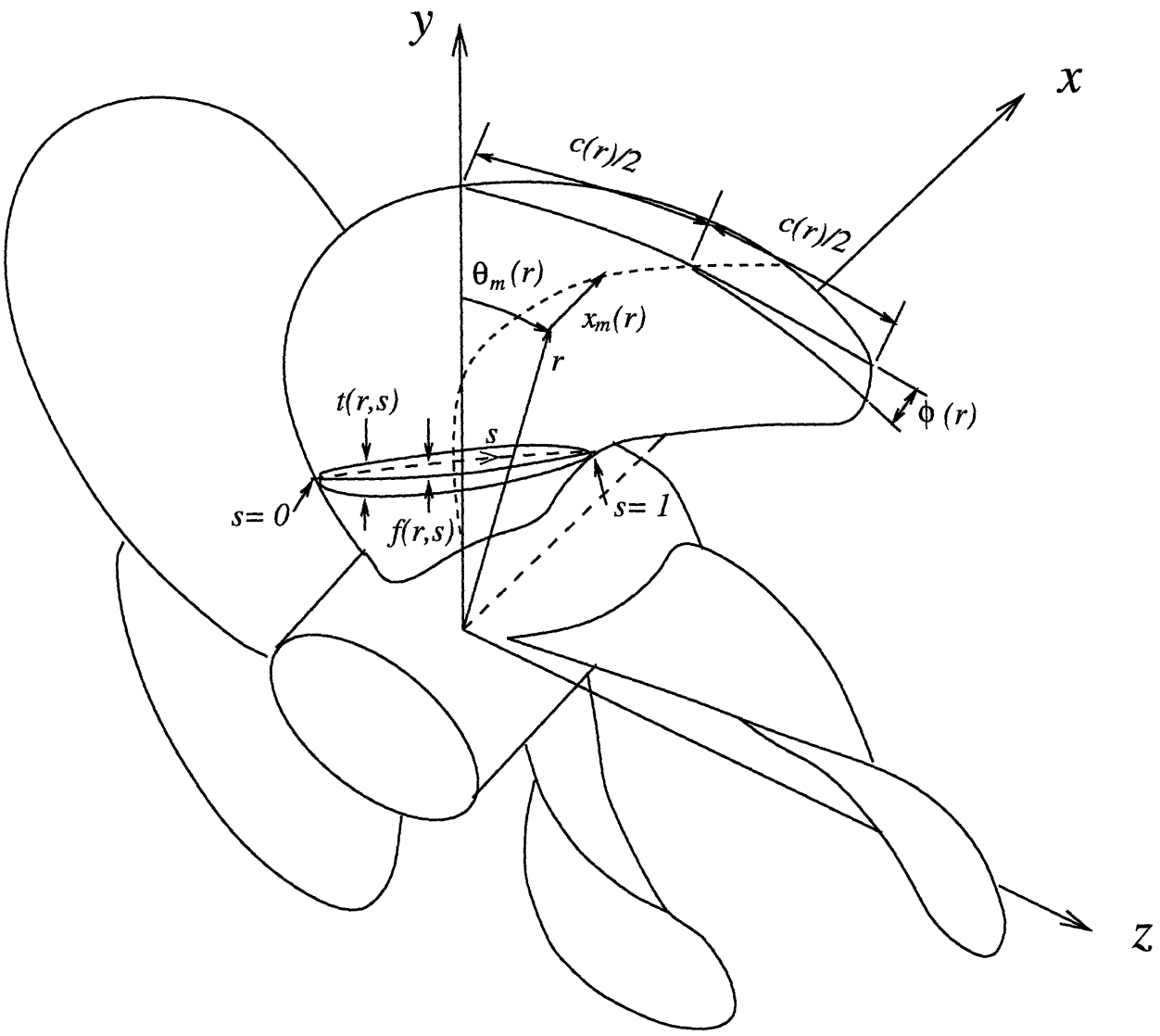

Figure 3-2: Coordinate systems and geometrical notations in *HPUF-3A*, adapted from [25]

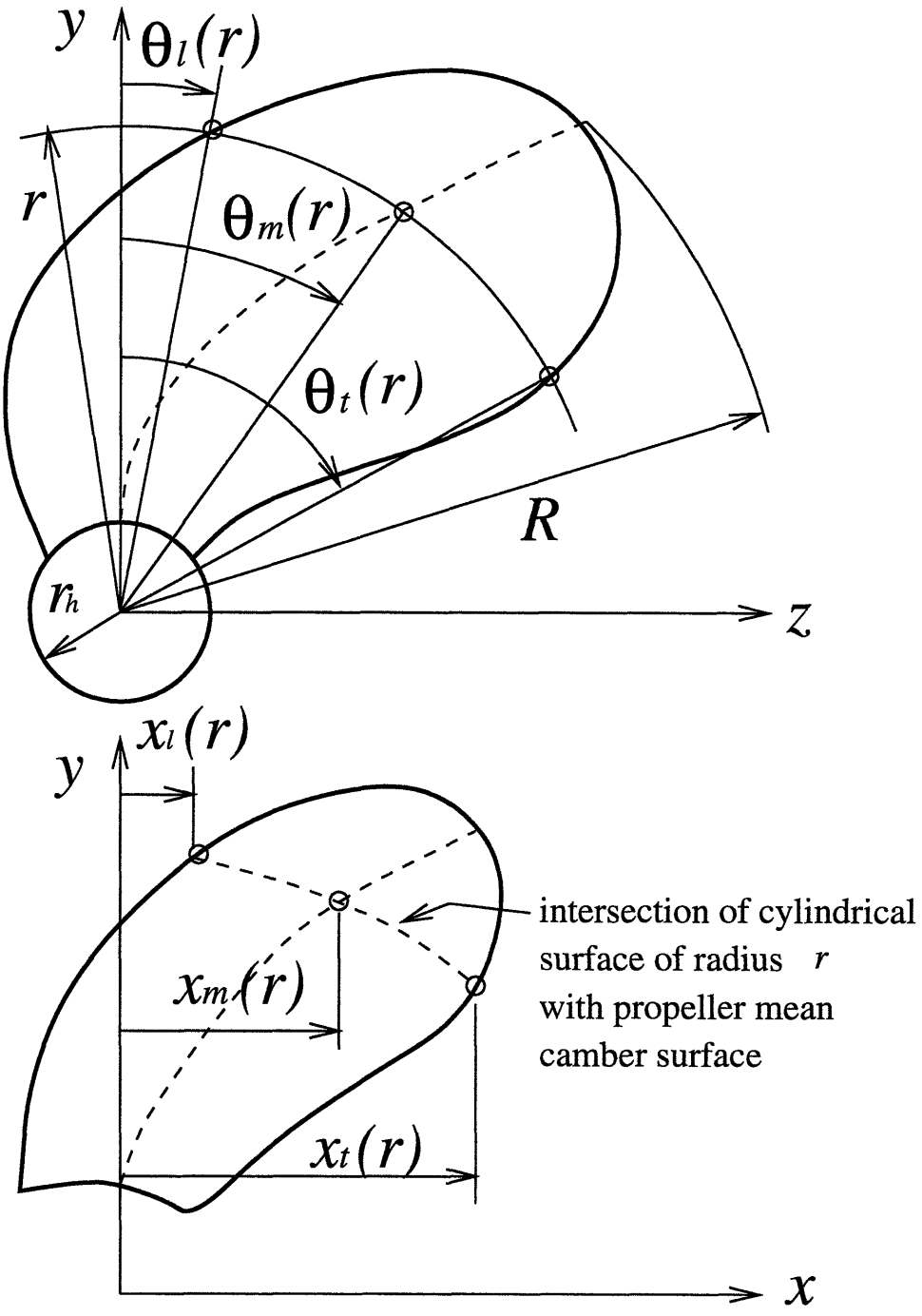

Figure 3-3: Radial distribution of skew and rake, adapted from [35]

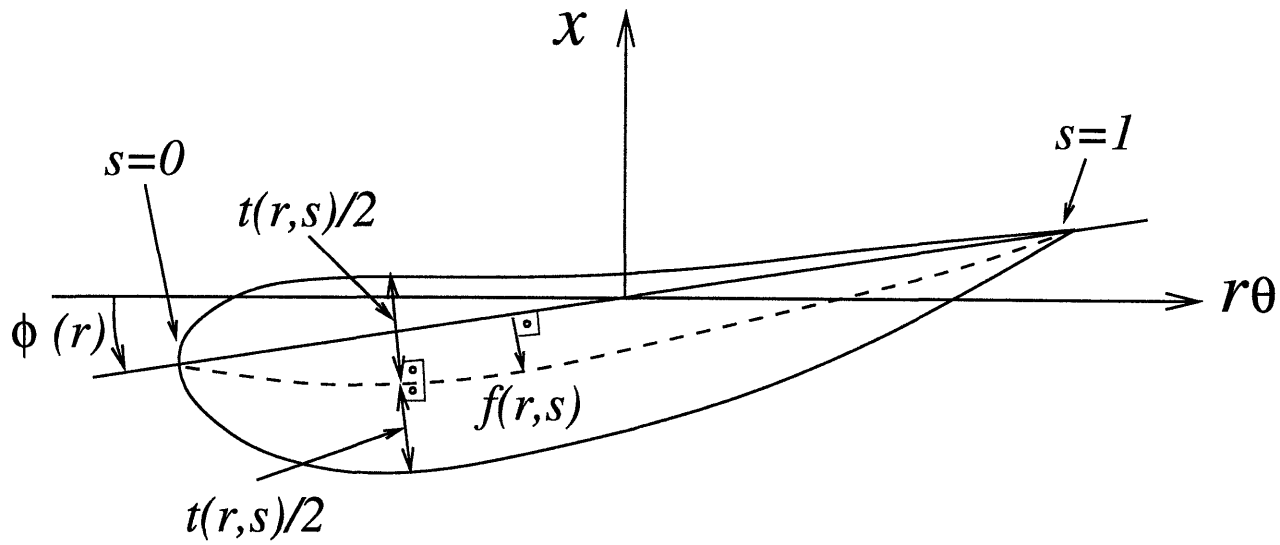

Figure 3-4: Construction of blade section from mean camber line and thickness form 3-4.

$$
\begin{aligned}
x_c(r,s) &= x_m(r) + c(r)\left(s - \frac{1}{2}\right)\sin\phi(r) - f(r,s)\cos\phi(r) \\
\theta_c(r,s) &= \theta_m(r) + c(r)\left(s - \frac{1}{2}\right)\frac{\cos\phi(r)}{r} + f(r,s)\frac{\sin\phi(r)}{r} \\
y_c(r,s) &= r\cos\theta_c(r,s) \\
z_c(r,s) &= r\sin\theta_c(r,s)
\end{aligned}
\tag{3.3}
$$

The maximum values of $f(r,s)$ and $t(r,s)$ at radius r are denoted as the maximum camber, $f_o(r)$, and the maximum thickness, $t_o(r)$, respectively.

3.3 B-spline Representation of the Blade

The B-spline representation of the blade is attractive in several ways and has been included in *HPUF-3A*.

In the traditional geometry definition described in section 3.2, tabular data for

radial distributions of pitch, rake, and skew, and chordwise distributions of camber and thickness are usually given. Inaccuracy arises due to the interpolation process necessary to determine the actual blade surface. By using B-splines, all points on the surface are defined uniquely. Another advantage of B-splines is that the blade may be defined with a relatively few number of parameters. This is particularly convenient for designing blades by numerical optimization. The number of parameters, also of the design variables, reflects the computational effort of the optimization method.

3.3.1 Cubic B-spline Curves and Surfaces

In *HPUF-3A*, cubic B-splines, which is a subset of *Non-Uniform Rational B-Splines (NURBS)*, are used. To see some properties of B-splines, B-spline curves are reviewed first following Patrikalakis [55].

Non-uniform B-spline curves are defined as :

$$\begin{aligned} \boldsymbol{P}(u) &= [x(u), y(u), z(u)] = \sum_{i=0}^{N_u-1} \boldsymbol{d}_i N_{i,k}(u) \\ N_u &\geq k \end{aligned} \tag{3.4}$$

where,

$\boldsymbol{d}_i$: B-spline control points

$N_{i,k}(u)$: B-spline basis of order k (piecewise polynomial of degree $k-1$)

u : parameter in the interval $t_o \leq u \leq t_{N_u+k-1}$

$$T = \{\underbrace{t_o = t_1 = \cdots = t_{k-1}}_{k \text{ equal values}} < \underbrace{t_k \leq t_{k+1} \leq \cdots \leq t_{N_u-1}}_{N_u-k \text{ internal knots}} < \underbrace{t_{N_u} = \cdots = t_{N_u+k-1}}_{k \text{ equal values}}\}$$

: knot vector, which has total $N_u + k$ knots

B-spline basis $N_{i,k}(u)$ is determined from the following required properties.

1. Partition of unity

$$\sum_{i=0}^{N_u-1} N_{i,k}(u) = 1 \tag{3.5}$$

2. Positivity

$$N_{i,k}(u) \geq 0 \tag{3.6}$$

3. Local support (change of one vertex, $\boldsymbol{d}_i$ affects curve locally)

$$N_{i,k}(u) = 0 \qquad \text{if } u \notin [t_i, t_{i+k}] \tag{3.7}$$

4. C^{k-2} continuity

   $N_{i,k}(u)$ is $(k-2)$ times continuously differentiable at simple knots. If a knot has a multiplicity equal to p $(\leq k)$,

   $t_j = t_{j+1} = \cdots = t_{j+p-1}$

   and $N_{i,k}(u)$ is $(k-p-1)$ times continuously differentiable.

$N_{i,k}(u)$ may be obtained recursively as, for example, in Yamaguchi [74].

$$N_{i,1}(u) = \begin{cases} 1 & u \in [t_i, t_{i+1}) \\ 0 & u \notin [t_i, t_{i+1}) \end{cases} \tag{3.8}$$

$$N_{i,k}(u) = \frac{u - t_i}{t_{i+k-1} - t_i} N_{i,k-1}(u) + \frac{t_{i+k} - u}{t_{i+k} - t_{i+1}} N_{i+1,k-1}(u) \tag{3.9}$$

If a "0/0" situation occurs, that term is set equal to 0 in equation (3.9).
Since in most propeller applications, continuity in curvature but not in higher order derivatives is desirable, $k = 4$ (cubic B-splines) is chosen. Figure 3-5 shows the cubic B-spline basis $(k = 4)$ for $N_u = 7$.

Figure 3-6 illustrates control points and the corresponding cubic B-spline curve.

Cubic B-spline surfaces are defined similarly as follows.

$$\boldsymbol{P}(u, w) = [x(u, w), y(u, w), z(u, w)] = \sum_{i=0}^{N_u - 1} \sum_{j=0}^{N_w - 1} \boldsymbol{d}_{ij} N_{i,4}(u) N_{j,4}(w) \tag{3.10}$$

where

$\boldsymbol{d}_{ij}$: B-spline control points

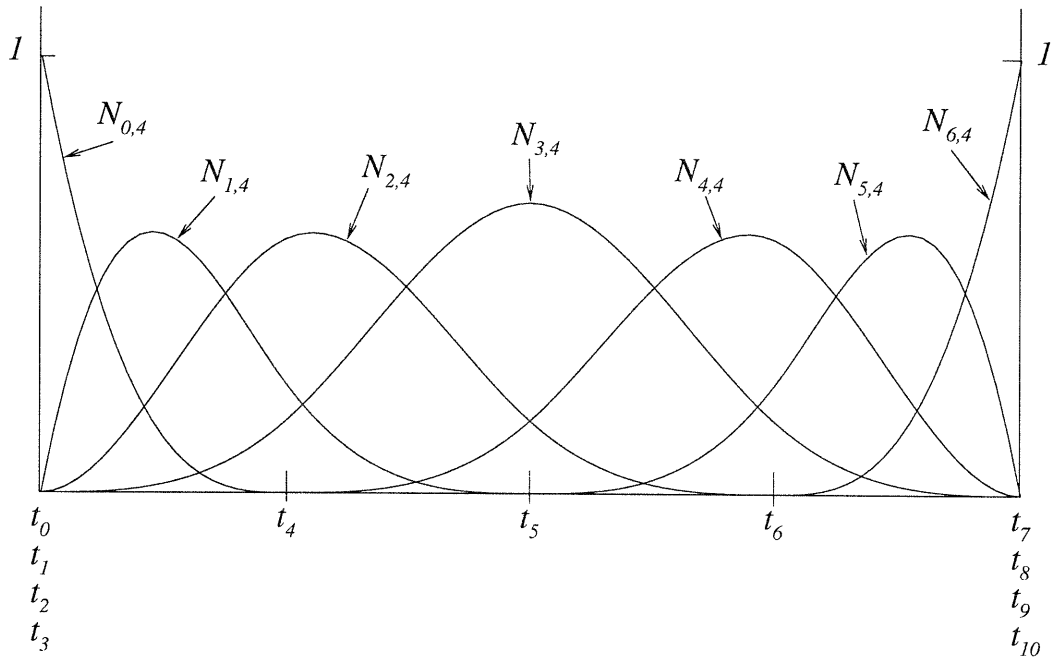

Figure 3-5: Cubic B-spline basis ($k = 4$) : $N_u = 7$

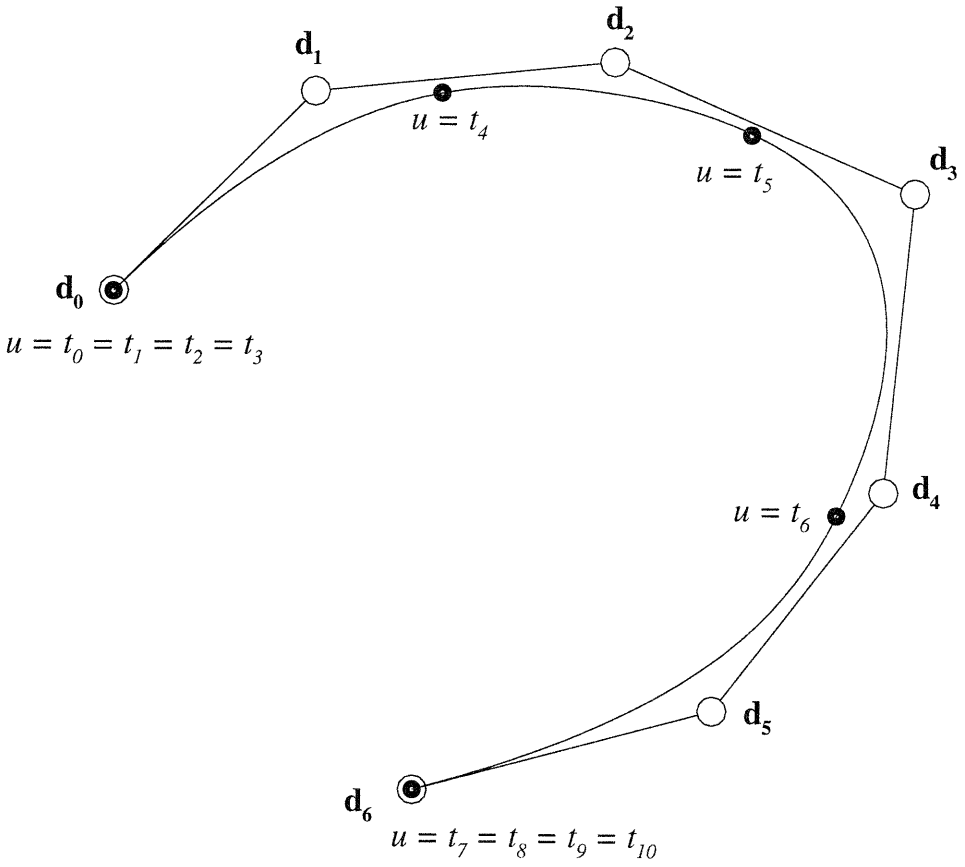

Figure 3-6: Cubic B-spline curve : $N_u = 7$

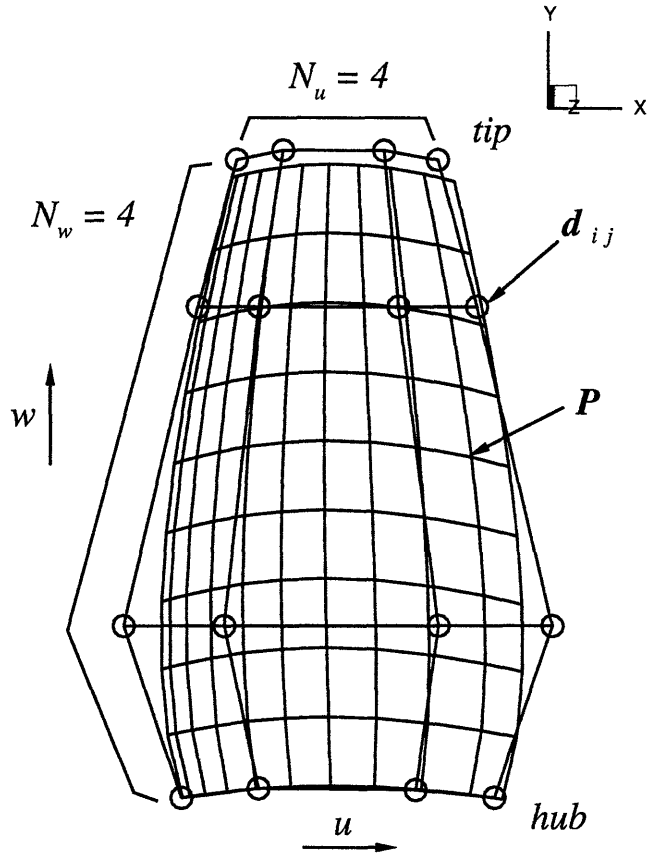

Figure 3-7: Cubic B-spline surface. 4 × 4 vertex polygon net is shown together with the 10 × 9 grid utilized in *HPUF-3A*

$N_{i,4}(u)$: B-spline basis of order 4

$N_{j,4}(w)$: B-spline basis of order 4

The basis $N_{i,4}(u)$ and $N_{j,4}(w)$ take the same form as before. A cubic B-spline surface from a 4 × 4 vertex polygon net is shown in Figure 3-7.

3.3.2 Physical and Parametric Spacings

In *HPUF-3A*, the singularities (discrete vortices and sources) are placed on the blade mean camber surface with uniform spacing in the radial direction and half-cosine spacing in the chordwise direction. When the blade geometry is defined by B-splines, if the parameters u and v are cosine spaced and uniformly spaced, the resulting singularities are not in general correctly located in the physical space as shown in

Figure 3-8. It is essential to have the correct spacing in a numerical lifting surface theory for a required accuracy [47]. In *HPUF-3A*, parameters u and v are iteratively determined to give the desired spacing in the physical space, as described in Appendix C. Figure 3-9 shows the correct spacing achieved in the physical space after the iterations.

3.3.3 Effect of the Number of B-spline Vertices on the Blade Geometry Representation and the Solution

If one desired to represent a certain given propeller blade geometry exactly, an infinite number of B-spline vertices would be necessary. However, in general, a fewer number of vertices is sufficient to represent typical propeller blades. Figure 3-10 shows the blade geometries defined by B-splines with 4×4 and 7×7 vertices. Given a target propeller blade, DTMB $N4381$, and the number of B-spline vertices, a least squares problem for minimizing the error between the target geometry and the resulting geometry defined by the vertices was solved [31]. Contour plots of the error distribution over the entire blade are shown in Figure 3-11. The error is the distance in three-dimensional space between the input point and the B-spline defined point, non-dimensionalized by the propeller radius, R. Figure 3-12 shows that the predicted forces and the cavity volumes for this propeller with 4×4 and 7×7 vertices agree well with the values for the original blade. This particularly justifies the use of very few number of vertices for the blade design, since there is no target blade geometry and the only concerns are the forces and the cavity characteristics. The forces are less sensitive than the cavity volume to the number of B-spline polygon vertices. The cavity volume appears to be converging to that corresponding to $N4381$ more slowly than K_T and K_Q.

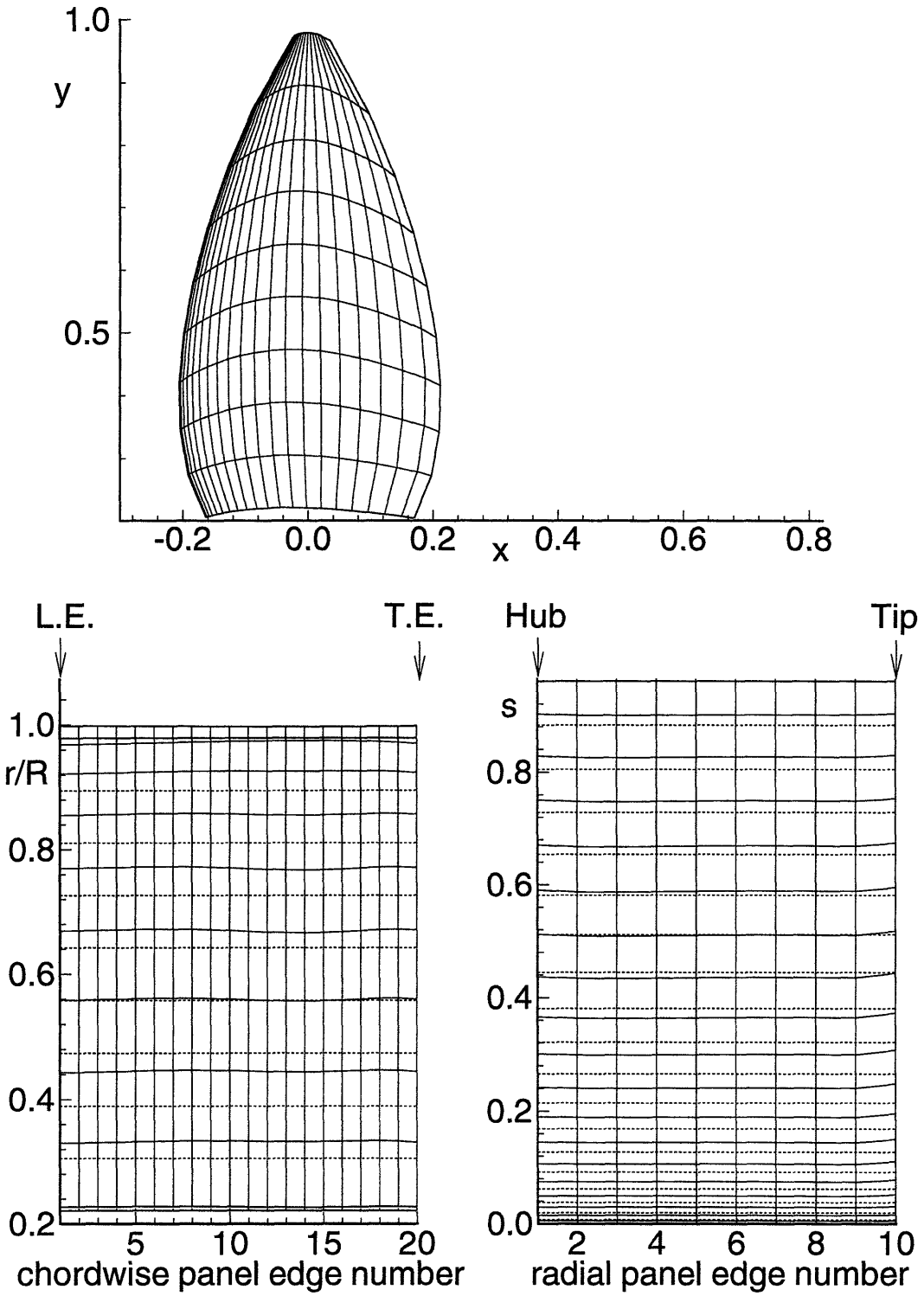

Figure 3-8: Chordwise and radial vortex lattice spacing from half-cosine and uniform spacing in u and w. The spacing required by *HPUF-3A* with 20 $\times$ 9 panels is also shown with dashed lines.

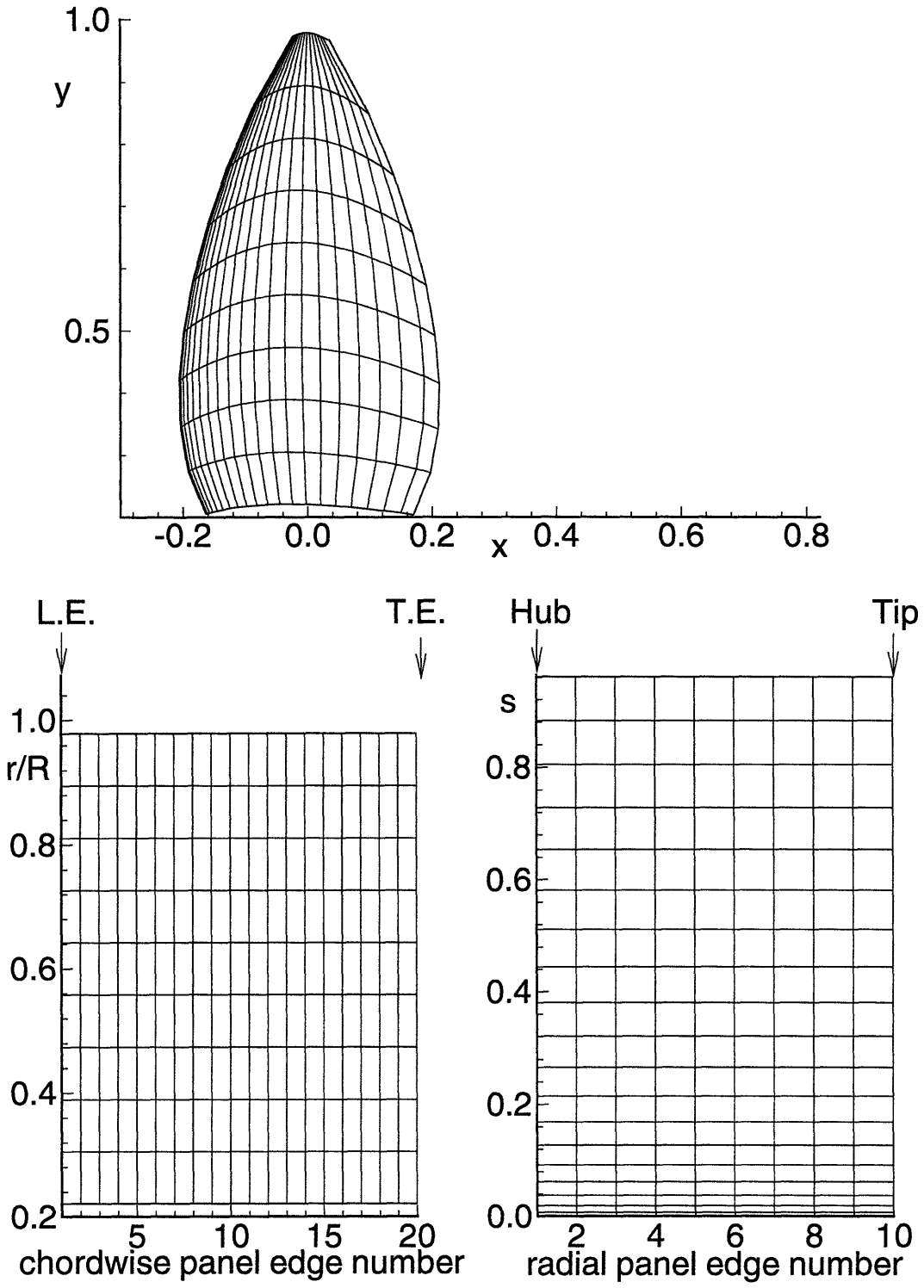

Figure 3-9: Chordwise and radial vortex lattice spacing from iteratively determined u and w. Notice that the vortex lattice is placed according to *HPUF-3A*'s scheme.

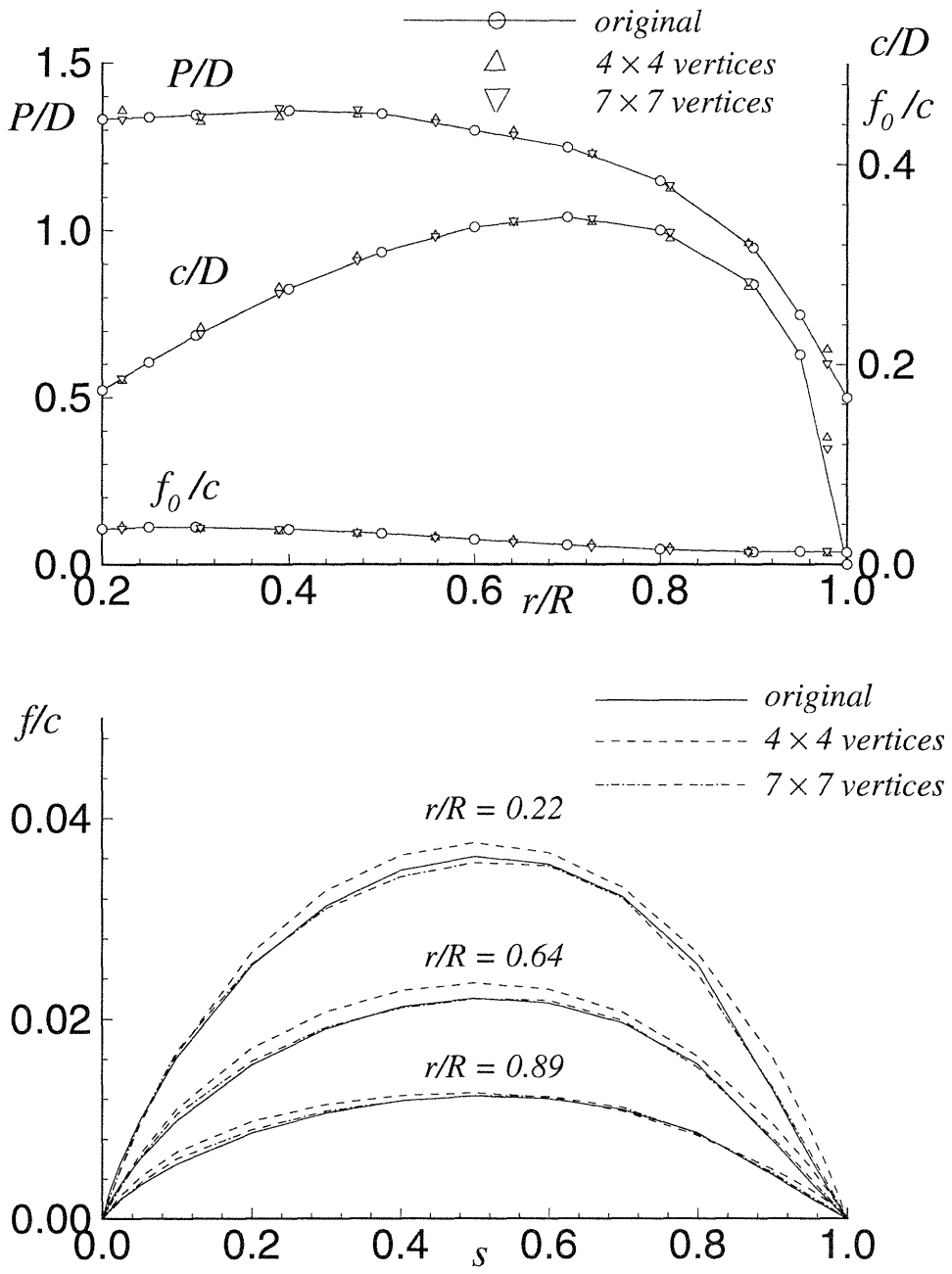

Figure 3-10: Original $N4381$ blade geometry and the geometries defined by 4×4 and 7×7 B-spline vertices.

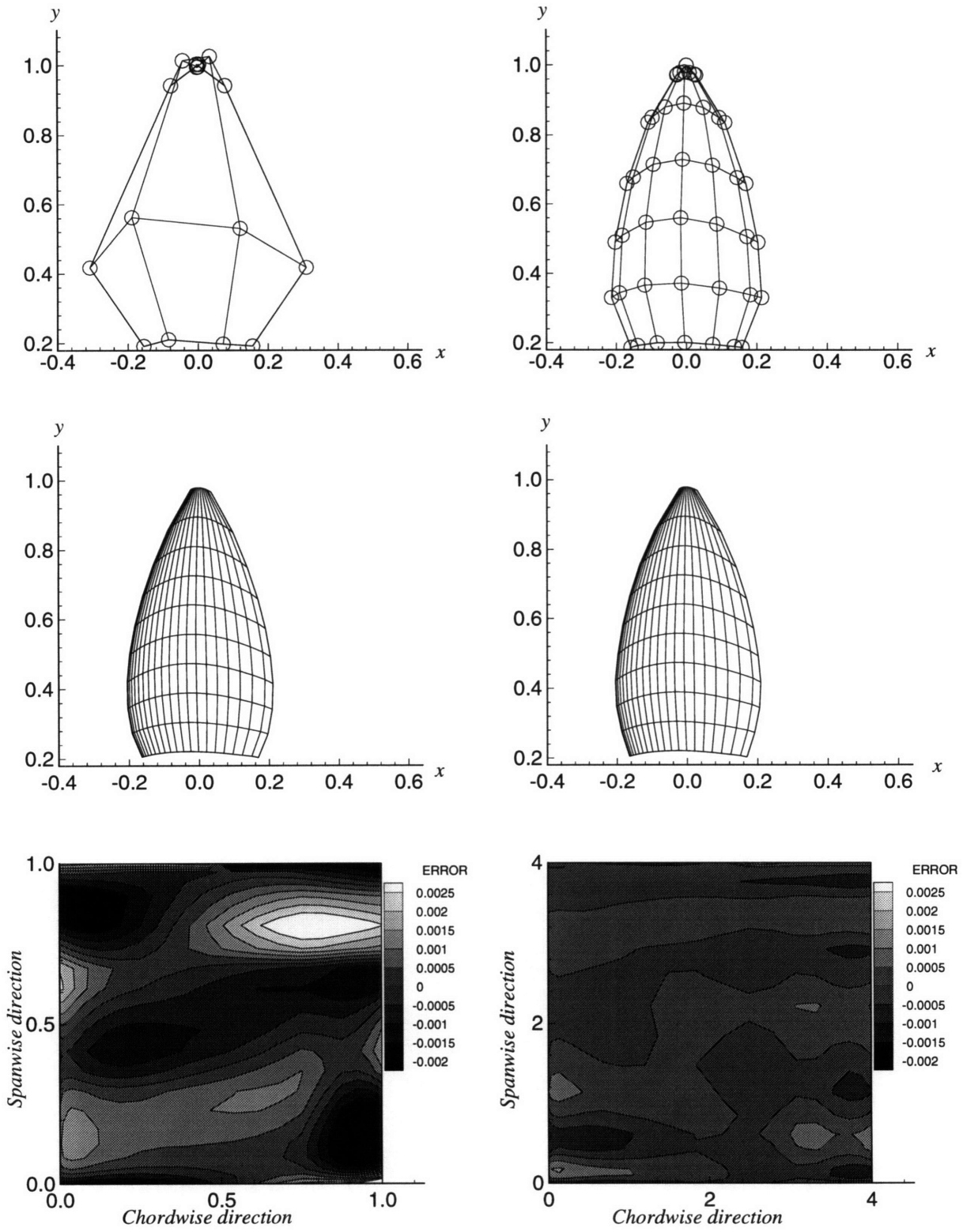

Figure 3-11: 4×4 and 7×7 B-spline vertices and contour plots of the error distribution over the blade from the original blade, $N4381$.

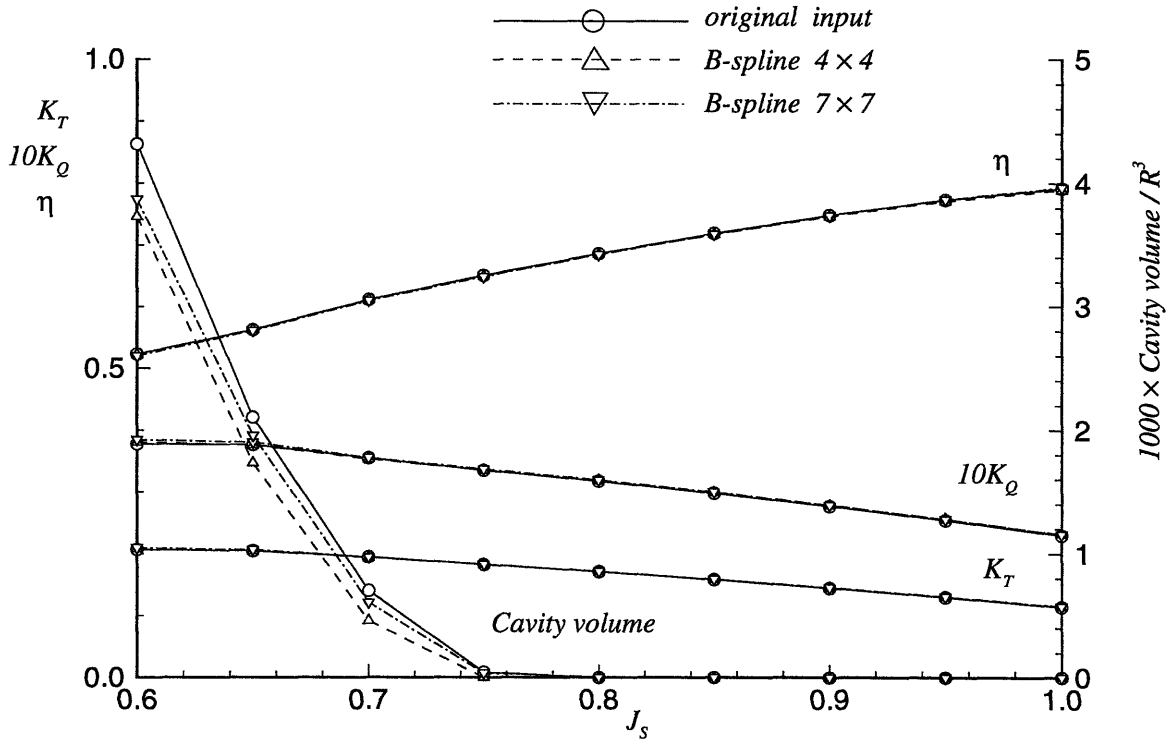

Figure 3-12: Forces and cavity volumes for original $N4381$ blade and 4×4 and 7×7 B-spline vertices defined blades

3.3.4 Geometrical Feature Extraction from B-spline Surface

Although the B-spline representation of the blade is perfectly sufficient both for an input to analysis programs and for manufacturing, it is still convenient to be able to know the geometry in terms of the traditional designers notations, such as pitch and camber. Patrikalakis and Bardis [56] developed an algorithm for the feature extraction from *NURBS*. In our case, since the singularities are placed at constant radii, it is easy to extract the geometrical feature from the mean camber surface defined by B-splines.

Using equations (3.2) and (3.3),

$$
\begin{aligned}
x_m(r) &= \frac{x_l(r) + x_t(r)}{2} \\
\theta_m(r) &= \frac{\theta_l(r) + \theta_t(r)}{2} \\
c(r) &= \sqrt{(x_t(r) - x_l(r))^2 + r^2(\theta_t(r) - \theta_l(r))^2} \\
\tan\phi(r) &= \frac{x_t(r) - x_l(r)}{r(\theta_t(r) - \theta_l(r))} \\
\tan\theta_{l,t}(r) &= \frac{z_{l,t}(r)}{y_{l,t}(r)} \\
s(r,s) &= \frac{r\cos\phi(r)(\theta_c(r,s) - \theta_m(r)) - \sin\phi(r)(x_m(r) - x_c(r,s))}{c(r)} + \frac{1}{2} \\
f(r,s) &= \frac{x_m(r) - x_c(r,s) + c(r)(s(r,s) - 1/2)\sin\phi(r)}{\cos\phi(r)}
\end{aligned}
\tag{3.11}
$$

Chapter 4

The Design Method

The present design method couples the numerical optimization scheme described in Chapter 2 and the unsteady vortex and source lattice cavitating flow analysis method, *HPUF-3A*, described in Chapter 3. The corresponding program is designated as *CAVOPT-3D*.

HPUF-3A provides the objective function, which is to be minimized, and the constraints functions. For example, for the torque minimization problem for a given thrust, the objective function would be the torque, and the constraint function would be given in terms of thrust.

$$\begin{aligned} f(\boldsymbol{x}) &= K_Q(\boldsymbol{x}) \\ h_1(\boldsymbol{x}) &= \frac{K_T(\boldsymbol{x}) - K_{To}}{K_{To}} \end{aligned}$$

where $K_T(\boldsymbol{x})$, $K_Q(\boldsymbol{x})$ are the thrust and torque coefficients, respectively, with $\boldsymbol{x}$ being the design variable vector that defines the blade geometry. K_{To} is the required thrust coefficient. Notice that the equality constraint is normalized on its required value, K_{To}, in this case, as explained in section 2.4.

4.1 The Algorithm

A flow chart of the algorithm is shown in Figures 4-1 and 4-2. It starts with an initial blade geometry represented by an n component design variable vector $\boldsymbol{x}_o$.

The first stage is to obtain linear approximations of the objective function and constraint functions. *HPUF-3A* is run for the following $1+n$ geometries to obtain the coefficients of the linear functions in terms of the design variables.

$$\boldsymbol{x}_j = \boldsymbol{x}_o + \lambda \boldsymbol{e}_j \ , \quad j = 0, 1, \ldots, n \tag{4.1}$$

where λ is a small specified positive number, usually taken equal to 0.01 in *CAVOPT-3D*, and $\boldsymbol{e}_j$ is a unit vector whose j-th element is 1. $\boldsymbol{e}_o$ is the zero vector.
Each $\boldsymbol{x}_j$ corresponds to a blade geometry slightly different from the initial guess.

$$\begin{aligned}
f(\boldsymbol{x}) &= F_f + \boldsymbol{x}^T \boldsymbol{G}_f \\
g_1(\boldsymbol{x}) &= F_{g_1} + \boldsymbol{x}^T \boldsymbol{G}_{g_1} \\
g_2(\boldsymbol{x}) &= F_{g_2} + \boldsymbol{x}^T \boldsymbol{G}_{g_2} \\
&\vdots \\
g_m(\boldsymbol{x}) &= F_{g_m} + \boldsymbol{x}^T \boldsymbol{G}_{g_m} \\
h_1(\boldsymbol{x}) &= F_{h_1} + \boldsymbol{x}^T \boldsymbol{G}_{h_1} \\
h_2(\boldsymbol{x}) &= F_{h_2} + \boldsymbol{x}^T \boldsymbol{G}_{h_2} \\
&\vdots \\
h_l(\boldsymbol{x}) &= F_{h_l} + \boldsymbol{x}^T \boldsymbol{G}_{h_l} \\
X &= \{\boldsymbol{x}_o, \boldsymbol{x}_1, \ldots, \boldsymbol{x}_n\}^T
\end{aligned} \tag{4.2}$$

where $\boldsymbol{x}$ is the design variable vector, $F_f, \boldsymbol{G}_f, F_{g_1}, \boldsymbol{G}_{g_1}, F_{g_2}, \boldsymbol{G}_{g_2}, \ldots, F_{h_l}, \boldsymbol{G}_{h_l}$ are the coefficients of the linear functions. This corresponds to the first order Taylor series expansions around the initial guess $\boldsymbol{x}_o$, if $F_f, F_{g_1}, \ldots, F_{h_l}$ are taken as the function

values at $\boldsymbol{x}_o$. For example,

$$F_f \approx f(\boldsymbol{x}_o) \tag{4.3}$$

$$\boldsymbol{G}_f \approx \frac{\partial f(\boldsymbol{x}_o)}{\partial x_i} = \begin{bmatrix} \frac{\partial f(\boldsymbol{x}_o)}{\partial x_1} \\ \frac{\partial f(\boldsymbol{x}_o)}{\partial x_2} \\ \vdots \\ \frac{\partial f(\boldsymbol{x}_o)}{\partial x_n} \end{bmatrix} \tag{4.4}$$

X is a set that has $1+n$ geometries. The procedures up to this point is the initialization of the linear optimization, as noted in Figure 4-1.

The minimization problem (2.1) is then solved numerically for the linear objective and constraint functions to give an improved geometry $\boldsymbol{x}_k$. The maximum change of each element of $\boldsymbol{x}$ is limited to a specified number, δ, which is usually taken equal to 0.01 in *CAVOPT-3D*. $\boldsymbol{x}_k$ is added to the set X and *HPUF-3A* is run for this $\boldsymbol{x}_k$. The iteration counter k is increased by 1. Since X has now $2+n$ elements, determining the coefficients of the linear functions would be an over-determined problem. In the present algorithm, only the most resent $1+n$ geometries are used to determine the coefficients. Geometries not used for the determination of the coefficients are stored in a memory for later use. For those newly defined functions the minimization problem is again solved to give a new solution $\boldsymbol{x}_k$. This process is repeated $n(n+1)/2$ times until the set X has $N = 1+n+n(n+1)/2$ elements. The linear optimizations just done may be regarded as the initialization of the quadratic optimizations in the final step. From this set X, quadratic approximations of $f(\boldsymbol{x})$, $g_i(\boldsymbol{x})$, $h_i(\boldsymbol{x})$ may be obtained.

$$\begin{aligned} f(\boldsymbol{x}) &= F_f + \boldsymbol{x}^T \boldsymbol{G}_f + \frac{1}{2}\boldsymbol{x}^T \boldsymbol{H}_f \boldsymbol{x} \\ g_1(\boldsymbol{x}) &= F_{g_1} + \boldsymbol{x}^T \boldsymbol{G}_{g_1} + \frac{1}{2}\boldsymbol{x}^T \boldsymbol{H}_{g_1} \boldsymbol{x} \\ g_2(\boldsymbol{x}) &= F_{g_2} + \boldsymbol{x}^T \boldsymbol{G}_{g_2} + \frac{1}{2}\boldsymbol{x}^T \boldsymbol{H}_{g_2} \boldsymbol{x} \\ &\vdots \end{aligned}$$

$$
\begin{aligned}
g_m(\boldsymbol{x}) &= F_{g_m} + \boldsymbol{x}^T \boldsymbol{G}_{g_m} + \frac{1}{2}\boldsymbol{x}^T \boldsymbol{H}_{g_m} \boldsymbol{x} \\
h_1(\boldsymbol{x}) &= F_{h_1} + \boldsymbol{x}^T \boldsymbol{G}_{h_1} + \frac{1}{2}\boldsymbol{x}^T \boldsymbol{H}_{h_1} \boldsymbol{x} \\
h_2(\boldsymbol{x}) &= F_{h_2} + \boldsymbol{x}^T \boldsymbol{G}_{h_2} + \frac{1}{2}\boldsymbol{x}^T \boldsymbol{H}_{h_2} \boldsymbol{x} \\
&\vdots \\
h_l(\boldsymbol{x}) &= F_{h_l} + \boldsymbol{x}^T \boldsymbol{G}_{h_l} + \frac{1}{2}\boldsymbol{x}^T \boldsymbol{H}_{h_l} \boldsymbol{x} \\
X &= \{\boldsymbol{x}_o, \boldsymbol{x}_1, \ldots, \boldsymbol{x}_{n+n(n+1)/2}\}^T
\end{aligned}
\tag{4.5}
$$

where $F_f, \boldsymbol{G}_f, \boldsymbol{H}_f, F_{g_1}, \boldsymbol{G}_{g_1}, \boldsymbol{H}_{g_1}, F_{g_2}, \boldsymbol{G}_{g_2}, \boldsymbol{H}_{g_2}, \ldots, F_{h_l}, \boldsymbol{G}_{h_l}, \boldsymbol{H}_{h_l}$ are the coefficients of the quadratic functions in terms of the design variables. $\boldsymbol{H}_f, \boldsymbol{H}_{g_1}, \ldots, \boldsymbol{H}_{h_l}$ will eventually be approximations of the Hessian matrices near the optimum solution. For instance,

$$
\boldsymbol{H}_{h_1} \approx \frac{\partial h_1}{\partial x_i \partial x_j} = \begin{bmatrix}
\frac{\partial h_1}{\partial x_1 \partial x_1} & \frac{\partial h_1}{\partial x_1 \partial x_2} & \cdots & \frac{\partial h_1}{\partial x_1 \partial x_n} \\
\frac{\partial h_1}{\partial x_2 \partial x_1} & \frac{\partial h_1}{\partial x_2 \partial x_2} & \cdots & \frac{\partial h_1}{\partial x_2 \partial x_n} \\
\vdots & \vdots & \cdots & \vdots \\
\frac{\partial h_1}{\partial x_n \partial x_1} & \frac{\partial h_1}{\partial x_n \partial x_2} & \cdots & \frac{\partial h_1}{\partial x_n \partial x_n}
\end{bmatrix}
\tag{4.6}
$$

The minimization problem is solved for the quadratic functions. The new solution $\boldsymbol{x}_k$ is again added to the set X and the $\boldsymbol{x}_i$, which is far from the optimum solution, is removed from X. This way, X would always have N elements. However, it has been found that the matrix that is to be inverted to give the coefficients of the quadratic functions is often close to singular. To remedy this ill-conditioned problem, no elements are removed from the set X until it has $N + n$ elements. After the number of elements in X becomes $N + n$, one element is removed at every iteration. Thus, hereinafter, X has always $N + n$ elements. The coefficients of the quadratic functions are computed by the least squares method.

The element $\boldsymbol{x}_i$ removed at each iteration after this point is determined in the following way.

The basic idea is to remove an element far away from the current optimum solution.

Stage 1	first N iterations	$X = X \cup \{\boldsymbol{x}\} - \{\boldsymbol{x}_i\}$ $\boldsymbol{x}_i$ is the earliest $\boldsymbol{x}$ in the set X
Stage 2	next $2N$ iterations	$X = X \cup \{\boldsymbol{x}\} - \{\boldsymbol{x}_i\}$ $\boldsymbol{x}_i$ is the $\boldsymbol{x}$ corresponding to the largest $f(\boldsymbol{x})$ (remember $f(\boldsymbol{x})$ must be minimized)
Stage 3	after $3N$ iterations	$X = X \cup \{\boldsymbol{x}\}$ The number of elements in X increases

During Stage 1, all the elements obtained from the linear approximation of the functions are replaced by the solutions from the quadratic approximations. Stage 3 helps smooth out the functions, $f(\boldsymbol{x})$, $g_i(\boldsymbol{x})$ and $h_i(\boldsymbol{x})$, and improves the convergence. Otherwise the solution may oscillate without any improvement in $f(\boldsymbol{x})$. The iteration is repeated until the change in $\boldsymbol{x}$ becomes less than a specified tolerance, ε.

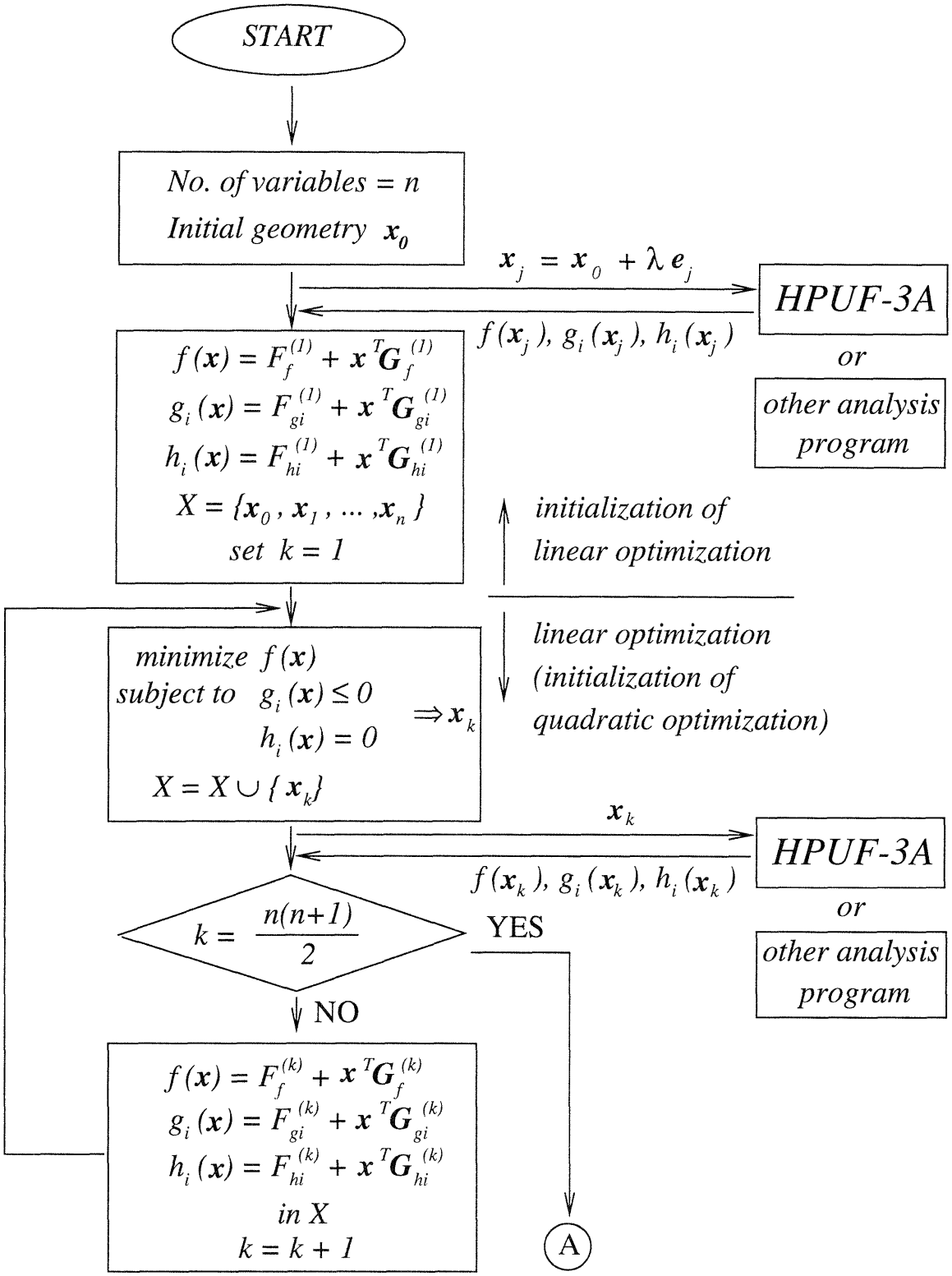

Figure 4-1: Flow chart of *CAVOPT-3D*

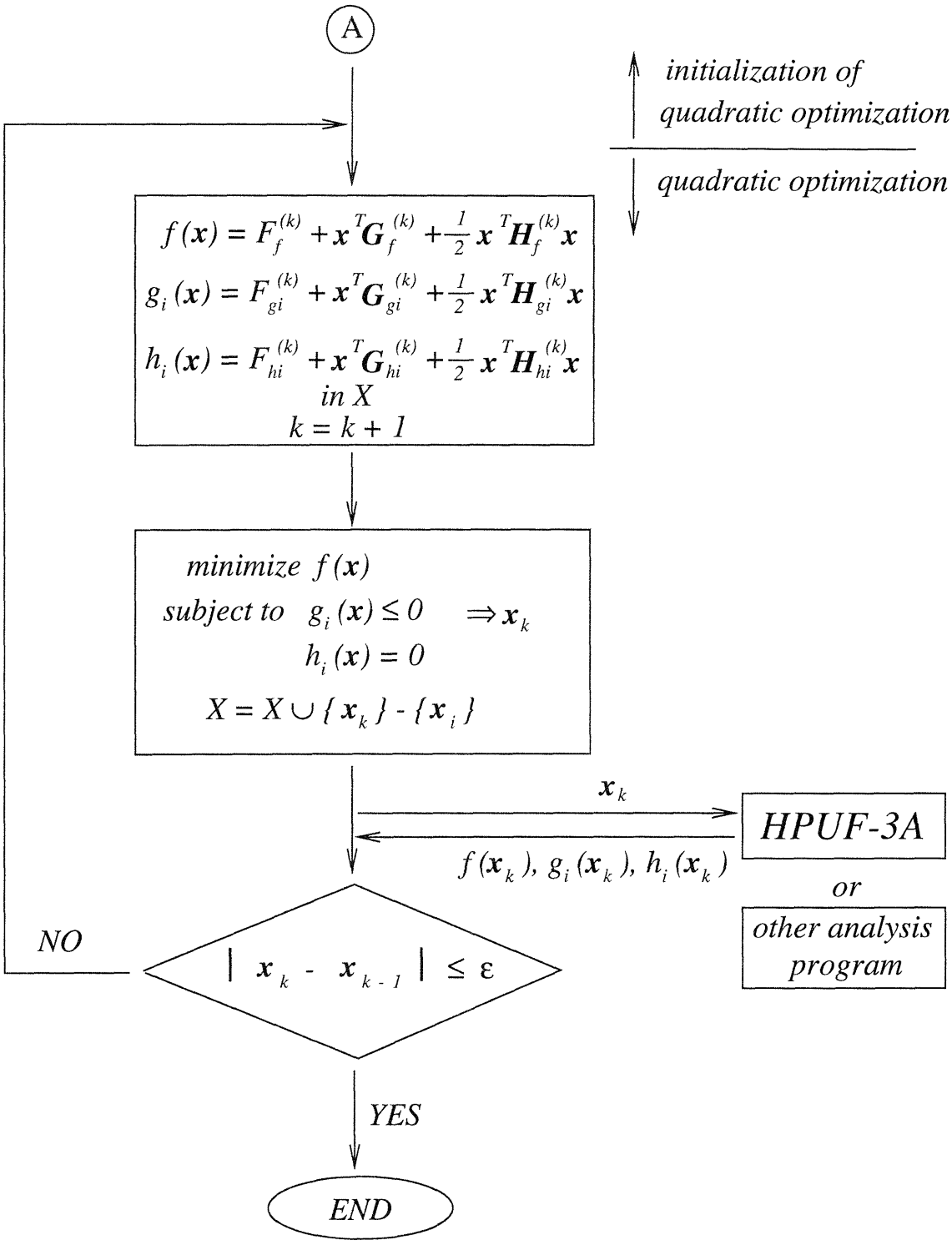

Figure 4-2: Flow chart of *CAVOPT-3D*, continued

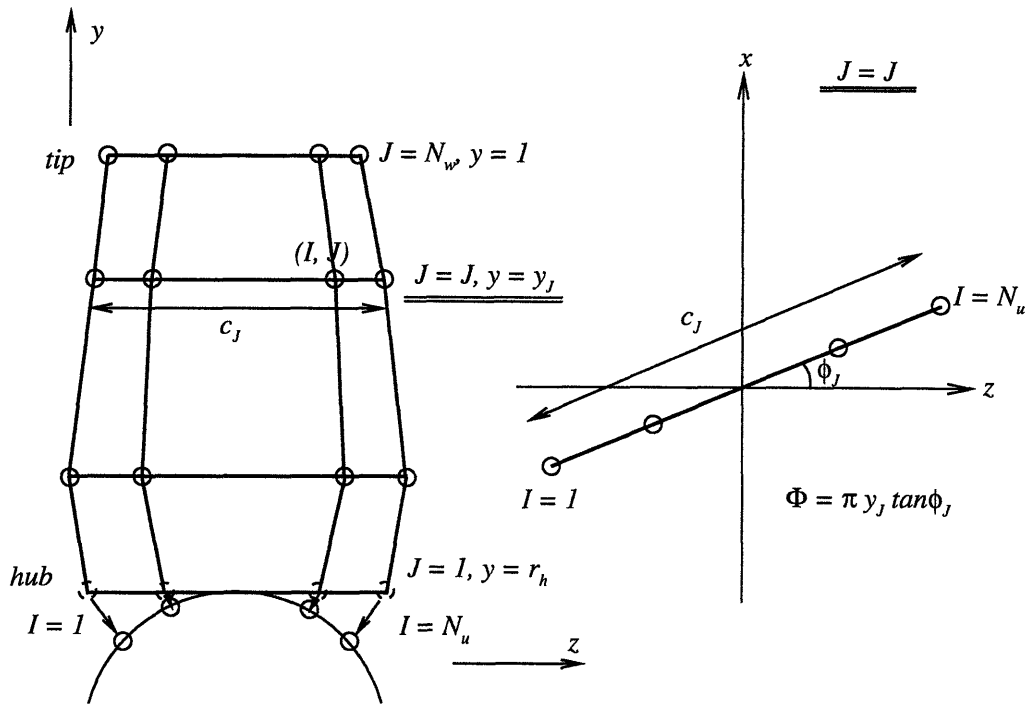

Figure 4-3: Construction of B-spline polygon net for initial propeller geometry

4.2 Initial Blade Geometry

Blade geometry is defined by a B-spline polygon net, as described in section 3.3. The net consists of N_u chordwise by N_w spanwise B-spline control points (vertices). The indices I and J are used for the "chordwise" and "spanwise" directions [1], respectively. Thus, I runs from 1 to N_u and J from 1 to N_w. Figure 4-3 shows how an initial B-spline polygon net is created.

Consider a particular chordwise strip, which is denoted by the index J. This has N_u vertices that form a straight line segment. This segment has a total length c_J and lies in a certain $y = y_J$ (constant) plane. It has an angle ϕ_J measured from z axis as shown in Figure 4-3. y_J is determined from the cosine spacing between $y_1 = r_h$ ("hub" radius) and $y_{N_w} = 1$ (tip).

[1] These sections are not chordwise or spanwise according to the traditional sense, where the sections are placed along cylindrical surfaces

$$y_J = (1 - r_h)\frac{1 - \cos\left(\frac{\pi(J-1)}{N_w - 1}\right)}{2} + r_h, \qquad J = 1, \ldots, N_w \tag{4.7}$$

ϕ_J is defined by

$$\pi y_J \tan\phi_J = \Phi = \text{constant} \tag{4.8}$$

The chordwise spacing is also cosine spacing, therefore

$$\begin{aligned}
d^o_{IJ} &= (x^o_{IJ}, y^o_{IJ}, z^o_{IJ})^T \\
x^o_{IJ} &= -\frac{c_J \cos(\frac{\pi(I-1)}{N_u - 1})}{2} \sin\phi_J \\
y^o_{IJ} &= y_J = (1 - r_h)\frac{1 - \cos(\frac{\pi(J-1)}{N_w - 1})}{2} + r_h \\
z^o_{IJ} &= -\frac{c_J \cos(\frac{\pi(I-1)}{N_u - 1})}{2} \cos\phi_J, \qquad I = 1, \ldots, N_u,\ J = 2, \ldots, N_w - 1
\end{aligned} \tag{4.9}$$

Finally, the vertices for $J = 1$ are moved radially inward so that they are right on the hub surface. Similarly, the tip vertices ($J = N_w$) are moved so that they are on $r = \sqrt{y^2_{I,N_w} + z^2_{I,N_w}} = 1$. Notice that this initial B-spline polygon does not introduce skew or rake.

$$\begin{aligned}
x^o_{I,1} &= -\frac{c_1 \cos(\frac{\pi(I-1)}{N_u - 1})}{2} \sin\phi_1 \\
y^o_{I,1} &= \frac{r_h^2}{\sqrt{r_h^2 + c_1^2 \cos^2(\frac{\pi(I-1)}{N_u - 1}) \cos^2\phi_1/4}} \qquad I = 1, \ldots, N_u \\
z^o_{I,1} &= -\frac{c_1 r_h \cos(\frac{\pi(I-1)}{N_u - 1}) \cos\phi_1}{2\sqrt{r_h^2 + c_1^2 \cos^2(\frac{\pi(I-1)}{N_u - 1}) \cos^2\phi_1/4}}
\end{aligned} \tag{4.10}$$

$$x^o_{I,N_w} = -\frac{c_{N_w} \cos(\frac{\pi(I-1)}{N_u - 1})}{2} \sin\phi_{N_w}$$

$$y^o_{I,N_w} = \frac{1}{\sqrt{1 + c^2_{N_w} \cos^2(\frac{\pi(I-1)}{N_u-1}) \cos^2 \phi_{N_w}/4}} \qquad I = 1, \ldots, N_u \qquad (4.11)$$

$$z^o_{I,N_w} = -\frac{c_{N_w} \cos(\frac{\pi(I-1)}{N_u-1}) \cos \phi_{N_w}}{2\sqrt{1 + c^2_{N_w} \cos^2(\frac{\pi(I-1)}{N_u-1}) \cos^2 \phi_{N_w}/4}}$$

4.3 Design Variables

The B-spline polygon net defines the blade geometry without skew. Skew is added independent of the blade geometry defined by the polygon. The vertices move at each optimization iteration to give an improved new blade geometry. The direction of the movement of each vertex is decomposed into two directions, the direction normal to the initial leading edge-trailing edge line on a horizontal plane (with the y_J value fixed) and the chordwise direction. When a chordwise vertex line stretches, the movement of the vertices in the chordwise direction is determined according to the cosine spacing. The chord length at the tip is kept constant. The tip vertices simply rotate without change in camber. There is a case in the design where the radial chord length distribution is given. In this case, no vertices are allowed to move in the chordwise direction. The vertices at the leading edge and the trailing edge on a particular chordwise strip always move by the same amount in the opposite direction, thus there will be no skew or rake after the movement. Again, hub and tip vertices are moved so that they are on the hub and tip surface, respectively.

The number of design variables, therefore, is

$n = (N_u - 1) \times (N_w - 1) + 1$	when chord length is given
$n = N_u \times (N_w - 1) + 1$	when chord length is determined

If linear skew is included, n is increased by 1 in either case.
The amount of the movement of the vertices is the design variable $\boldsymbol{x} = (x_1, \ldots, x_n)^T$ and is illustrated in Figure 4-4. This is also shown more schematically in Figure 4-5. The coordinates of the new vertices, $\boldsymbol{d}_{I,J} = (x_{I,J}, y_{I,J}, z_{I,J})^T$, corresponding to $\boldsymbol{x}$, using the initial vertices, $\boldsymbol{d}^o_{I,J} = (x^o_{I,J}, y^o_{I,J}, z^o_{I,J})^T$, are listed in Appendix D.

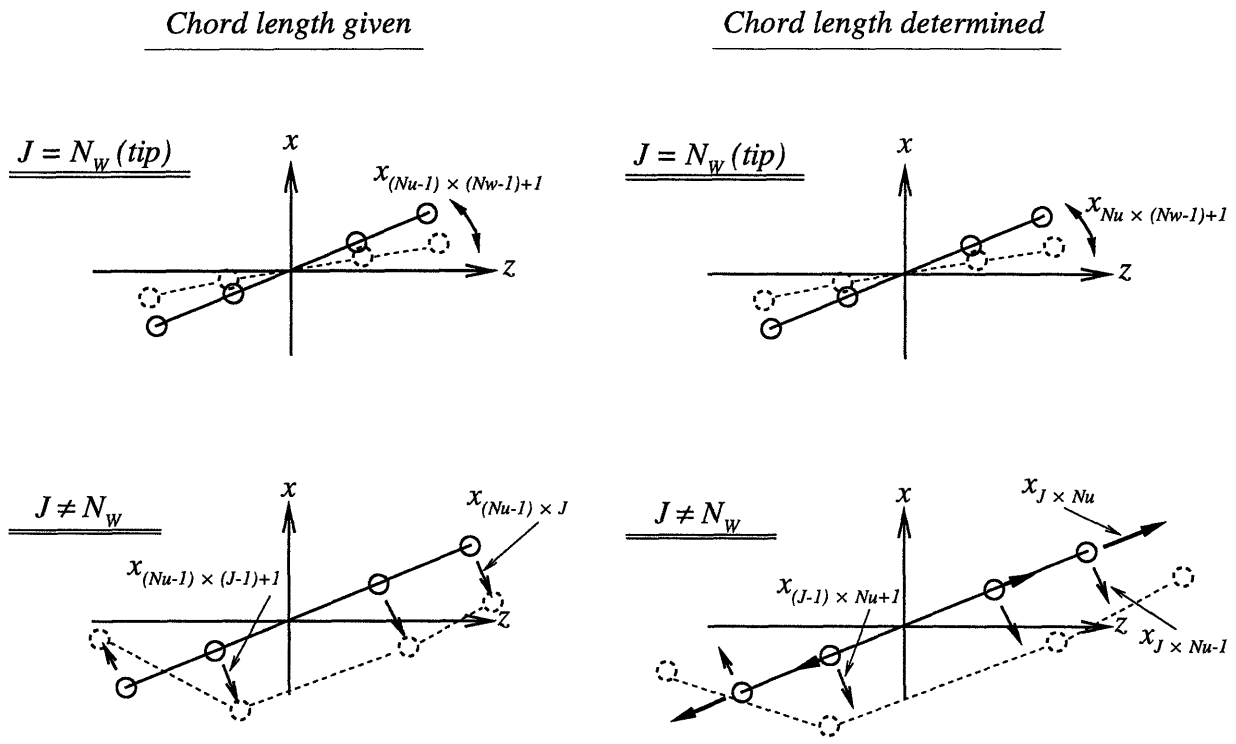

Figure 4-4: Design variables and B-spline vertices movement

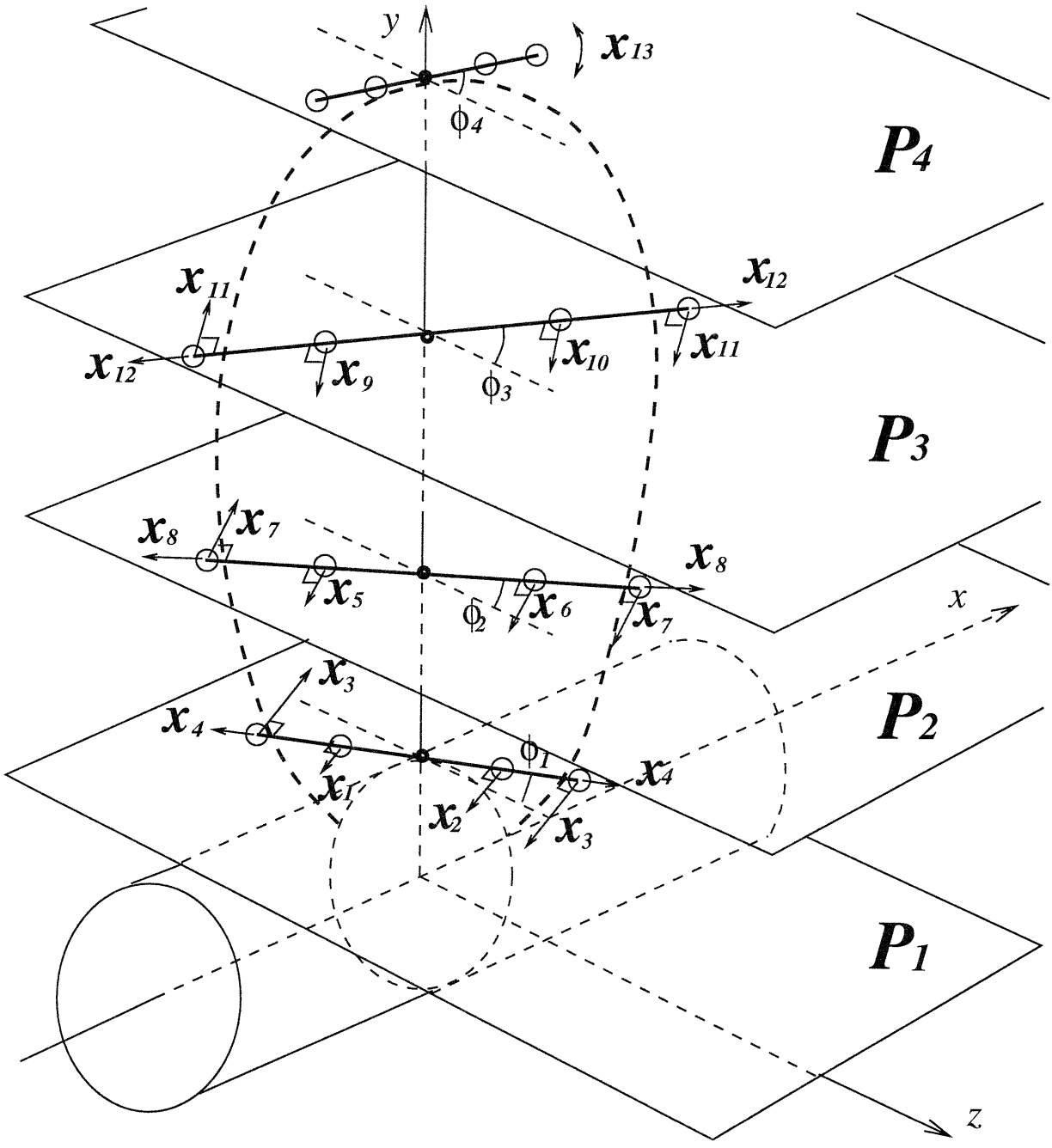

Figure 4-5: Initial B-spline polygon vertices, design variables, and vertex movement (4×4 vertices)

4.4 Numerical Validation

For the propeller design, the functions, $f(\boldsymbol{x})$, $g_i(\boldsymbol{x})$, or $h_i(\boldsymbol{x})$ are not known explicitly. The algorithm is first validated by applying it to some known functions taken from [26]. This is done by simply replacing *HPUF-3A* with a routine that computes the function values.

4.4.1 Choice of x_i for the Removal from the Set X

The algorithm was first tested for a simple case where $f(\boldsymbol{x})$ is a function of two variables and there are no constraints [5].

$$\begin{aligned} \boldsymbol{x} &= (x_1, x_2)^T \\ f(\boldsymbol{x}) &= (x_1 - 1)^4 + (x_1 - 1)^2 x_2^2 + (x_2 - 2)^2 \end{aligned} \tag{4.12}$$

A subroutine which computes $f(\boldsymbol{x})$, given $\boldsymbol{x}$, replaces *HPUF-3A* in the flow chart shown in Figures 4-1 and 4-2. The optimum solution is obviously

$$\bar{\boldsymbol{x}} = (1, 2)^T \tag{4.13}$$

The algorithm starts with $\boldsymbol{x}_o = (3, 3)^T$.

The top plot in Figure 4-6 is a contour of $f(\boldsymbol{x})$. The middle figure is a contour plot of the quadratic approximation of $f(\boldsymbol{x})$ after the final iteration of the present method. It is seen that the optimum point $\bar{\boldsymbol{x}} = (1, 2)^T$ is captured locally by the quadratic approximation.

The bottom figure shows a contour of the quadratic approximation of $f(\boldsymbol{x})$ from the algorithm *without* removing any points ever from the set X. A converged solution $\bar{\boldsymbol{x}} = (0.893, 1.403)^T$ was obtained, but it is clearly wrong. The convergence history of the variables, x_1 and x_2, and the function, $f(\boldsymbol{x})$, for the present method with/without removing $\boldsymbol{x}$ at iterations is shown in Figure 4-7. Several tolerances, ε, for the convergence are indicated in the figure. The stopping criterion is:

$$\frac{\sqrt{\sum_{i=1}^{n}\left(\frac{x_i^{(k+1)}-x_i^{(k)}}{x_i^{(k+1)}}\right)^2}}{n} \leq \varepsilon$$

Since the quadratic approximation is supposed to be valid only locally near the optimum point, the points far away from this point should not be used for the function approximation.

4.4.2 Functions with Constraints

Some other functions [26] tested are shown below.

Test Problem No. 4-1	
Function to be minimized	$f(\boldsymbol{x}) = (x_1-1)^2 + (x_1-x_2)^2 + (x_3-x_4)^4 + (x_4-x_5)^4$ $\boldsymbol{x} = (x_1, x_2, x_3, x_4, x_5)^T$
Equality constraints	$h_1(\boldsymbol{x}) = x_1 + x_2^2 + x_3^3 - 2 - 3\sqrt{2}$ $h_2(\boldsymbol{x}) = x_2 - x_3^2 + x_4 + 2 - 2\sqrt{2}$ $h_3(\boldsymbol{x}) = x_1 x_5 - 2$
Inequality constraints	none
Starting point	$\boldsymbol{x}_o = (2,2,2,2,2)^T$ $f(\boldsymbol{x}_o) = 1$
Solution from [26]	$\bar{\boldsymbol{x}} = (1.191, 1.363, 1.473, 1.635, 1.679)$ $f(\bar{\boldsymbol{x}}) = 0.07878$
Present method	$\bar{\boldsymbol{x}} = (1.191, 1.363, 1.473, 1.644, 1.680)$ $f(\bar{\boldsymbol{x}}) = 0.07878$

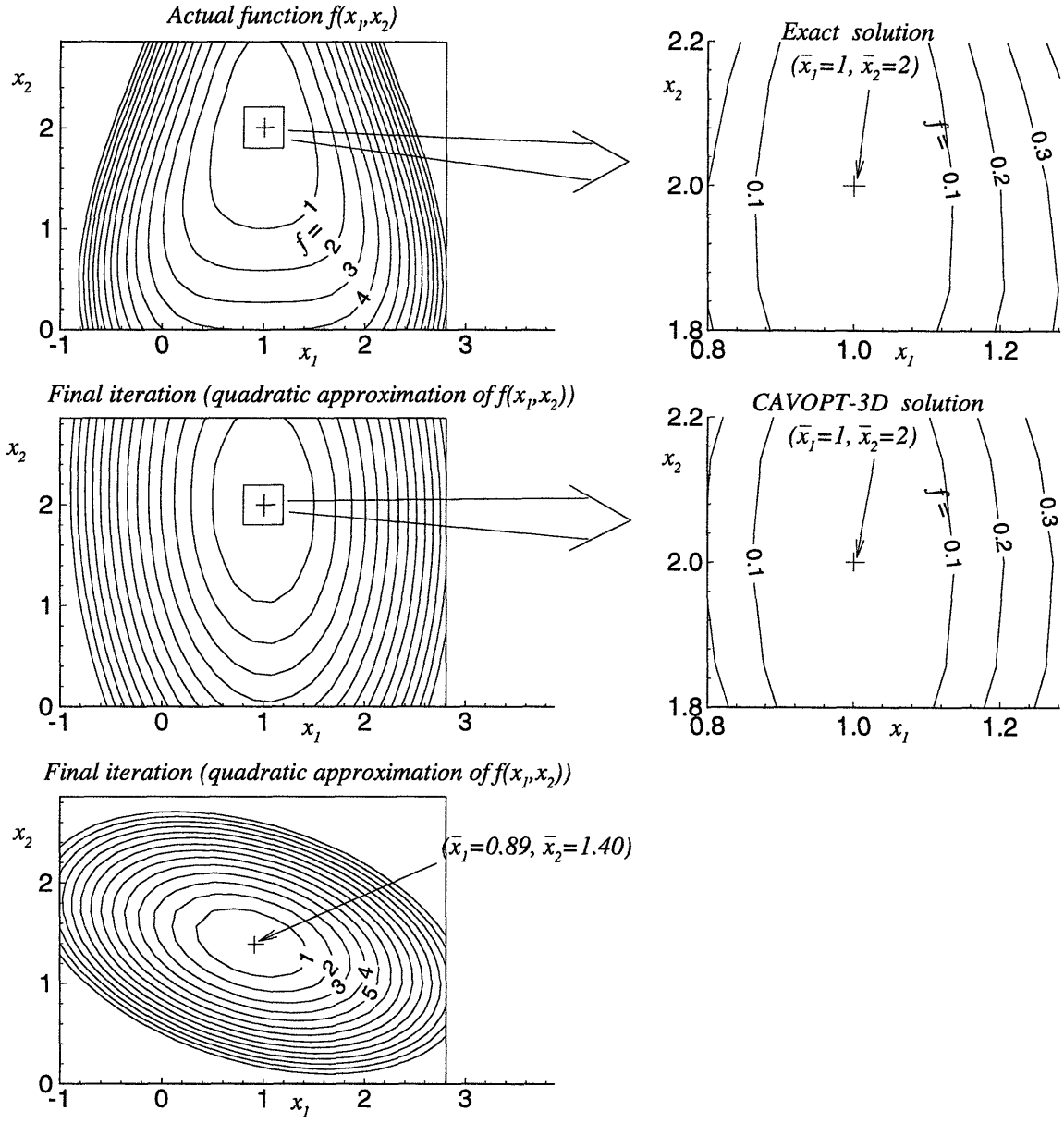

Figure 4-6: Contour plots of $f(\boldsymbol{x}) = (x_1 - 1)^4 + (x_1 - 1)^2 x_2^2 + (x_2 - 2)^2$ and quadratic approximation of $f(\boldsymbol{x})$, top : $f(\boldsymbol{x})$, middle : quadratic approximation of $f(\boldsymbol{x})$ (present algorithm) , bottom : quadratic approximation of $f(\boldsymbol{x})$ (without $\boldsymbol{x}$ removal : converges to a wrong answer !)

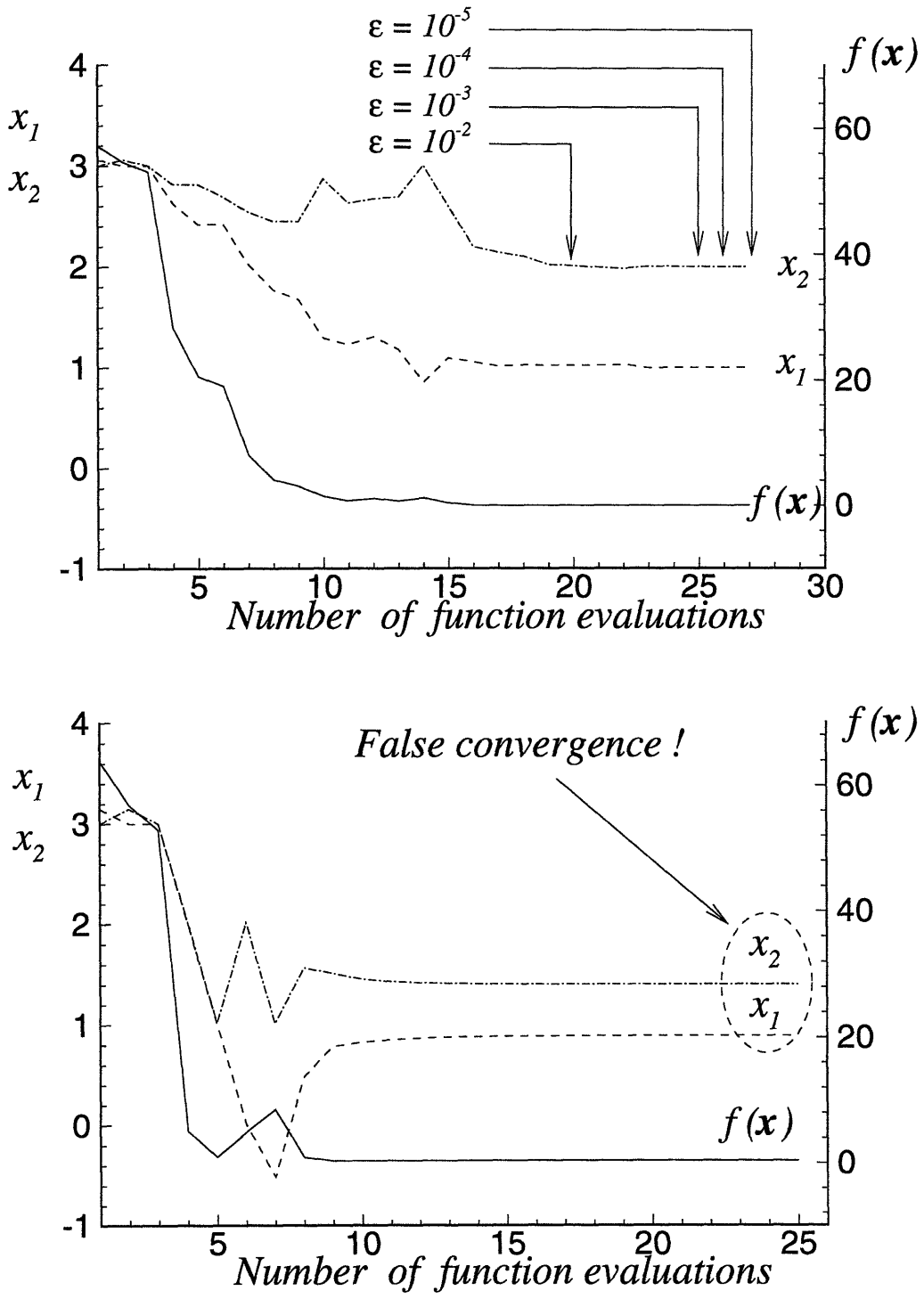

Figure 4-7: Convergence history of the variables and the function $f(\boldsymbol{x}) = (x_1 - 1)^4 + (x_1 - 1)^2 x_2^2 + (x_2 - 2)^2$, top : present method $(\bar{x}_1, \bar{x}_2) = (1.0, 2.0), f(\boldsymbol{x}) = 0.0$, bottom : without $\boldsymbol{x}$ removal $(\bar{x}_1, \bar{x}_2) = (0.89, 1.40), f(\boldsymbol{x}) = 0.379$

Test Problem No. 4-2	
Function to be minimized	$f(\boldsymbol{x}) = x_1^2 + x_2^2 + x_1x_2 - 14x_1 - 16x_2 + (x_3 - 10)^2$ $+4(x_4 - 5)^2 + (x_5 - 3)^2 + 2(x_6 - 1)^2 + 5x_7^2$ $+7(x_8 - 11)^2 + 2(x_9 - 10)^2 + (x_{10} - 7)^2 + 45$ $\boldsymbol{x} = (x_1, x_2, x_3, x_4, x_5, x_6, x_7, x_8, x_9, x_{10})^T$
Equality constraints	none
Inequality constraints	$g_1(\boldsymbol{x}) = -105 + 4x_1 + 5x_2 - 3x_7 + 9x_8$ $g_2(\boldsymbol{x}) = 10x_1 - 8x_2 - 17x_7 + 2x_8$ $g_3(\boldsymbol{x}) = -8x_1 + 2x_2 + 5x_9 - 2x_{10} - 12$ $g_4(\boldsymbol{x}) = 3(x_1 - 2)^2 + 4(x_2 - 3)^2 + 2x_3^2 - 7x_4 - 120$ $g_5(\boldsymbol{x}) = 5x_1^2 + 8x_2 + (x_3 - 6)^2 - 2x_4 - 40$ $g_6(\boldsymbol{x}) = 0.5(x_1 - 8)^2 + 2(x_2 - 4)^2 + 3x_5^2 - x_6 - 30$ $g_7(\boldsymbol{x}) = x_1^2 + 2(x_2 - 2)^2 - 2x_1x_2 + 14x_5 - 6x_6$ $g_8(\boldsymbol{x}) = -3x_1 + 6x_2 + 12(x_9 - 8)^2 - 7x_{10}$
Starting point	$\boldsymbol{x}_o = (2, 3, 5, 5, 1, 2, 7, 3, 6, 10)^T$ $f(\boldsymbol{x}_o) = 753$
Solution from [26]	$\bar{\boldsymbol{x}} = (2.172, 2.364, 8.774, 5.096, 0.991, 1.431,$ $1.322, 9.829, 8.280, 8.376)^T$ $f(\bar{\boldsymbol{x}}) = 24.306$
Present method	$\bar{\boldsymbol{x}} = (2.173, 2.362, 8.773, 5.091, 0.989, 1.427,$ $1.323, 9.830, 8.278, 8.366)^T$ $f(\bar{\boldsymbol{x}}) = 24.307$

The convergence history of the design variables, $\boldsymbol{x}$, the objective function, $f(\boldsymbol{x})$, and a constraint function, $g_1(\boldsymbol{x})$ for the problem No. 4-1 and 4-2 are shown in Figures 4-8 and 4-9, respectively.

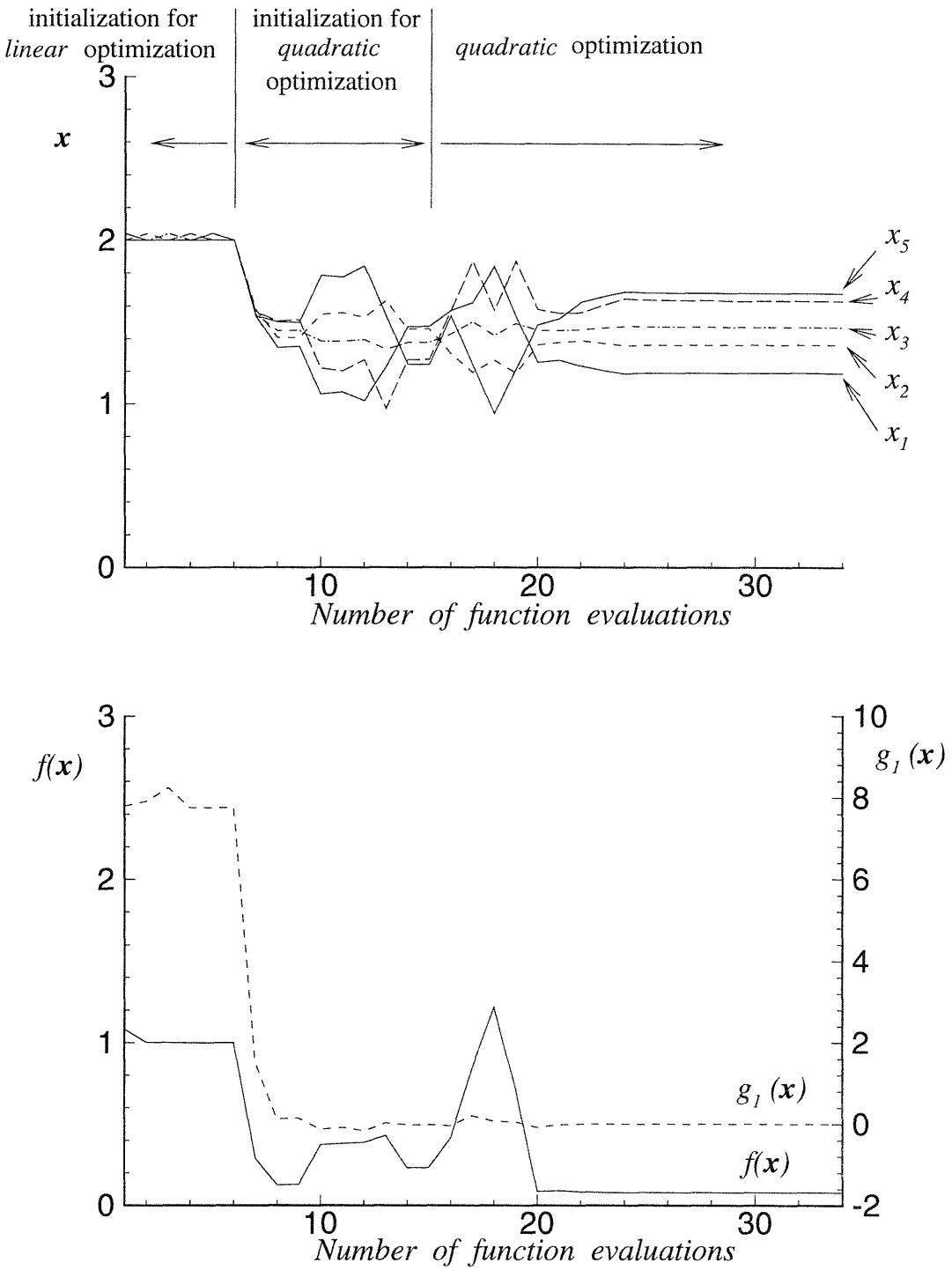

Figure 4-8: Convergence history of design variables and function values for test problem No. 4-1

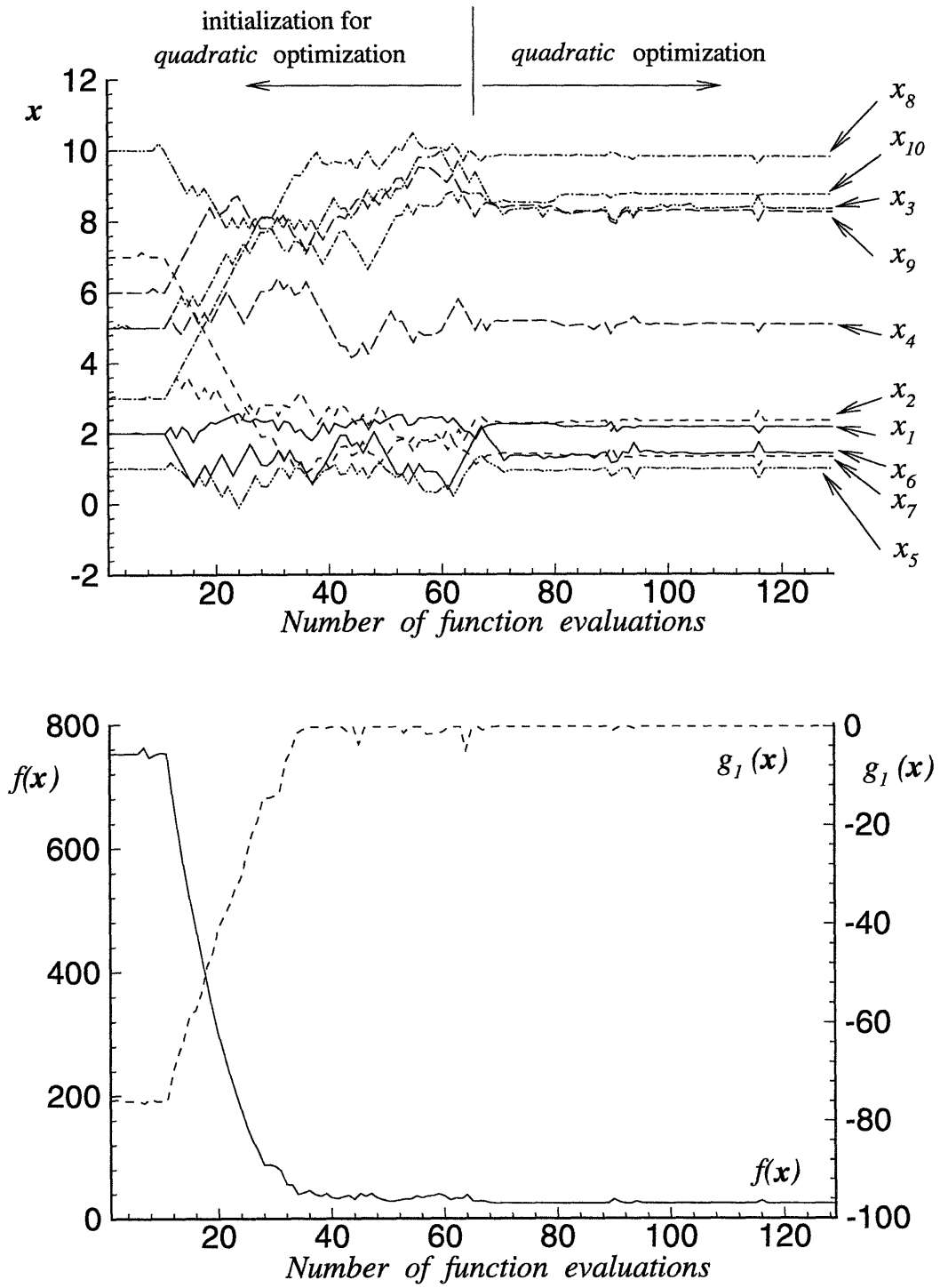

Figure 4-9: Convergence history of design variables and function values for test problem No. 4-2

Chapter 5

Design of Two Dimensional Cavitating Sections

The design algorithm described in the previous chapters was applied to the design of two dimensional cavitating hydrofoil sections.

A similar method was used to design two dimensional cavitating sections by Mishima and Kinnas [52], where the objective function and constraint functions are expressed explicitly in terms of quadratic functions of the main parameters of the hydrofoil geometry, angle of attack, and the cavity length. The coefficients of the quadratic polynomials are determined by applying the least squares method to the results obtained from the analysis method for a wide range of the geometry parameters involved. Once these quadratic functions become available, an optimization may be done very quickly for any design conditions. This method is applicable only if the number of design variables is small and running the analysis program is computationally inexpensive.

The present design method is applied to this two dimensional problem and the results are compared with the results from [52].

5.1 Statement of the Problem

The design of partially and super-cavitating two dimensional hydrofoils is considered.

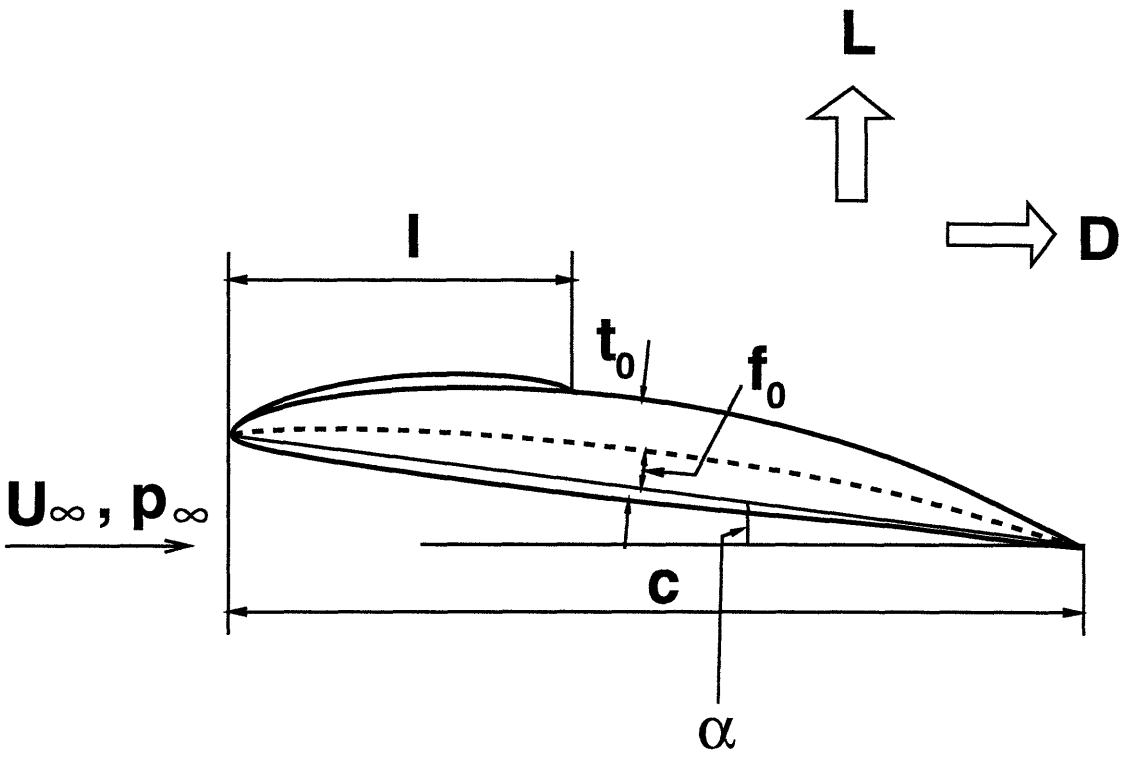

Figure 5-1: A partially cavitating hydrofoil.

The design objective is to determine the hydrofoil geometry and its operating condition (angle of attack, α), which produces the minimum drag, D, for specified design requirements. The main parameters that define the geometry of a partially cavitating hydrofoil, also shown in Figure 5-1, are:

- the chord, c
- the maximum camber, f_0
- the maximum thickness, t_0

The thickness and camber distributions along the chord are assumed to be given.

The main parameters that define the geometry of a supercavitating hydrofoil, also shown in Figure 5-2, are :

- the chord, c
- the maximum camber on the pressure side, f_0

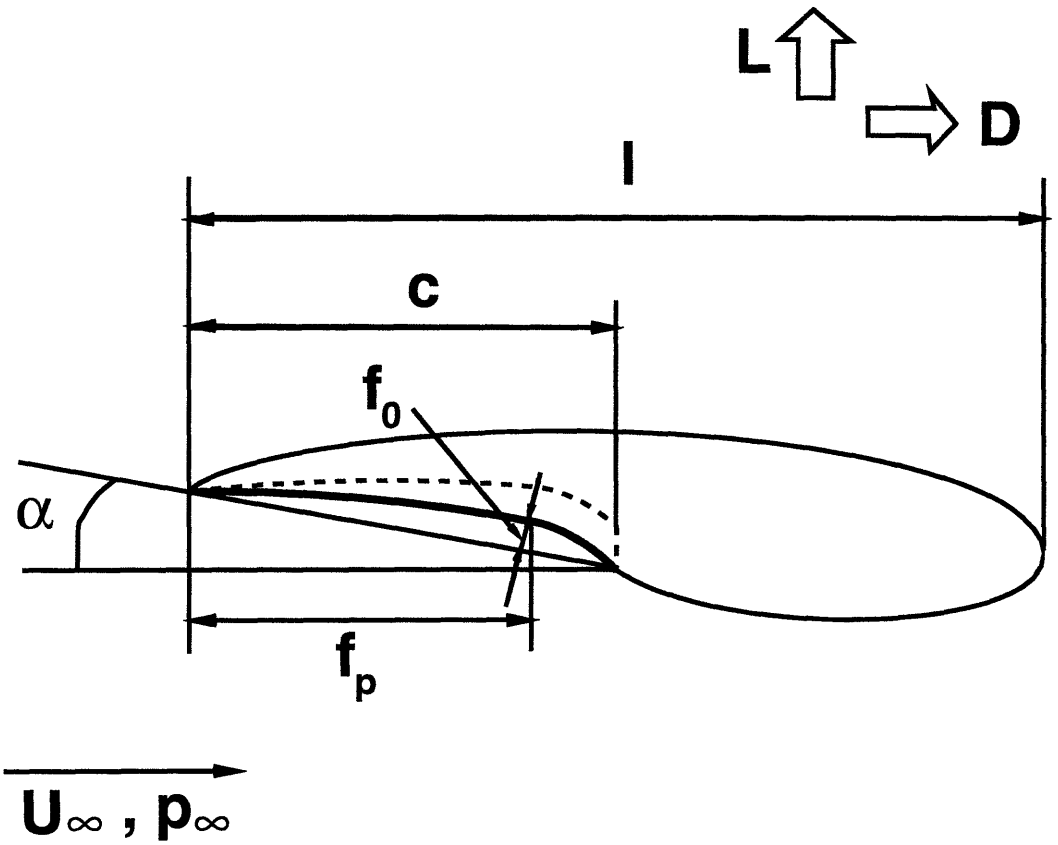

Figure 5-2: A supercavitating hydrofoil.

- location of the maximum camber, f_p

Since only the lower surface of the foil determines the hydrodynamics of supercavitating flows, the thickness is not included as a parameter. The upper surface can be placed anywhere arbitrarily inside the cavity. Thus, when computing the section modulus of a foil, the upper cavity surface is considered as the upper surface of the "compound" foil. It is reasonable to assume that the cavity always starts at the leading edge of the foil, since the supercavitating sections have a sharp leading edge. Furthermore, we deal with situations where the cavity detaches at the trailing edge of the foil on the pressure side.

The design requirements taken into consideration in this work are :

- Sectional Lift, $L_o(N/m)$

- Cavitation number, σ_o, defined as:

$$\sigma_0 = \frac{p_\infty - p_v}{\frac{1}{2}\rho U_\infty^2} \tag{5.1}$$

  where ρ is the fluid density, p_∞ is the ambient pressure, and p_v is the vapor pressure.

- Minimum section modulus of the foil, z_{min}

- Acceptable cavity length, l

- Acceptable cavity volume, V, or cavity height, h

The condition on the cavity length is necessary in order to avoid unstable cavities, usually being the long partial or short supercavities. The cavity volume/height constraint ensures acceptable positive cavity thickness (volume) in order to avoid very thin cavities (also negative thickness cavities) which either are non-physical or may turn into harmful bubble cavitation.

For the case of supercavitating sections, in addition to specifying the minimum section modulus of the compound section, the minimum allowable cavity height at the 10% of the chord length from the leading edge is specified via an inequality constraint. This ensures positive cavity thickness, as well as sufficient local strength at the sharp leading edge of the foil. An alternative to this condition would be to impose a lower limit on the magnitude of the leading edge radius of the section.

The problems are:

Partially cavitating hydrofoil

$$\begin{aligned} \text{minimize} \quad & f(\boldsymbol{x}) &&= C_D(\boldsymbol{x}) \\ \text{subject to} \quad & h_1(\boldsymbol{x}) &&= C_L(\boldsymbol{x}) - C_{L_o} = 0 \\ & h_2(\boldsymbol{x}) &&= \sigma(\boldsymbol{x}) - \sigma_o = 0 \\ & g_1(\boldsymbol{x}) &&= \frac{l}{c} - \left(\frac{l}{c}\right)_{max} \leq 0 \end{aligned} \tag{5.2}$$

$$g_2(\boldsymbol{x}) = -\frac{V(\boldsymbol{x})}{l^2} + \left(\frac{V}{l^2}\right)_{min} \leq 0$$
$$g_3(\boldsymbol{x}) = -\frac{z(\boldsymbol{x})}{c^3} + \frac{z_{min}}{c^3} \leq 0$$

where $\boldsymbol{x} = (\alpha, t_o/c, f_o/c, l/c)^T$

C_L and C_D are the lift and drag coefficients, respectively.

Supercavitating hydrofoil

$$\begin{aligned}
\text{minimize} \quad & f(\boldsymbol{x}) = C_D(\boldsymbol{x}) \\
\text{subject to} \quad & h_1(\boldsymbol{x}) = C_L(\boldsymbol{x}) - C_{L_o} = 0 \\
& h_2(\boldsymbol{x}) = \sigma(\boldsymbol{x}) - \sigma_o = 0 \\
& g_1(\boldsymbol{x}) = -\frac{l}{c} + \left(\frac{l}{c}\right)_{min} \leq 0 \\
& g_2(\boldsymbol{x}) = -\frac{z(\boldsymbol{x})}{c^3} + \frac{z_{min}}{c^3} \leq 0 \\
& g_3(\boldsymbol{x}) = -\frac{h_{10}(\boldsymbol{x})}{c} + \left(\frac{h_{10}}{c}\right)_{min} \leq 0
\end{aligned} \tag{5.3}$$

where $\boldsymbol{x} = (\alpha, f_o/c, f_p/c, l/c)^T$

h_{10} is the cavity height at 10 % from the leading edge of the foil.

5.2 Hydrodynamic Quantities

The hydrofoil lift, L, and drag, D, acting on the hydrofoil as shown in Figures 5-1 5-2 are expressed in terms of lift and drag coefficients, C_L and C_D, respectively:

$$L = \frac{1}{2}\rho U_\infty^2 c C_L \tag{5.4}$$
$$D = \frac{1}{2}\rho U_\infty^2 c C_D \tag{5.5}$$

The drag coefficient, C_D, may be decomposed into two components.

$$C_D = C_D^i + C_D^v \tag{5.6}$$

where C_D^i is the inviscid cavity drag coefficient, and C_D^v is the viscous drag coefficient.

A numerical nonlinear cavity analysis method of Kinnas and Fine [39, 40] is utilized for the inviscid hydrodynamic quantities. The shape of the cavity surface is determined iteratively using non-linear theory, with the use of a low-order potential based panel method. The inviscid forces are determined by integrating the pressures along the foil surface.

The viscous drag is determined by assuming a uniform friction coefficient, C_f, over the wetted part of the foil. C_f is expressed in terms of the Reynolds number ($Re = U_\infty c/\nu$, ν : kinematic viscosity) via the ITTC formula [8]:

$$C_f = \frac{0.075}{(log_{10}Re - 2)^2} \tag{5.7}$$

The cavity detachment point is taken to be fixed at 0.2% c in the case of partial cavitation and at the sharp leading edge in the case of supercavitation.

5.3 Numerical Solutions

In the case of partially cavitating hydrofoils, the combination of NACA a=0.8 camber form and the modified NACA66 thickness form [1] is used. The following values for the constraints are imposed:

$$\begin{aligned} C_{L_o} &= 0.593 \\ \sigma_o &= 0.6 \\ Re &= 5.6 \times 10^6 \\ \left(\frac{l}{c}\right)_{max} &= 0.4 \\ \left(\frac{V}{l^2}\right)_{min} &= 0.02 \end{aligned} \tag{5.8}$$

$$\frac{z_{min}}{c^3} = 7 \times 10^{-5}$$

In the case of supercavitating hydrofoils, the NACA 4-digit camber form [1] is used. The NACA 4-digit camber form has two parameters, which are the maximum camber-to-chord ratio f_o/c and the location of the maximum camber f_p/c, as shown in Figure 5-2. The values for the constraints are:

$$\begin{aligned} C_{L_o} &= 0.303 \\ \sigma_o &= 0.2 \\ Re &= 6.3 \times 10^6 \\ \left(\frac{l}{c}\right)_{min} &= 1.15 \\ \left(\frac{h_{10}}{c}\right)_{min} &= 0.01 \\ \frac{z_{min}}{c^3} &= 7 \times 10^{-5} \end{aligned} \tag{5.9}$$

The resulting partially cavitating foil geometry from the present method and the method of [52] are shown in Table 5.1. It is seen that the geometries from the two methods are reasonably close.

	α	t_o/c	f_o/c	l/c	L/D
Present method	2.08	0.031	0.028	0.39	88.6
Mishima & Kinnas	2.07	0.029	0.028	0.40	88.6

Table 5.1: The optimum partially cavitating foil geometries from the present method and Mishima & Kinnas [52]

The resulting supercavitating foil geometry from the present method and the method of [52] are shown in Table 5.2. The foil geometry from the present method is shown also in Figure 5-3, together with the corresponding pressure distribution on the foil. The sections designed by the two different approaches are not the same. The

method of Mishima and Kinnas [52] uses a global interpolation that covers a wider range of the geometries. The present method uses a more local interpolation and is expected to represent the actual functions more accurately.

	α	f_o/c	f_p/c	l/c	L/D
Present method	1.23	0.009	0.90	1.15	32.5
Mishima & Kinnas	1.36	0.011	0.82	1.15	31.8

Table 5.2: The optimum supercavitating foil geometries from the present method and Mishima & Kinnas [52]

	α	t_o/c	f_o/c	l/c
1	2.5	0.03	0.03	0.20
2	3.0	0.05	0.04	0.30
3	2.0	0.04	0.03	0.35
4	3.0	0.05	0.02	0.30

Table 5.3: Initial foil geometry guesses

In general, a nonlinear optimization problem is initial guess dependent. In other words, if there exist more than one local minima to the objective function, any one of these minima may be obtained depending on the initial guess. Due to the special structure of the problem, no multiple solutions were found for the range of lift and cavitation number that were tested. This uniqueness is attributed partly to the fact that the range of the solution is known, so that a reasonable initial guess can be selected. Figure 5-4 shows that several different initial guesses, which are tabulated in Table 5.3, lead to the same solution.

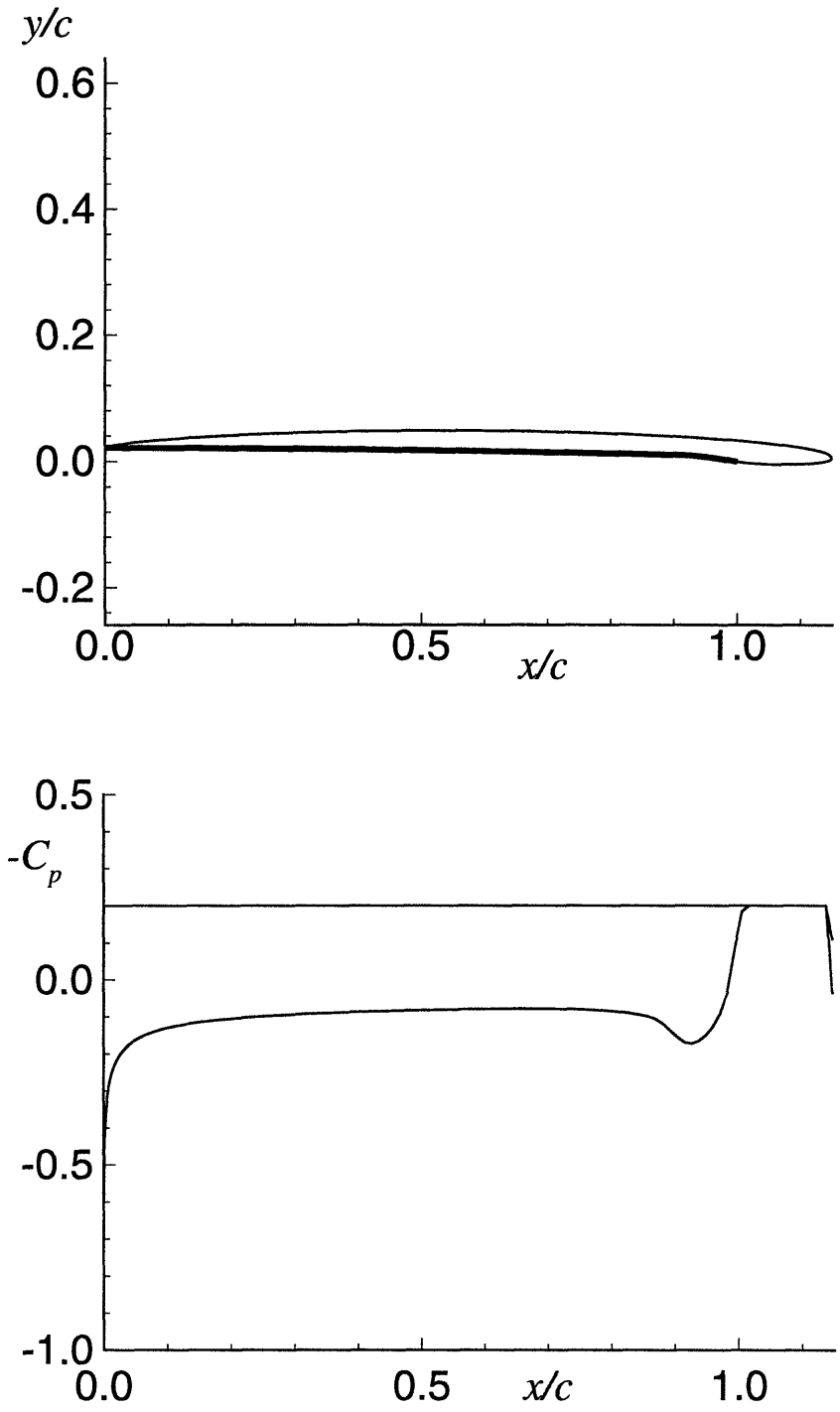

Figure 5-3: Optimum supercavitating foil geometry and corresponding pressure distribution : $C_{L_o} = 0.303$, $\sigma_o = 0.2$, $Re = 6.3 \times 10^6$

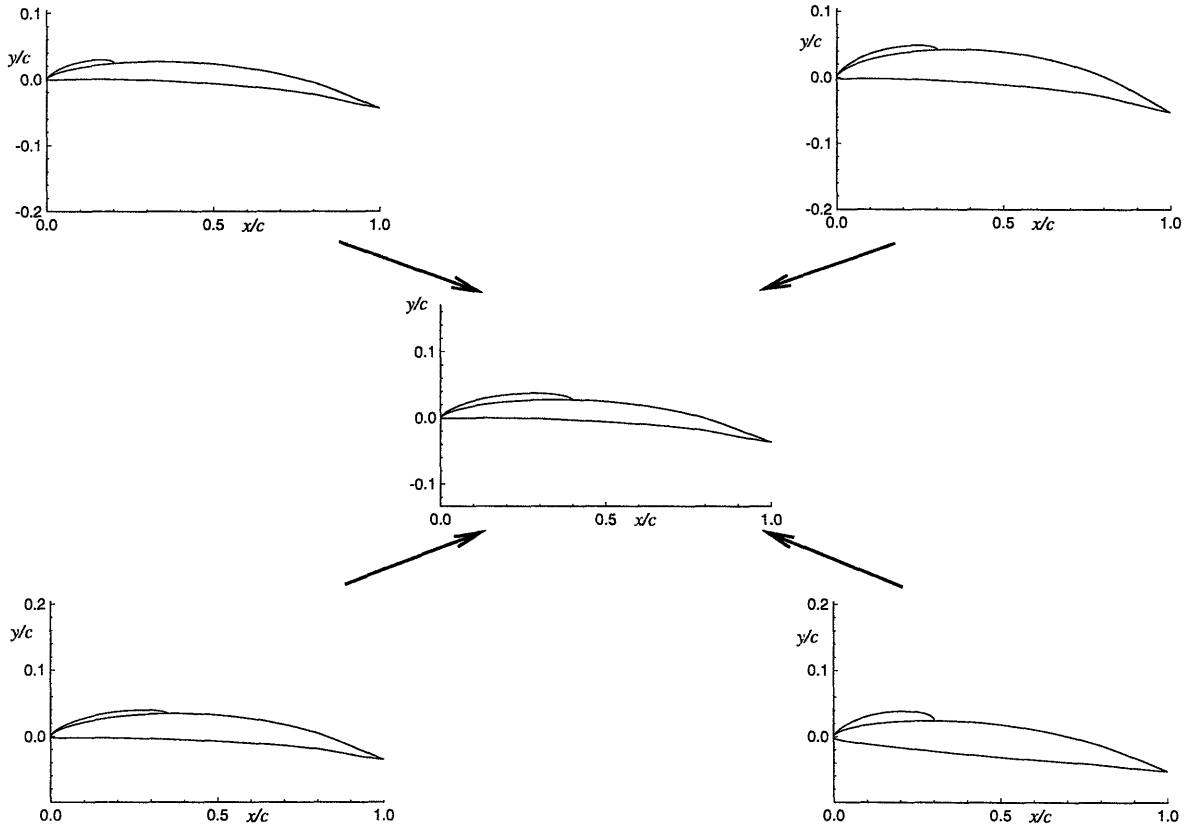

Figure 5-4: Different initial foil geometry guesses lead to the same optimum solution

5.4 Effect of the Algorithm Parameters on the Solution

There are several parameters used in the algorithm and the effect of the parameters on the solution is investigated in detail in this section. The parameters are re-stated below.

λ	:	perturbation of each design variable for the initial linear approximation of the functions (see also equation (4.1))
δ	:	maximum allowed change of design variables at each iteration
ε	:	tolerance for convergence

The effect of each parameter on the performance of the algorithm is demonstrated next. The default parameter values used in the hydrofoil design problems are:

$$\begin{aligned} \lambda &= 0.05\ (5\%) \text{ of the initial variable} \\ \delta &= 0.02 \\ \varepsilon &= 1 \times 10^{-3} \end{aligned}$$

The algorithm terminates when the root mean square of the change of the variables is less than ε.

$$\frac{\sqrt{\sum_{i=1}^{n} \left(\frac{x_i^{(k+1)} - x_i^{(k)}}{x_i^{(k+1)}} \right)^2}}{n} \leq \varepsilon$$

The two-dimensional hydrofoil design problem is suitable for a test of the performance of the algorithm, since the number of the design variables is relatively small and the computational effort is much less than the three-dimensional propeller design problem.

Figures 5-5 and 5-6 show the effect of α on the solution and the required number of iterations, equivalently the number of analysis runs, for the partially and supercavitating hydrofoil designs described in the previous sections, respectively. δ and ε are kept constant, equal to the default values in this test. In both design cases, α affects the number of iterations, but the solution is not sensitive to this parameter.

Figures 5-7 and 5-8 show the effect of δ on the required number of iterations and the solution for the same partially and supercavitating hydrofoil designs as in Figures 5-5 and 5-6, respectively. It is seen from these figures that the solution is again insensitive to δ, although there is a dependence of the number of iterations on δ. However, this seems to be problem dependent. Therefore it is difficult or not feasible to find the optimum δ that works for all the problems. Although it is needless to say that the required number of iterations is extremely important from the viewpoint of computational efficiency, the fact that the solution is unique regardless of the δ value is even more essential.

Finally, Figures 5-9 and 5-10 show the effect of ε on the solution. In the case of the supercavitating hydrofoil, complete convergence is realized for $\varepsilon \leq 1 \times 10^{-3}$. For ε larger than this value, C_D is slightly higher than the truly converged C_D. In the case of the partially cavitating hydrofoil, complete convergence is achieved for $\varepsilon \leq 1 \times 10^{-3}$. In the contrast to the supercavitating hydrofoil case, C_D is lower for a larger ε. This is because all the constraints are not strictly satisfied for a larger ε.

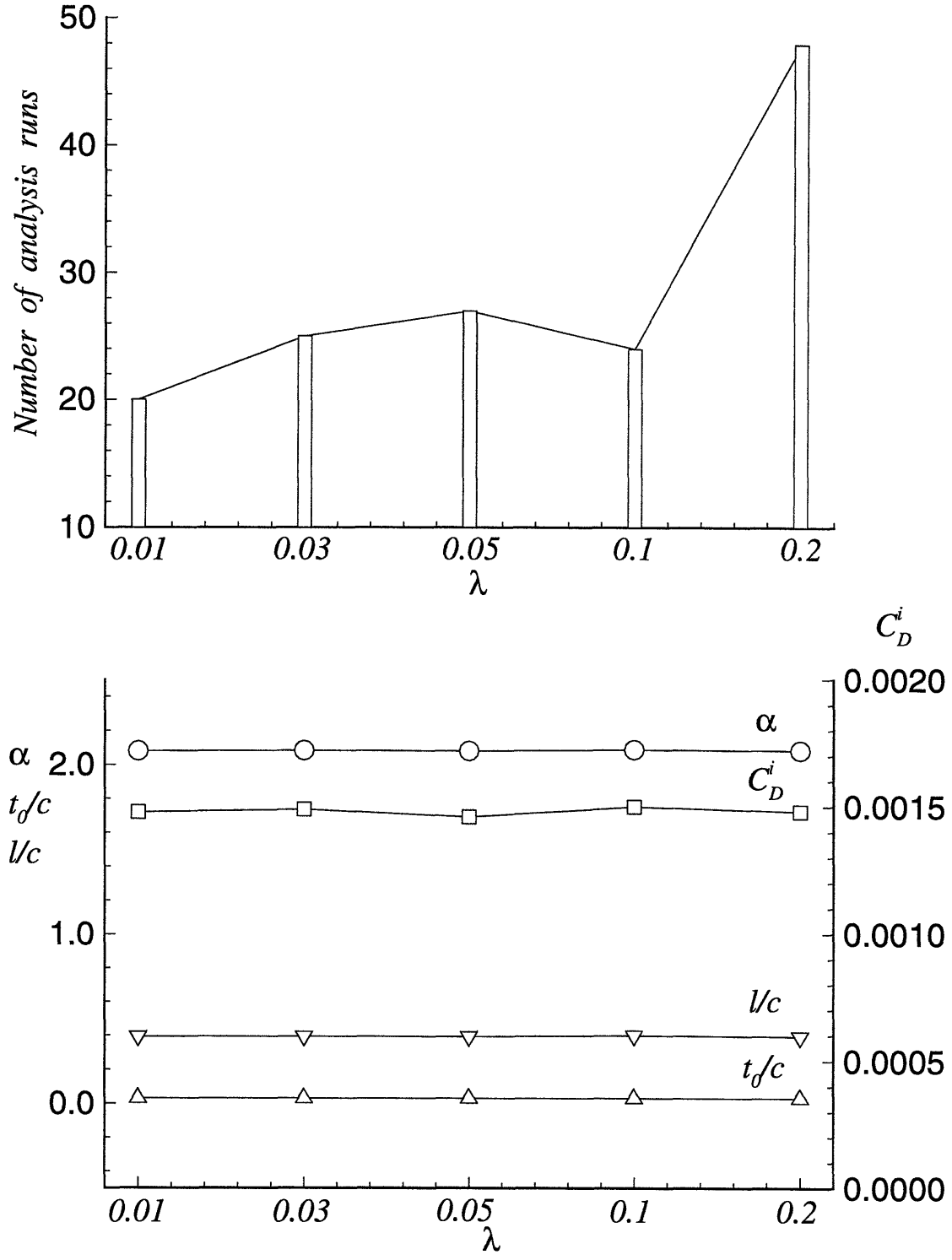

Figure 5-5: Effect of λ in the finite difference scheme for the initial linear approximation of the functions on the required number of analysis runs and the solution : $\delta = 0.02, \varepsilon = 1 \times 10^{-3}$: *Partially cavitating* hydrofoil

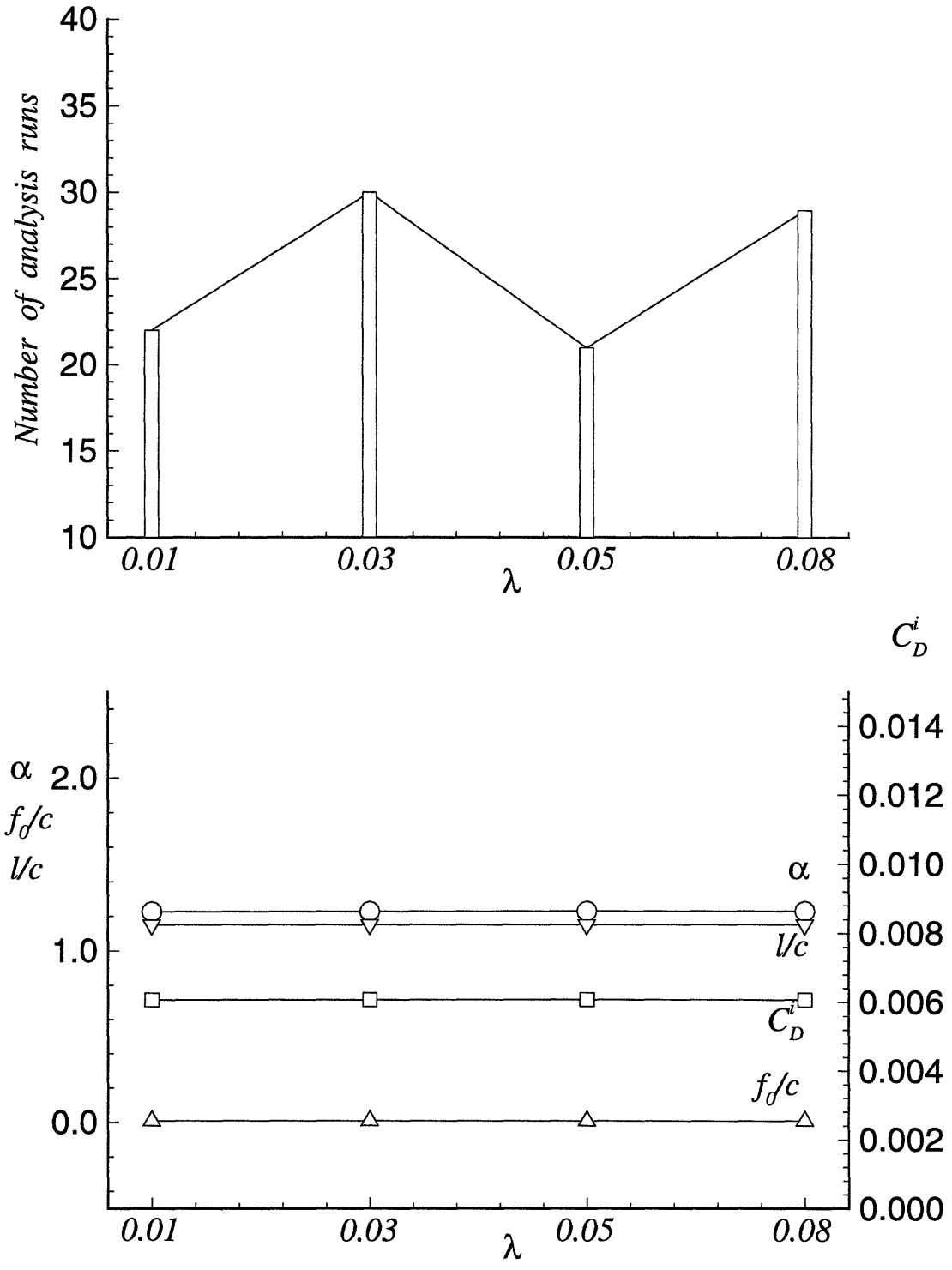

Figure 5-6: Effect of λ in the finite difference scheme for the initial linear approximation of the functions on the required number of analysis runs and the solution : $\delta = 0.02, \varepsilon = 1 \times 10^{-3}$: *Supercavitating* hydrofoil

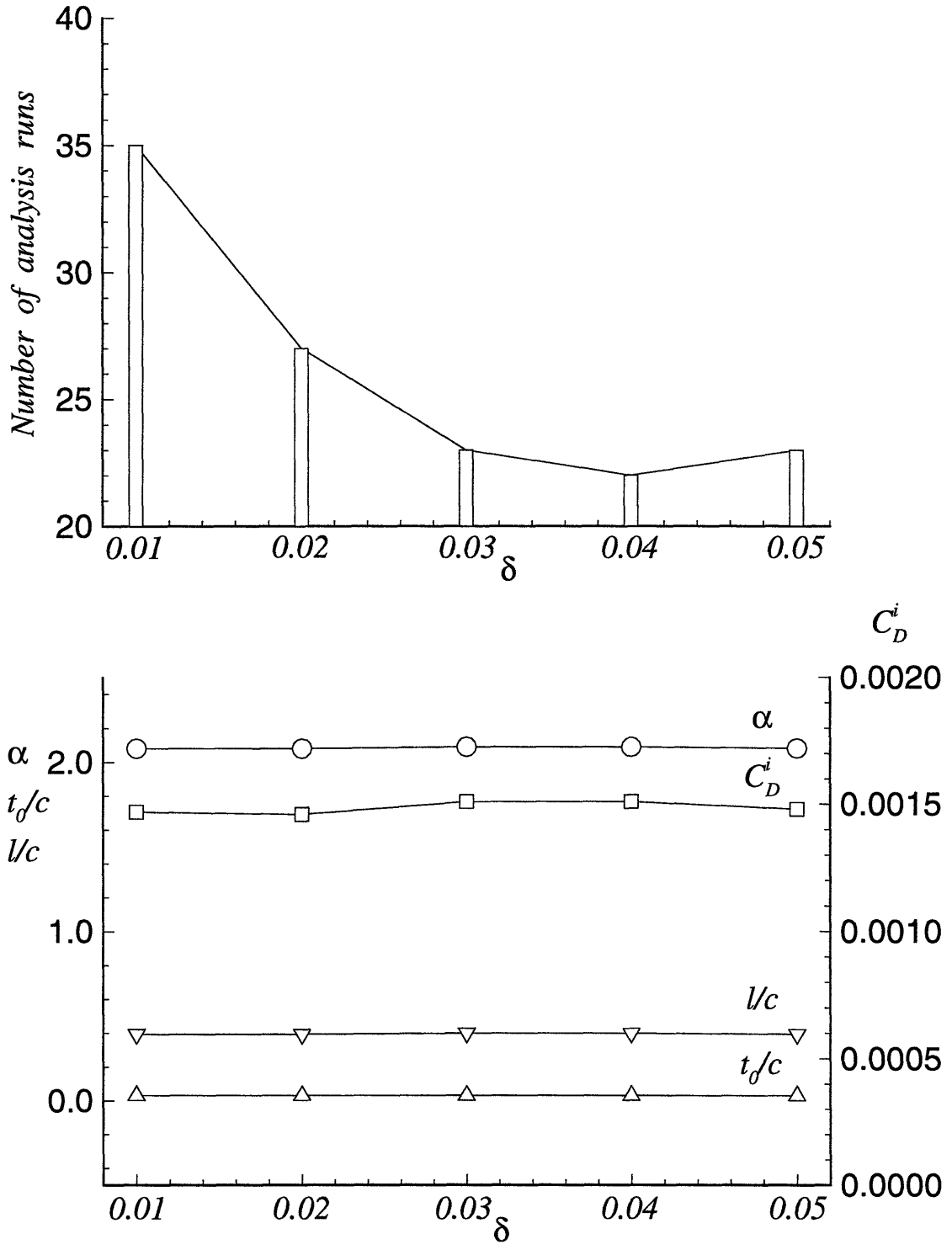

Figure 5-7: Effect of the maximum movement of the variables, δ, on the required number of analysis runs and the solution : $\lambda = 0.05, \varepsilon = 1 \times 10^{-3}$: *Partially cavitating* hydrofoil

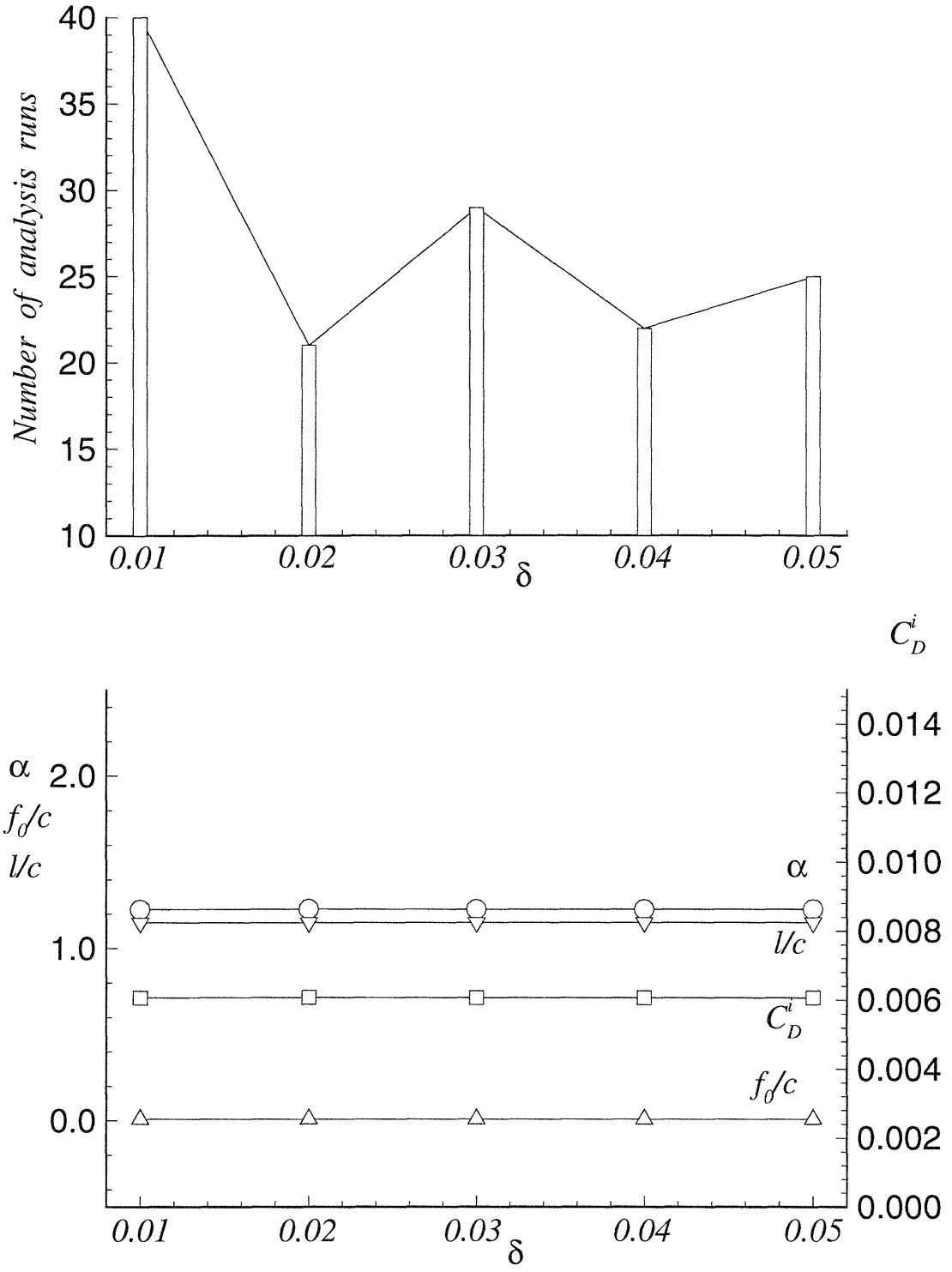

Figure 5-8: Effect of the maximum movement of the variables, δ, on the required number of analysis runs and the solution : $\lambda = 0.05, \varepsilon = 1 \times 10^{-3}$: *Supercavitating* hydrofoil

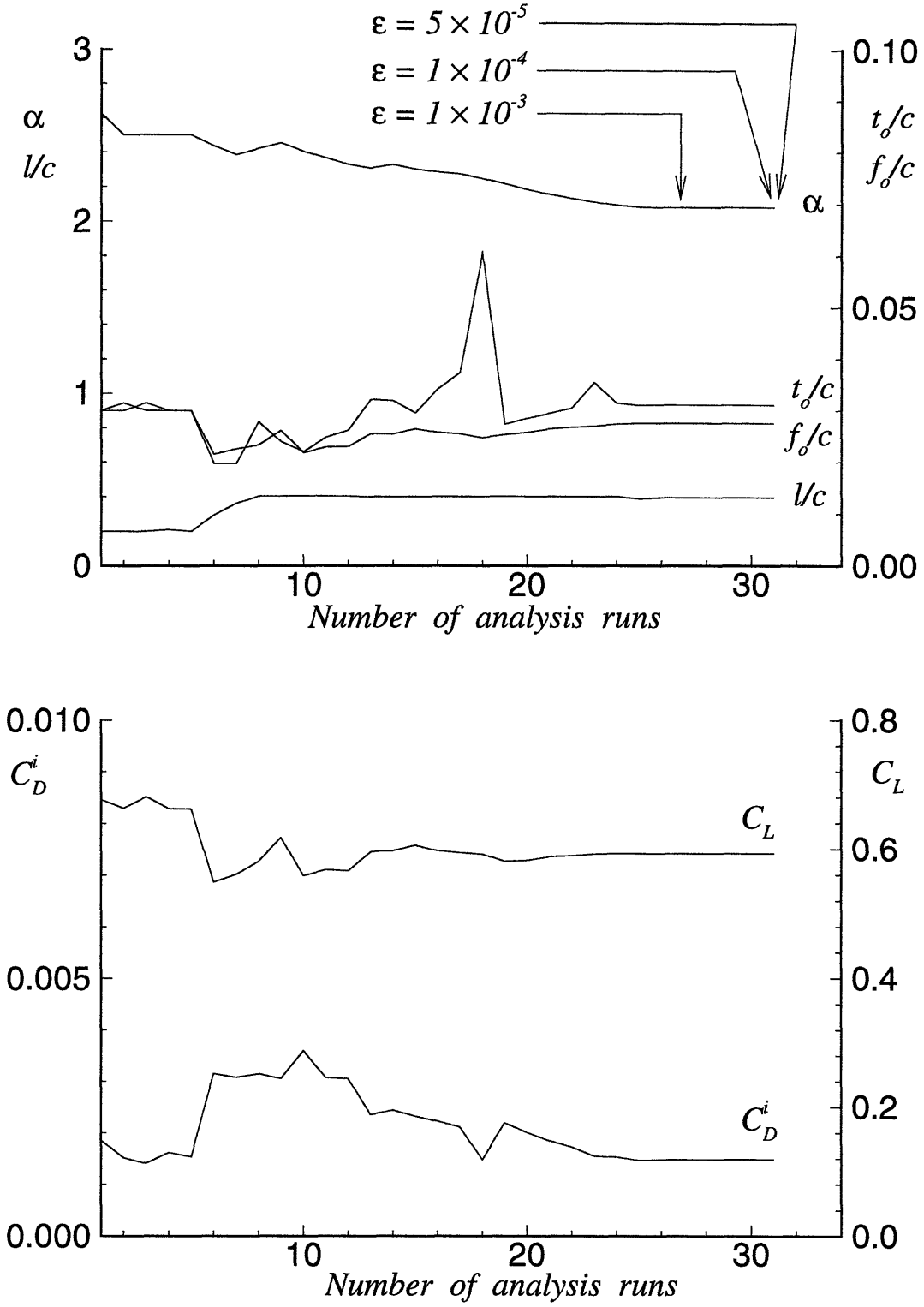

Figure 5-9: Effect of the tolerance for convergence, ε, on the required number of analysis runs and the solution : $\lambda = 0.05, \delta = 0.02$: *Partially cavitating* hydrofoil

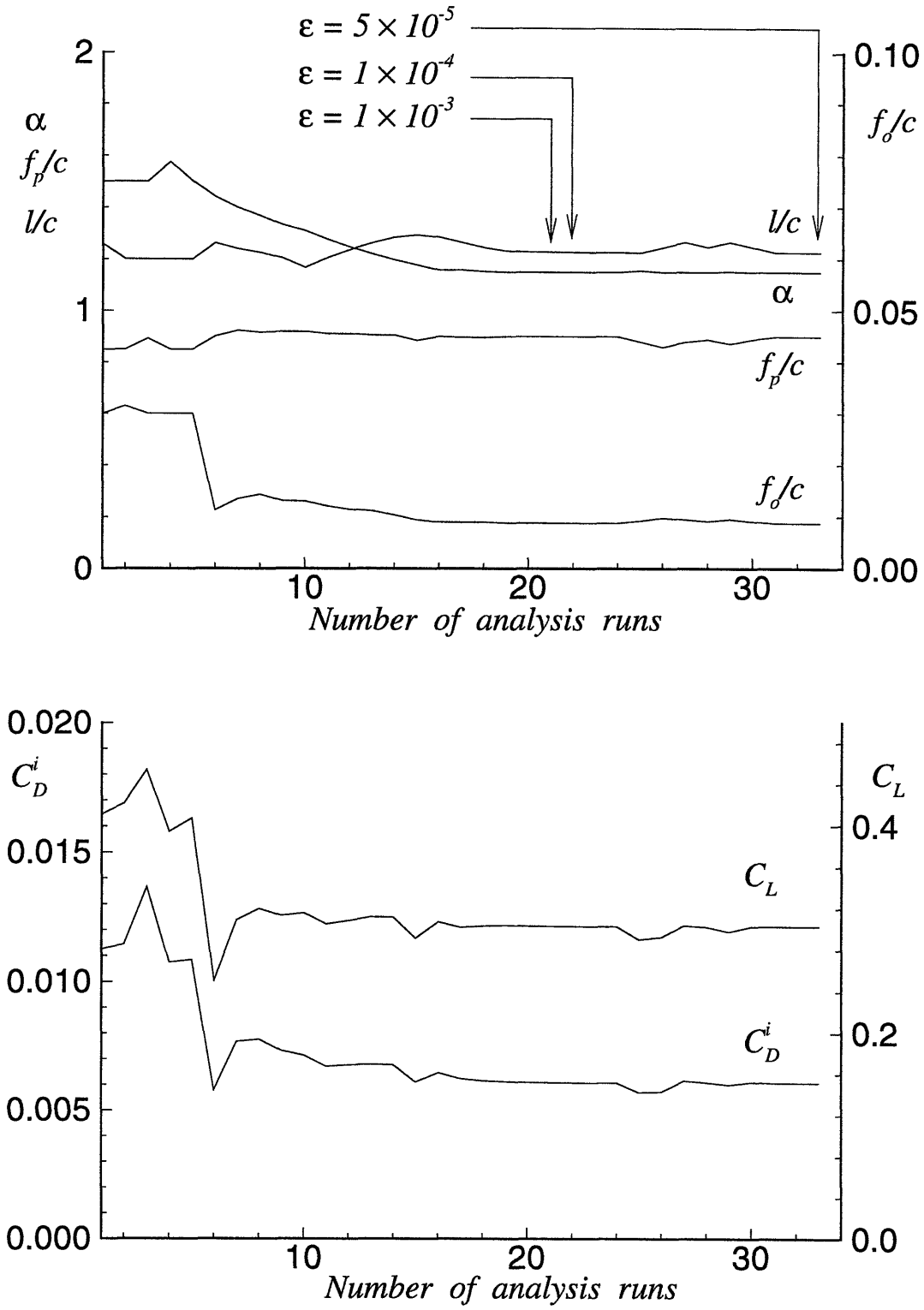

Figure 5-10: Effect of the tolerance for convergence, ε, on the required number of analysis runs and the solution : $\lambda = 0.05, \delta = 0.02$: *Supercavitating* hydrofoil

5.5 Effect of Viscosity

The effect of viscosity may be included more accurately, than via a uniform friction coefficient, by coupling the inviscid cavity panel method with the integral boundary layer solver of Drela [15], as was done recently by Kinnas et al [42]. The viscous flow effects have been found to alter the cavitation number and the lift coefficient, as well as the cavity detachment point. A numerically efficient way to include these effects, iteratively *outside* the optimization loop, has been developed by Kinnas and Mishima [41] and Kinnas et al [43].

Step 1: Determine *inviscid* optimum foil geometry for given C_{L_o} and σ_o.

Step 2: Apply viscous/inviscid interactive cavity analysis method for the optimum foil geometry. Determine modified lift coefficient, C_{L_v}, and modified cavitation number, σ_v, due to viscous effects.

Step 3: Determine optimum foil geometry for given C'_{L_o} and σ'_o where:

$$C'_{L_o} = C_{L_o} - (C_{L_v} - C_{L_o}) \tag{5.10}$$

$$\sigma'_o = \sigma_o - (\sigma_v - \sigma_o) \tag{5.11}$$

Step 4: Iterate Steps 2-3 until $C_{L_v} = C_{L_o}$ and $\sigma_v = \sigma_o$.

The optimum *inviscid* and *viscous* geometries and the corresponding pressure distribution on the foils are shown in Figures 5-11 and 5-12, respectively. The iterative procedure between the inviscid optimization and the viscous analysis converged after three iterations in this case.

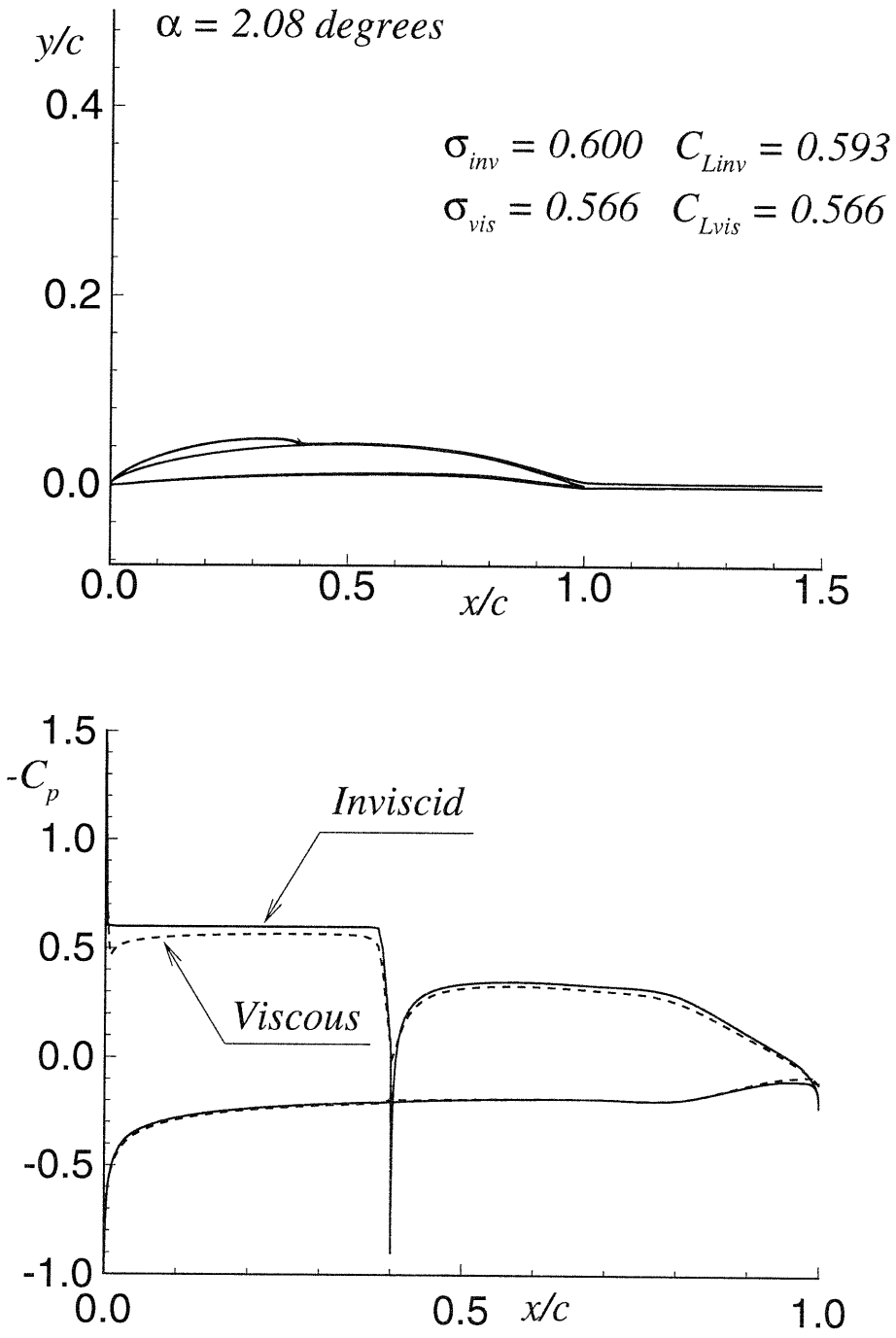

Figure 5-11: *Inviscid* optimum partially cavitating foil geometry and corresponding pressure distribution ($Re = 5.6 \times 10^6$)

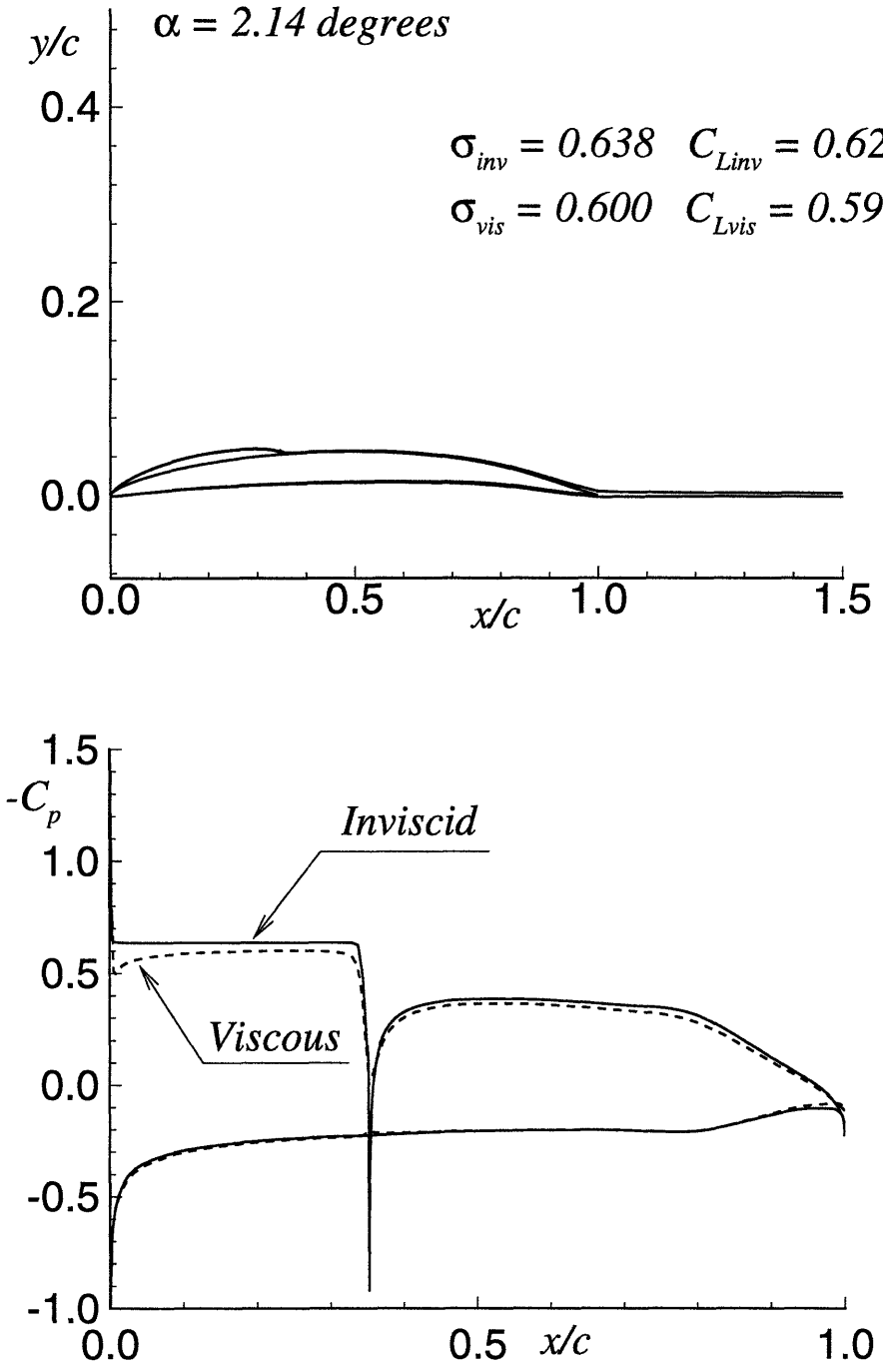

Figure 5-12: *Viscous* optimum partially cavitating foil geometry and corresponding pressure distribution ($Re = 5.6 \times 10^6$)

Chapter 6

Design of Cavitating Propeller Blades

The design of three dimensional propeller blades by the present method is described in this chapter. First, the design of a propeller in uniform flow is performed. This geometry turned out to be a non-cavitating propeller for the given conditions. The radial circulation distribution corresponding to this design is compared to the optimum circulation based on lifting line theory [10]. The blade geometry and the pressure distribution on the blade are compared with the design from a lifting-line/lifting-surface approach [25].

Then, cavitating propeller blades in non-uniform flow are designed for several design requirements. The convergence of the algorithm and the effect of the constraints on the solution are investigated.

6.1 Statement of the Problem

The objective of the cavitating propeller design is to find a blade mean camber surface, represented by a B-spline polygon net, which requires minimum torque for a given design requirement.

Given :

- Effective wake

- Thrust coefficient

$$K_T = \frac{T}{\rho n^2 D^4}$$

- Advance coefficient

$$J_s = \frac{V_s}{nD}$$

- Cavitation number

$$\sigma_n = \frac{p_{shaft} - p_v}{\frac{1}{2}\rho n^2 D^2}$$

- Froude number

$$F_n = \frac{n^2 D}{g}$$

- Number of blades, Z
- Thickness distribution
- Rake distribution
- *Constraints on cavity characteristics and/or unsteady forces*

where

T : propeller thrust

V_s : ship speed

n : propeller rotational speed

D : propeller diameter

p_{shaft} : pressure at the propeller shaft depth far upstream

p_v : vapor pressure

ρ : fluid density

g : acceleration of gravity

Determine :

- Blade mean camber surface by a B-spline polygon net that requires minimum torque coefficient,

$$K_Q = \frac{Q}{\rho n^2 D^5}$$

where,

Q : propeller torque

In non-axisymmetric inflow, the given thrust is the circumferential mean value of a time-varying thrust, and the torque to be minimized is the circumferential mean value of a time-varying torque. In a non-dimensional form,

$$\bar{K}_T = \frac{1}{2\pi}\int_0^{2\pi} K_T(\theta)d\theta \tag{6.1}$$

$$\bar{K}_Q = \frac{1}{2\pi}\int_0^{2\pi} K_Q(\theta)d\theta \tag{6.2}$$

Figure 6-1 illustrates unsteady forces of a four-bladed propeller in a non-axisymmetric inflow.

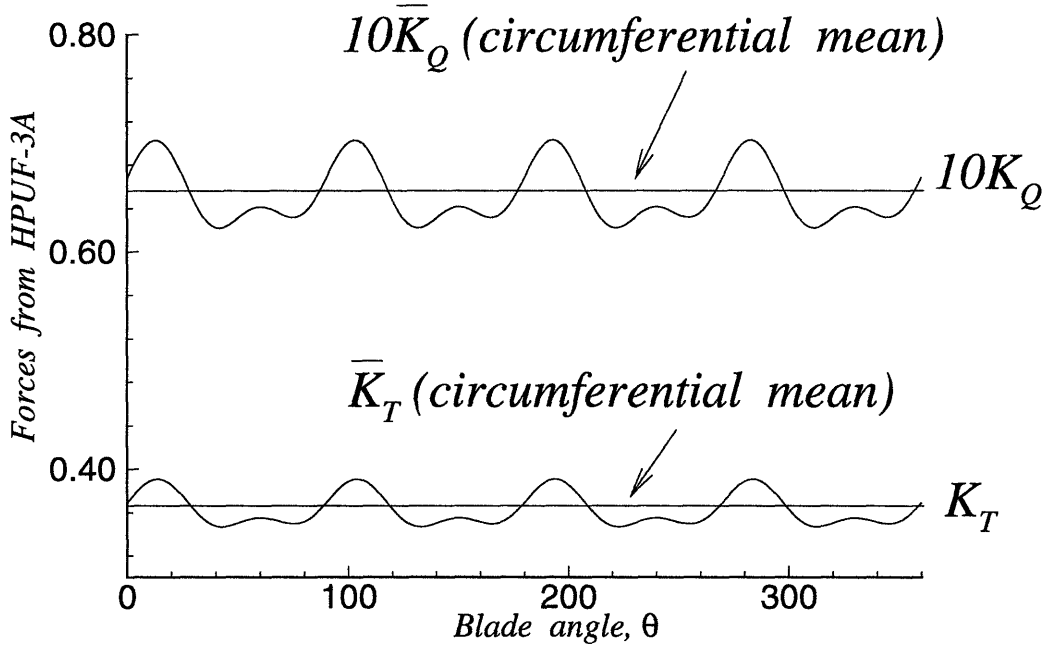

Figure 6-1: Circumferential mean thrust and torque of a four-bladed propeller in a non-axisymmetric inflow

6.2 Propeller in Uniform Flow

6.2.1 Design Condition

The design condition is

$$\begin{aligned} J_s &= 1.0 \\ \sigma_n &= 5.0 \\ K_T &= 0.15 \end{aligned} \tag{6.3}$$

The number of blades, $Z = 3$, is chosen. The hub/diameter ratio is 0.2. The inflow is uniform. Pressure variation due to the hydrostatic effect is turned off in *HPUF-3A*, thus, the Froude number, F_n, does not affect the solution. The radial thickness and rake distributions are given. Skew optimization is not included in this design. The propeller designed for these conditions turns out to be a non-cavitating propeller. The chord length is also given to allow the direct comparison to the design using a lifting-line/lifting-surface approach. B-spline vertices are allowed to move only in the direction normal to the original chordwise segments in the yz plane, not to stretch in the chordwise direction. Four chordwise ($N_u = 4$) by four spanwise ($N_w = 4$) B-spline vertices are used.

6.2.2 Results

The radial circulation distributions from *CAVOPT-3D* and from a vortex-lattice lifting line design program, *PLL* [11], are shown in Figure 6-2. The frictional drag coefficient, $C_f = 0.004$ was used. The convergence history of K_T, K_Q, and the cavity area is shown in Figure 6-3. Although the initial blade is cavitating, it turns out that the optimum design for this relatively high cavitation number is a non-cavitating propeller. The blade geometries from *CAVOPT-3D*, together with the 4×4 B-spline vertices, are shown in Figure 6-4.

For the same chord length distribution as in *CAVOPT-3D*, *PLL* was run to get the optimum radial circulation distribution. Then, the circulation obtained from *CAVOPT-3D* was used in the lifting line calculation to evaluate the forces, which are tabulated in Figure 6-2. Circulation distributions from the two methods are reasonably close to each other. The fact that the two slightly different circulation distributions give almost the same efficiency implies that the design surface is fairly flat near the optimum solution.

However, this is not necessarily the best design because this propeller blade was not designed to have shock free entry. If a fully wetted propeller was to be designed, a fully wetted design method should be used. A lifting surface non-cavitating blade design method developed by Kerwin [25], which is designated as *PBD-10*, was used to design a blade for the comparison to the design by the present method. *PBD-10* requires a radial and chordwise circulation distribution as an input and iteratively determines the blade geometry, which satisfies the flow tangency condition on the blade mean camber surface. The optimum radial circulation distribution determined by *PLL* was used. The NACA a=0.8 loading [1] was used as the chordwise vorticity distribution at all radii. The pressure distributions on the optimum blade designed by *CAVOPT-3D* and *PBD-10* are shown in Figure 6-5. It is seen from this figure that for both designs the blade sections are at ideal angles of attack (shock-free entry) at all radii as required by *PBD-10*. Although the shock free entry condition was *not* imposed by *CAVOPT-3D* in this design, the singular behavior at the leading edge, which could have increased the drag, was avoided. Figure 6-6 shows the blade geometries designed by *CAVOPT-3D* and *PBD-10*. The *CAVOPT-3D* geometry is the same as in Figure 6-4. Since the chordwise loadings are not the same, as shown in Figure 6-5, the required pitch distributions to give (almost) the same radial circulation distribution are slightly different in the *CAVOPT-3D* and *PBD-10* designs. The geometry resulting from *PBD-10* exhibits a discontinuity near the tip. This is typical in this version of *PBD* due to its blade geometry representation. *PBD-10* determines the locations of discrete control points and splines them to give the entire blade geometry. *CAVOPT-3D* used a cubic B-spline representation that guarantees

the smoothness of the blade geometry in curvature as well as in slope.

It took approximately one hour for this design to be determined by *CAVOPT-3D* on an ALPHA/DEC 600(5/266) workstation.

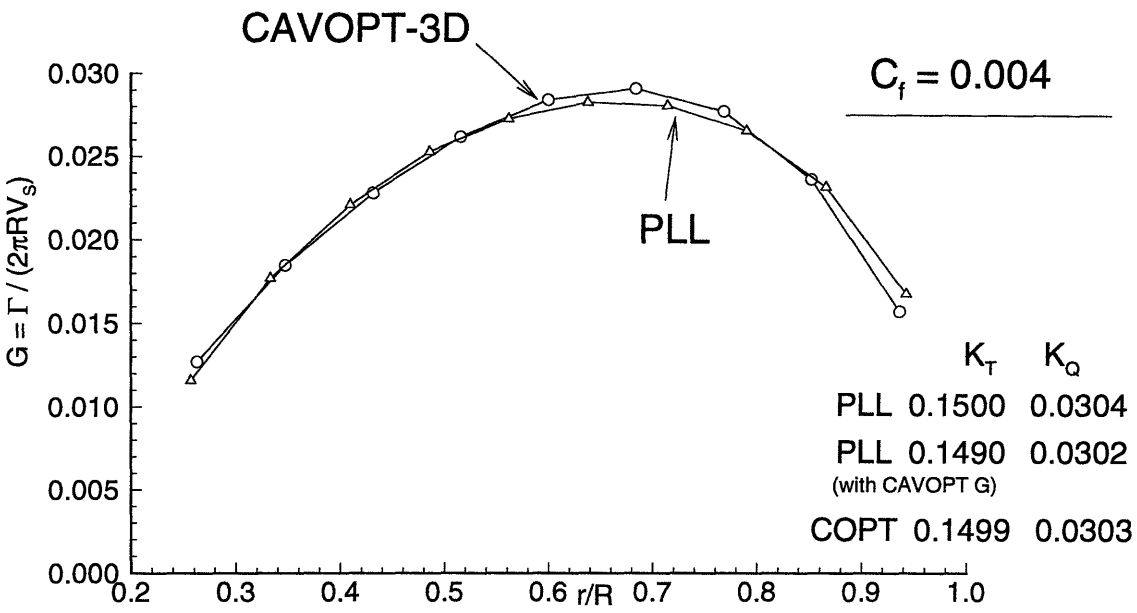

Figure 6-2: Optimum circulation distribution obtained from *CAVOPT-3D* and *PLL* : $C_f = 0.004$

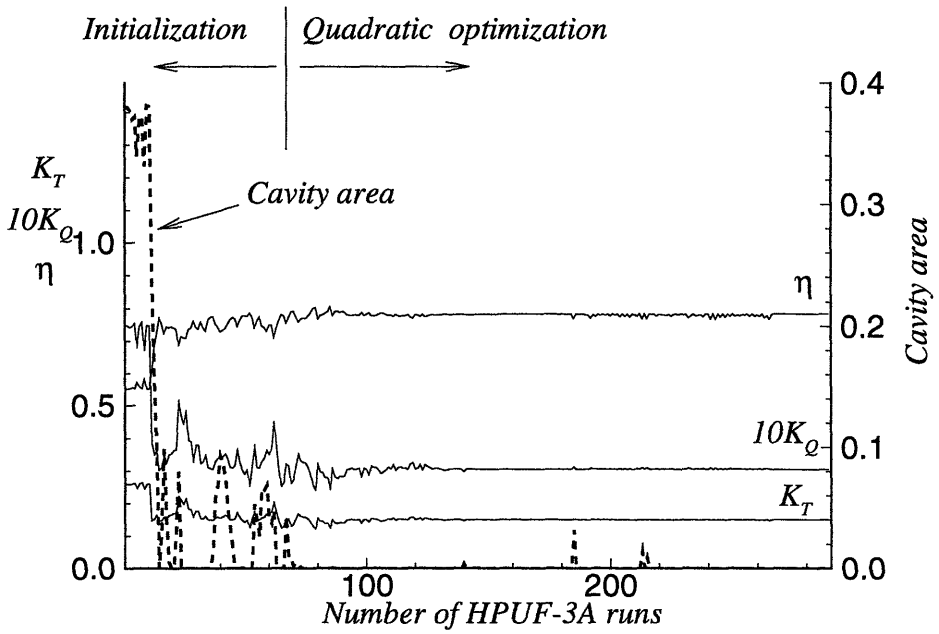

Figure 6-3: Convergence history of forces and cavity area in *CAVOPT-3D*: $C_f = 0.004$

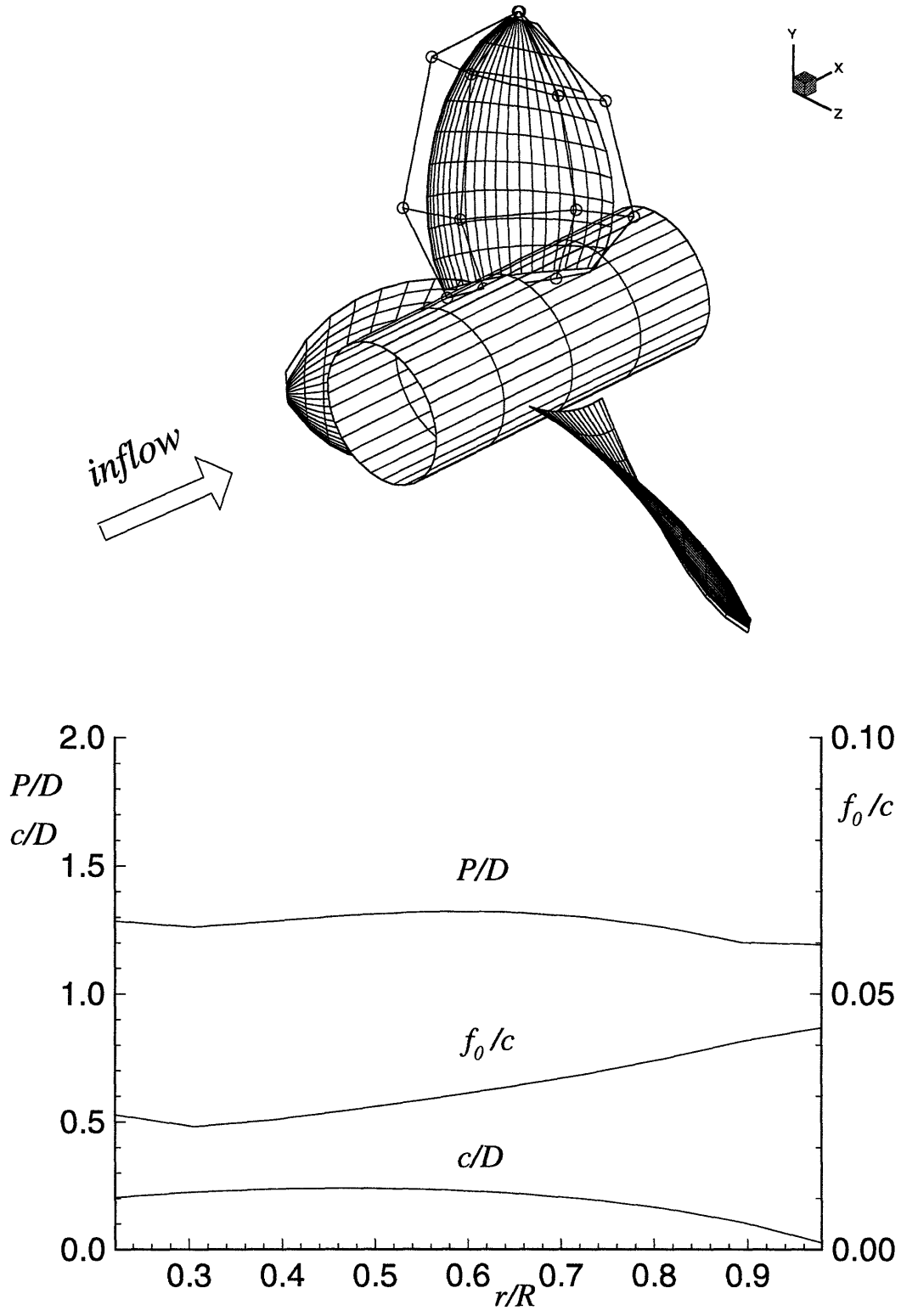

Figure 6-4: Optimum blade geometry by *CAVOPT-3D* : $C_f = 0.004$

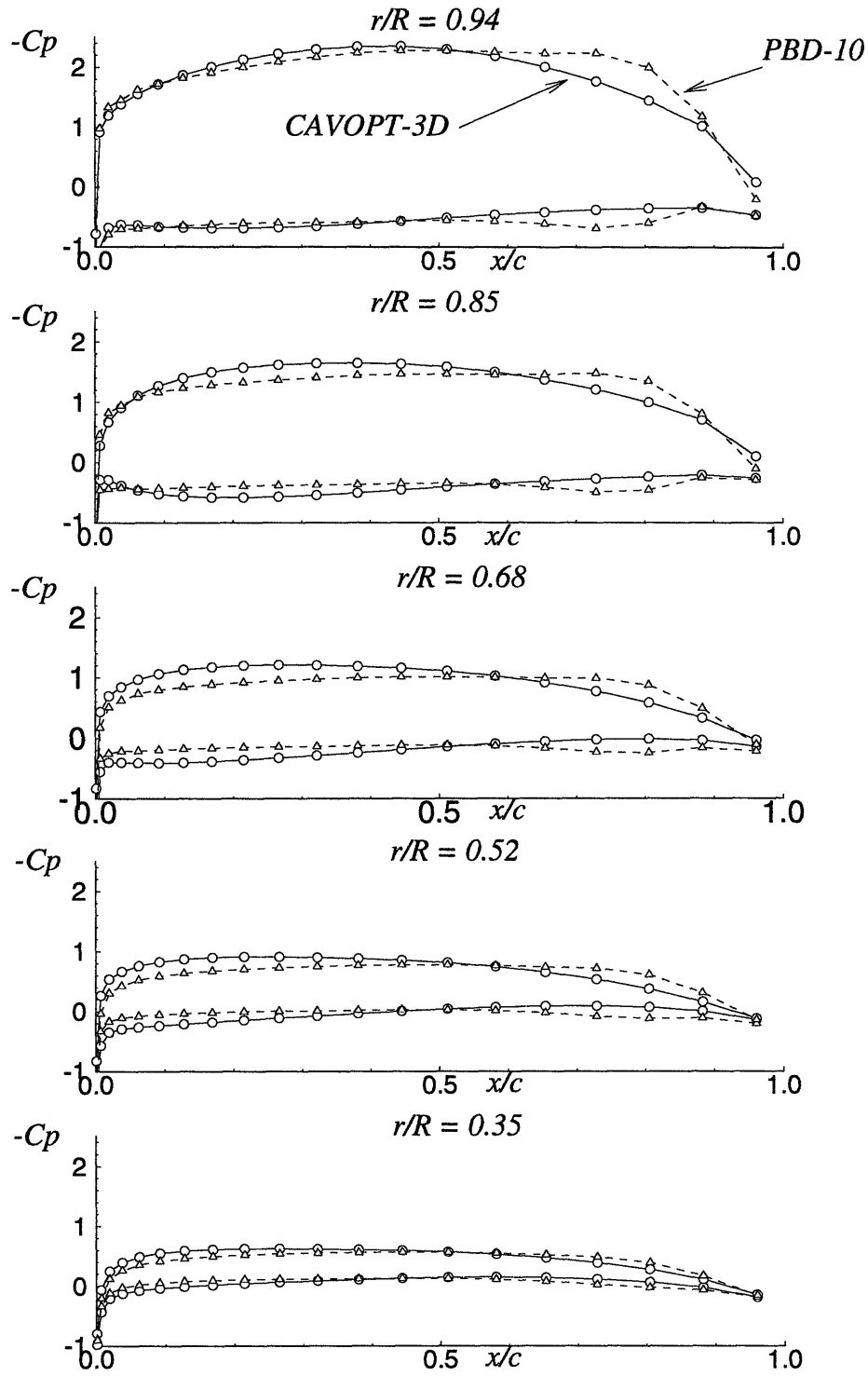

Figure 6-5: Pressure distribution on the optimum blade designed by *CAVOPT-3D* and *PBD-10* : $C_f = 0.004$

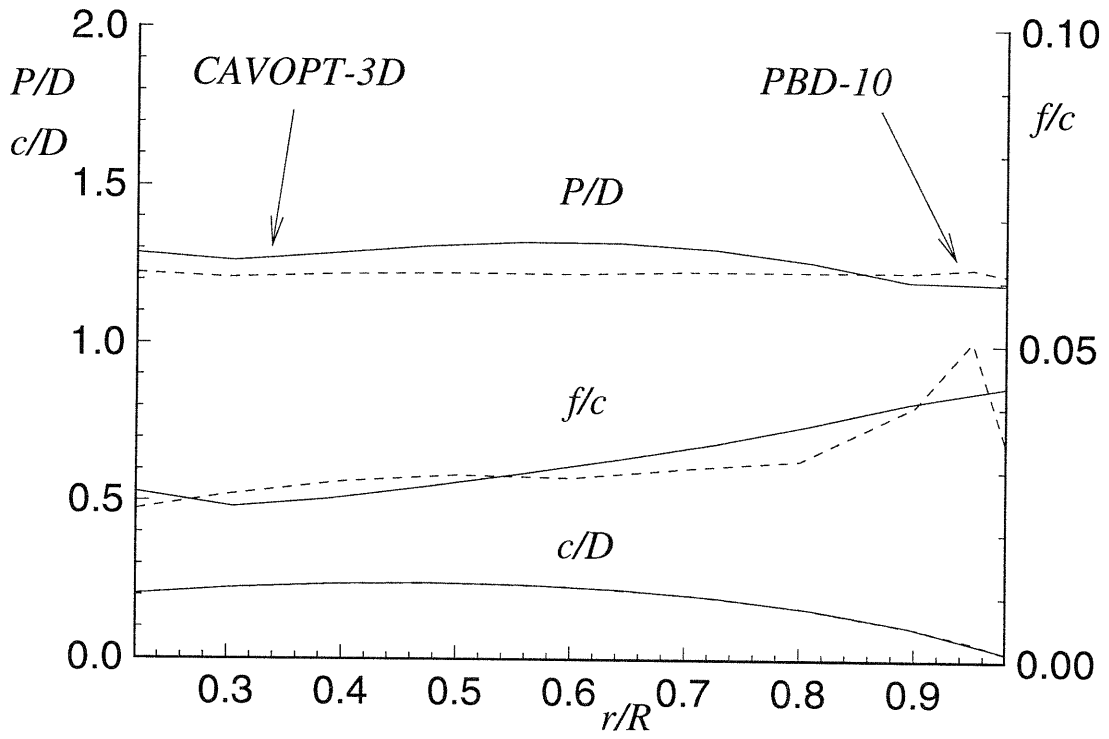

Figure 6-6: Optimum blade geometries designed by *CAVOPT-3D* and *PBD-10*: $C_f = 0.004$

6.3 Cavitating Propeller in Non-Uniform Flow

6.3.1 Design Condition

The design of cavitating propellers in non-uniform flow with cavity constraints is considered in this section. The design condition is

$$\begin{aligned} J_s &= 1.2 \\ \sigma_n &= 2.5 \\ F_n &= 5.0 \\ \bar{K}_T &= 0.2 \\ SK &\leq SKMAX \\ CA &\leq CAMAX \\ VV &\leq VVMAX \\ FA &\leq FAMAX \end{aligned} \tag{6.4}$$

where

SK	: Skew at the tip
CA	: Maximum back cavity area / Blade area
FA	: Maximum face cavity area / Blade area
VV	: Blade rate cavity volume velocity harmonics / nR^3
$SKMAX$	: Allowable maximum skew at the tip
$CAMAX$	: Allowable maximum back cavity area / Blade area
$CAMAX$	: Allowable maximum face cavity area / Blade area
$VVMAX$	: Allowable maximum blade rate cavity volume velocity harmonics / nR^3

As discussed in section 6.1, the present method minimizes the circumferential mean torque, $\bar{K}_Q$, in non-axisymmetric inflow for a given circumferential mean thrust,

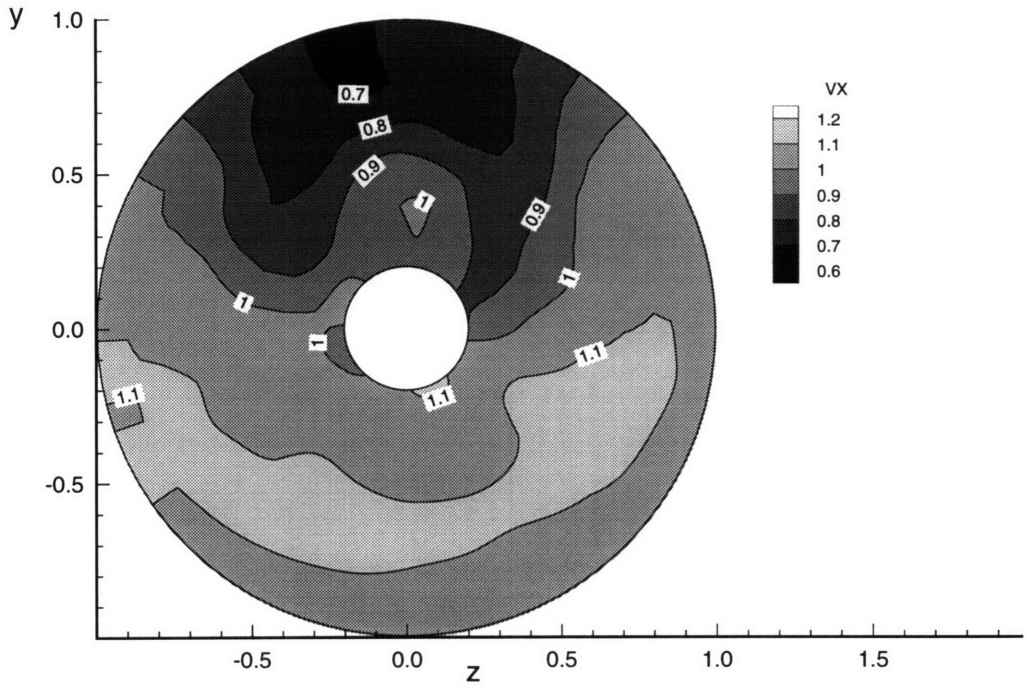

Figure 6-7: Non-uniform inflow used in the sample runs : axial velocity / V_s

$\bar{K}_T$. This is different from other design methods, which evaluate the optimum propeller geometry subject to circumferential mean axisymmetric inflow. For non-cavitating propellers, the two approaches will give the same steady forces in linear theory, in which the response to sinusoidal gusts with different frequencies is the sum of the individual responses to each frequency. However, for cavitating propellers, the two approaches will be different due to the nonlinear effect of the cavity.

Three-bladed propeller is chosen in this design again. The radial thickness and rake distributions are given. The thickness is usually given from the structural consideration. The rake is determined from the structural requirement and the geometrical arrangement of the ship hull and the propulsor. The chord length is determined by the method. Linear skew is used, where skew is 0 at the hub and maximum at the tip.

The inflow is spatially nonuniform and has only the axial component. The inflow velocity field is shown in Figure 6-7.

6.3.2 Cavity Constraints

In this section, several cavity constraints are investigated. In non-uniform inflow, cavity changes its shape during a propeller rotation. The maximum cavity planform area on the suction side of the blade (also called *back* cavity), non-dimensionalized on the blade area, is restricted to be less than some specified value, $CAMAX$. The blade geometry including the blade area is determined with this constraint by the optimization procedure, which minimizes the required torque. The blade area has usually been determined using an empirical chart and a non-cavitating blade design method is used to determine the blade geometry. Then an analysis method is used to check the cavitation performance.

The non-dimensional maximum cavity planform area on the pressure side (also known as *face* cavity) must be less than some specified value, $FAMAX$, which is almost zero in most cases.

One of the main objectives of the present design concerns the unsteady performance of the propeller. The pressure fluctuations induced by the intermittent cavity on a ship's hull, as well as the vibratory forces acting on the propeller shaft, must be considered. The blade rate harmonics of cavity volume velocity is a direct measure of the free-space pressure fluctuations at large distances from the propeller as shown in [6, 34]. In the program, $VVMAX$ is the maximum allowable blade rate harmonics of cavity volume velocity non-dimensionalized on nR^3.

Skew is introduced to improve the unsteady performance of the propeller. Table 6.1 summarizes the imposed constraints and the resulting propeller characteristics. $N_u = 4$ (chordwise) and $N_w = 4$ (spanwise) B-spline vertices are used for the designs presented in this section. Initial B-spline vertices are arbitrary, although of course a reasonable guess will help a faster convergence towards the optimum solution. The same initial geometry with $\Phi = 1.55$ (defined by equation (4.8)) is used for all the runs in this section.

	Constraints				Results				
	SKMAX	*CAMAX*	*VVMAX*	*FAMAX*	*SK*	*CA*	*VV*	*FA*	η
1	0	-	-	-	0	0.617	0.0149	0.002	0.780
2	45	-	-	-	45	0.652	0.0178	0.002	0.792
3	45	0.3	-	-	45	0.300	0.0110	0.002	0.790
4	45	0.3	0.007	-	45	0.300	0.0070	0.012	0.787
5	45	0.3	0.007	0	45	0.261	0.0070	0	0.776

Table 6.1: Cavity constraints and resulting values

Design No. 1

Figure 6-8 shows the blade geometry and cavity shapes designed without any constraints, which corresponds to the design No. 1 in Table 6.1. Skew is not included in this design. The convergence history of this run is shown in Figure 6-9. Without constraints, the non-dimensional maximum cavity planform area was 0.617.

Design No. 2

Figures 6-10 and 6-11 show the optimum blade and cavity shapes, respectively for design No. 2. There is no cavity constraint imposed. Linear skew is included. With skew, the efficiency increased from 0.780 to 0.792. However, the maximum cavity area, *CA* increased to 0.652.

Design No. 3

In the next design, the objective is to minimize the required torque with for given maximum cavity area allowed. Linear skew is allowed in this design. This run (design No. 3 in Table 6.1) is intended to show the effectiveness of skew to improve the unsteady performance. The optimum blade geometry and convergence history are shown in Figures 6-12 and 6-13, respectively. With skew, the efficiency is 0.790, which is only slightly lower than that for design No. 2 and higher than that for design No. 1. The blade rate harmonics of cavity volume velocity, which is not constrained, goes down as a by-product.

Design No. 4

In the next design (design No. 4 in Table 6.1), the constraint on the cavity volume velocity harmonics is imposed. The results are shown in Figures 6-14 and 6-15. Substantial reduction in cavity volume velocity harmonics is achieved with a small decrease in efficiency. Figure 6-17 shows the iteration history of the cavity geometry. The blade is at 42^o from the top.

Up to this point, there is no constraint on face cavitation. It is likely in the course of optimization that major face cavitation is avoided, since such cavitation would tend to exhibit a poor performance. In fact, designs No. 1-3 have almost zero face cavitation. However, there is a case where the blade has a small amount of face cavitation. The design No. 4 is one of those few cases. It is possible to impose a constraint which eliminates face cavitation completely.

Design No. 5

Figures 6-16 shows the cavity geometries of the face cavitation free design (design No. 5 in Table 6.1). The face cavity constraint is turned on after $3N$ iterations. In other words, in the earlier iterations, face cavitation is allowed to exist simply to obtain a functional relationship between the face cavity area and the design variables. Otherwise, the function would not be defined well, since the most blade geometries would give zero face cavity area.

Figure 6-18 shows the blade geometries for designs No. 1-5 in terms of the radial distributions of pitch, camber, and chord length.

6.3.3 Effect of Initial Blade Geometry

In order to investigate the effect of the initial blade geometry on the solution, three different initial B-spline polygon nets were used. The parameter values $\Phi = 1.2$, 1.55 and 1.8 (defined by equation (4.8) in section 4.2) are used.
In these runs,

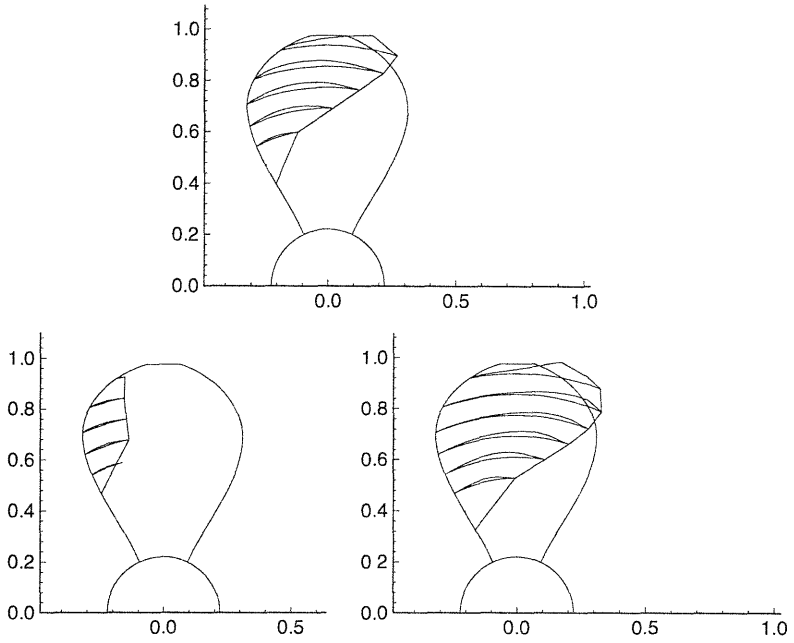

Figure 6-8: Cavity shapes for design No. 1, Blade angle $\theta = 318^o, 0^o, 42^o$ from left to right : $SKMAX = 0^o$, $CAMAX = \infty$, $VVMAX = \infty$, $FAMAX = \infty$

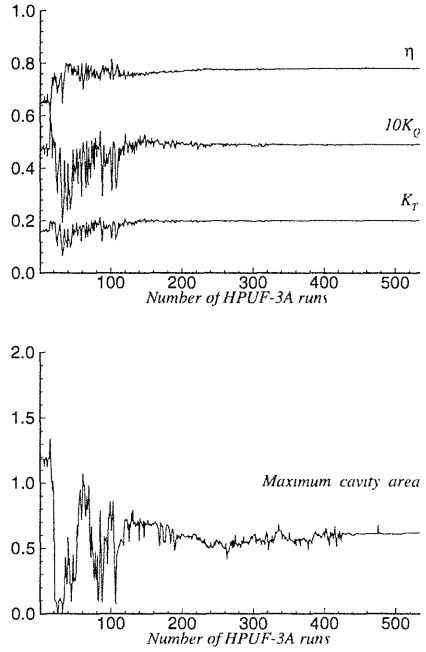

Figure 6-9: Convergence history of design No. 1 : $SKMAX = 0^o$, $CAMAX = \infty$, $VVMAX = \infty$, $FAMAX = \infty$

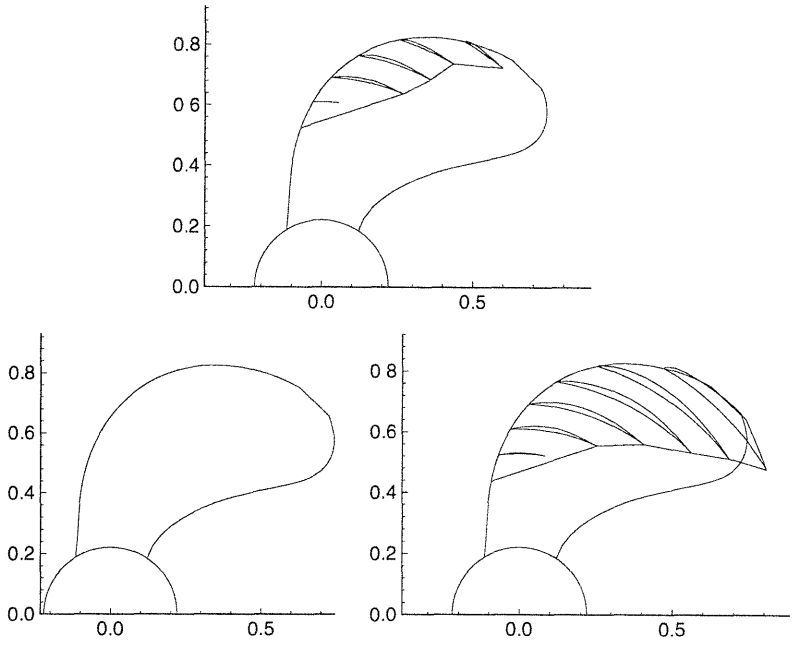

Figure 6-10: Cavity shapes for design No. 2 , Blade angle $\theta = 318^o, 0^o, 42^o$ from left to right : $SKMAX = 45^o$, $CAMAX = \infty$, $VVMAX = \infty$, $FAMAX = \infty$

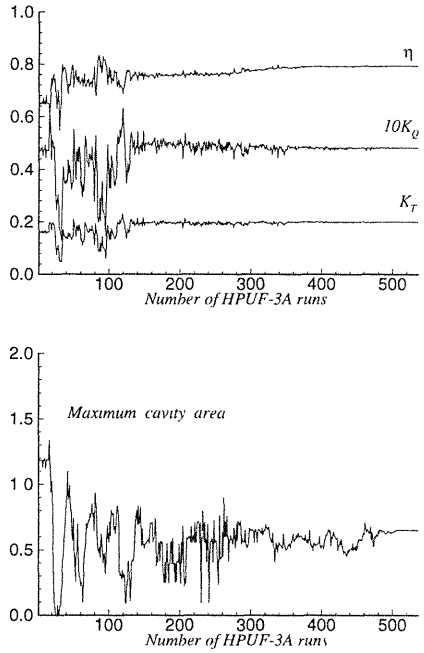

Figure 6-11: Convergence history of design No. 2 : $SKMAX = 45^o$, $CAMAX = \infty$, $VVMAX = \infty$, $FAMAX = \infty$

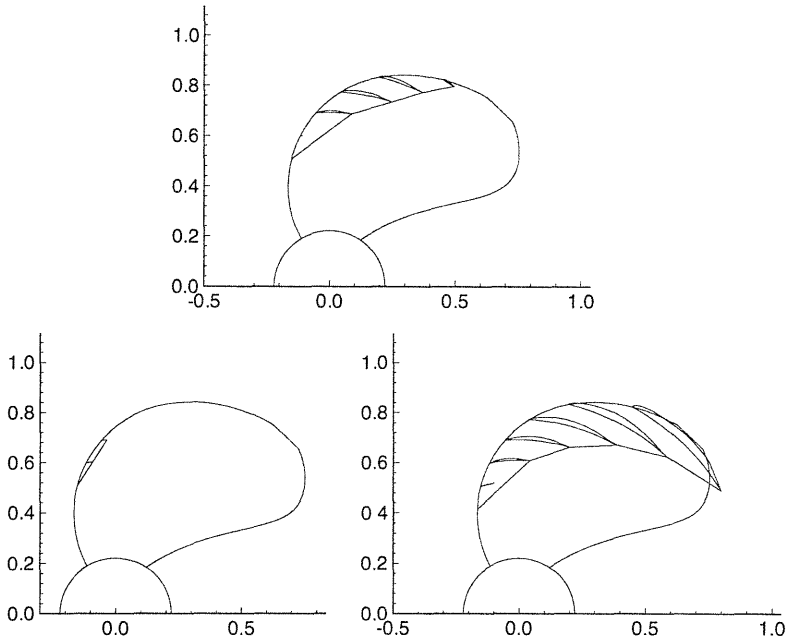

Figure 6-12: Cavity shapes for design No. 3 , Blade angle $\theta = 318^o, 0^o, 42^o$ from left to right : $SKMAX = 45^o$, $CAMAX = 0.3$, $VVMAX = \infty$, $FAMAX = \infty$

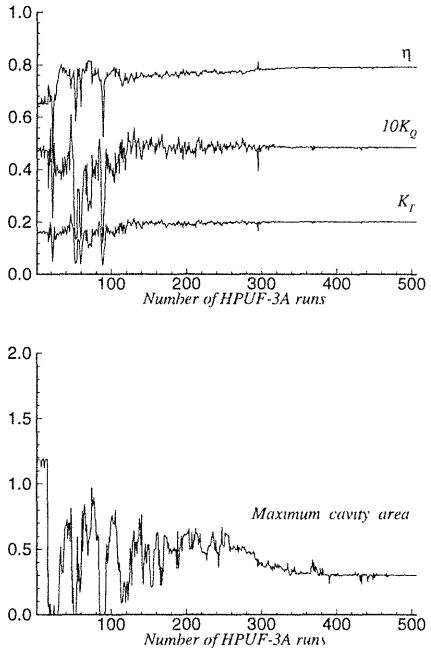

Figure 6-13: Convergence history of design No. 3 : $SKMAX = 45^o$, $CAMAX = 0.3$, $VVMAX = \infty$, $FAMAX = \infty$

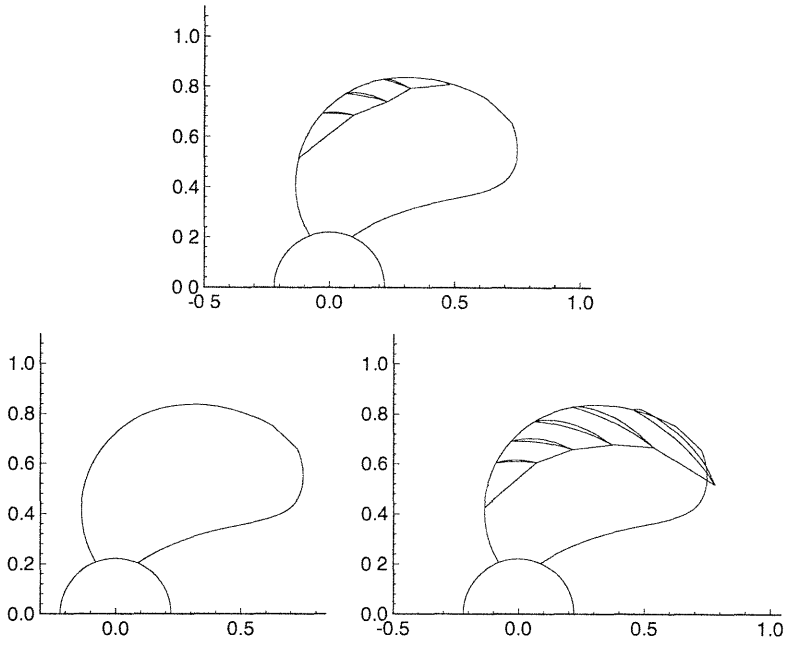

Figure 6-14: Cavity shapes for design No. 4 , Blade angle $\theta = 318^o, 0^o, 42^o$ from left to right : $SKMAX = 45^o$, $CAMAX = 0.3$, $VVMAX = 0.007$, $FAMAX = \infty$

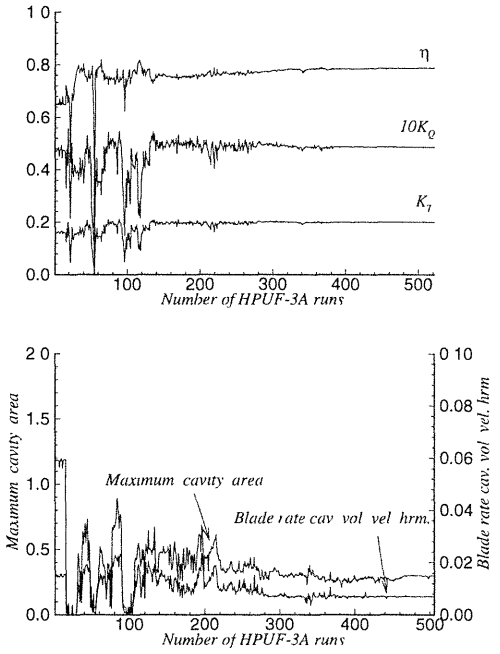

Figure 6-15: Convergence history of design No. 4 : $SKMAX = 45^o$, $CAMAX = 0.3$, $VVMAX = 0.007$, $FAMAX = \infty$

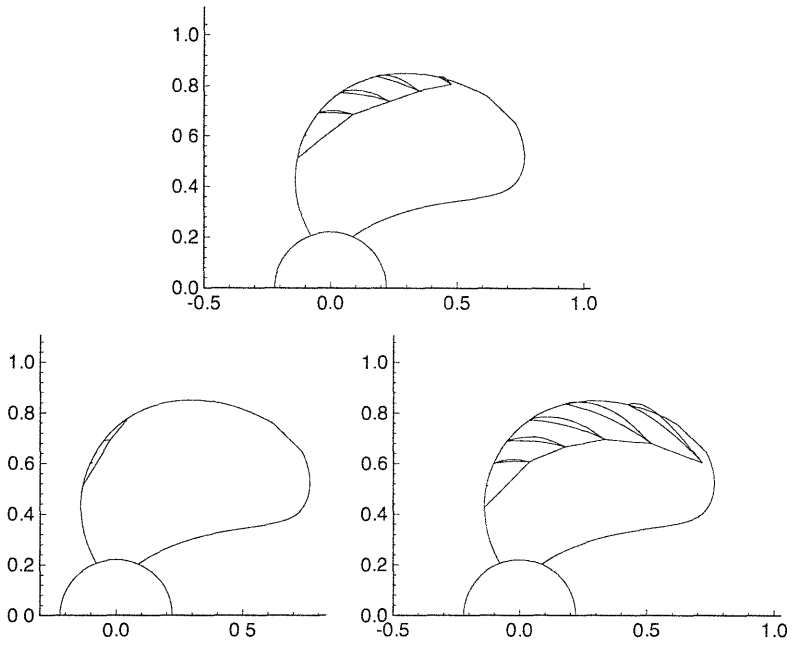

Figure 6-16: Cavity shapes for design No. 5 , Blade angle $\theta = 318^o, 0^o, 42^o$ from left to right : $SKMAX = 45^o$, $CAMAX = 0.3$, $VVMAX = 0.007$, $FAMAX = 0$

$$\begin{aligned} SKMAX &= 45^o \\ CAMAX &= 0.3 \\ FAMAX &= \infty \\ VVMAX &= 5 \times 10^{-3} \end{aligned} \tag{6.5}$$

The initial and resulting blade geometries are shown in Figure 6-19 and the cavity volume history during one propeller revolution is shown in Figure 6-20. The resulting K_Q from these three runs are in Table 6.2. The iteration history of K_T and K_Q is shown in Figure 6-21. Three different initial K_T and K_Q converged to the almost identical final values.

It appears that the geometries do not differ much, except near the hub and the tip. It is interesting to see that K_Q is very close in all three cases, although the blade geometries are not exactly the same.

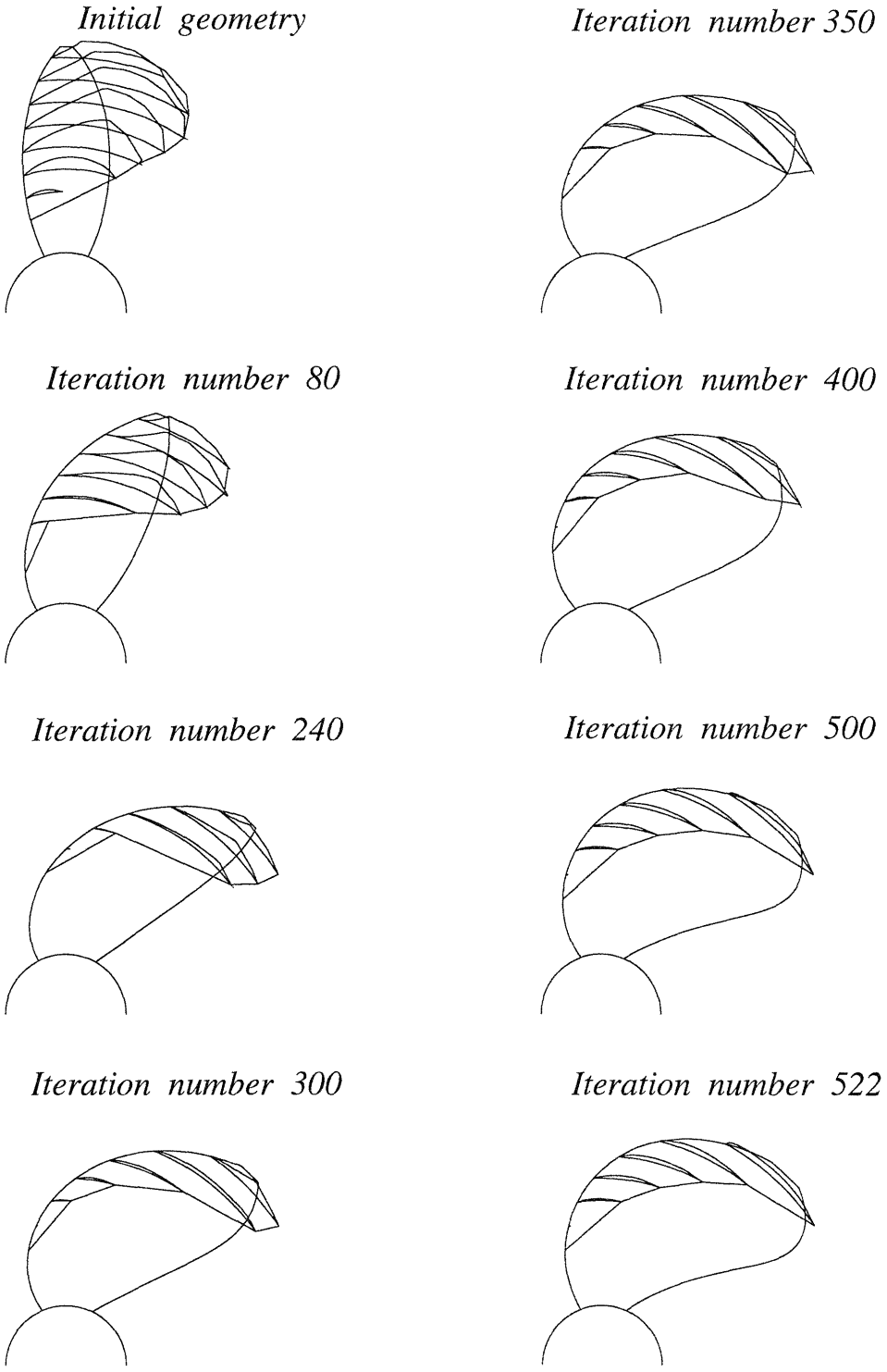

Figure 6-17: Iteration history of cavity shapes of design No. 4 ($\theta = 42^o$) : $SKMAX = 45^o$, $CAMAX = 0.3$, $VVMAX = 0.007$, $FAMAX = \infty$

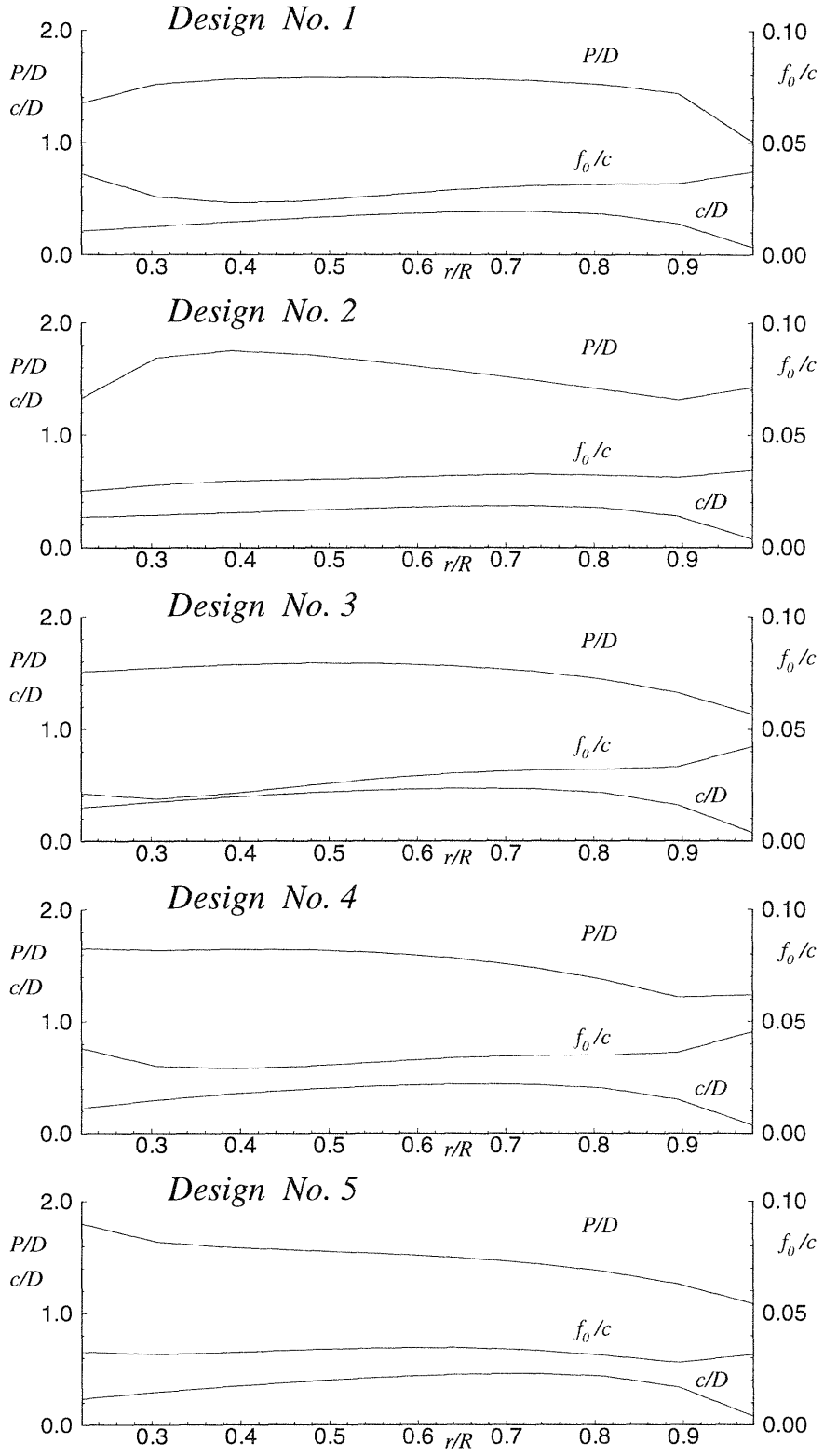

Figure 6-18: Optimum cavitating blade geometries for designs No. 1-5

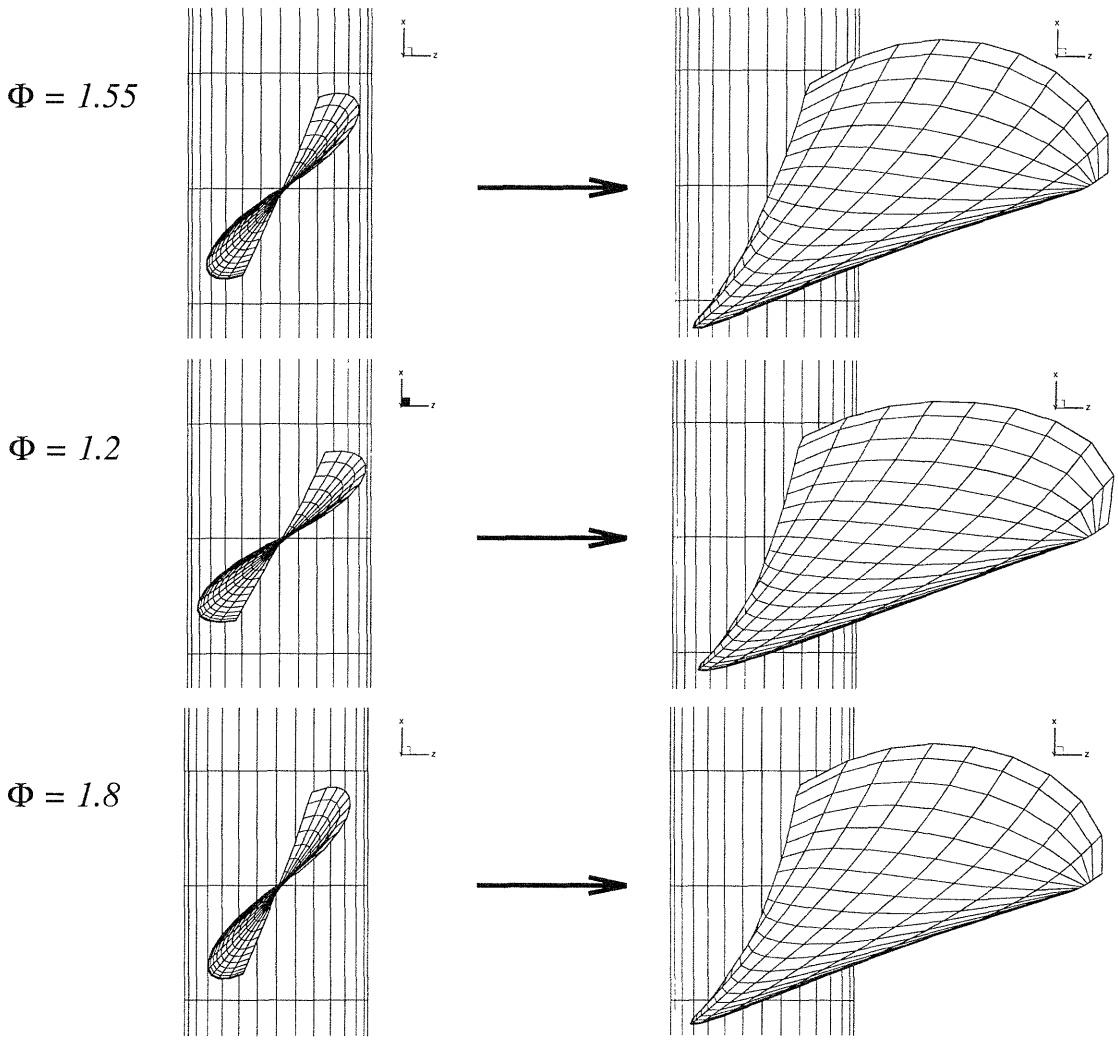

Figure 6-19: Optimum blade geometries from different initial geometries : $SKMAX = 45^o$, $CAMAX = 0.3$, $VVMAX = 0.005$, $FAMAX = \infty$

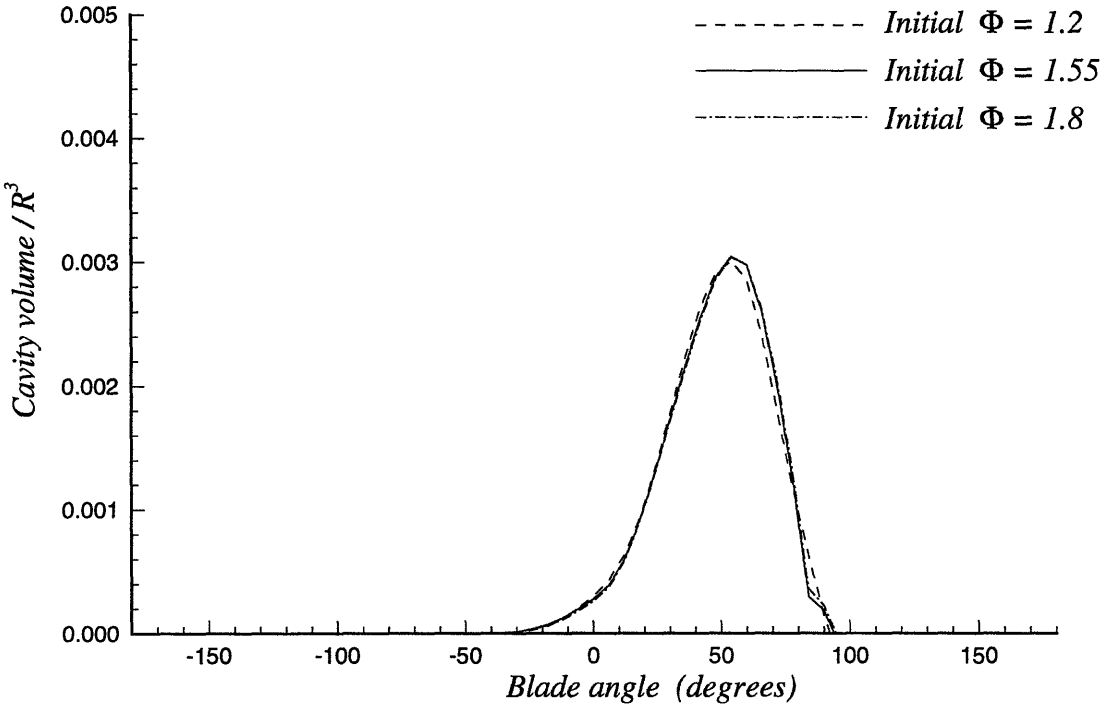

Figure 6-20: Cavity volume history of optimum blade geometries from different initial geometries : $SKMAX = 45^o$, $CAMAX = 0.3$, $VVMAX = 0.005$, $FAMAX = \infty$

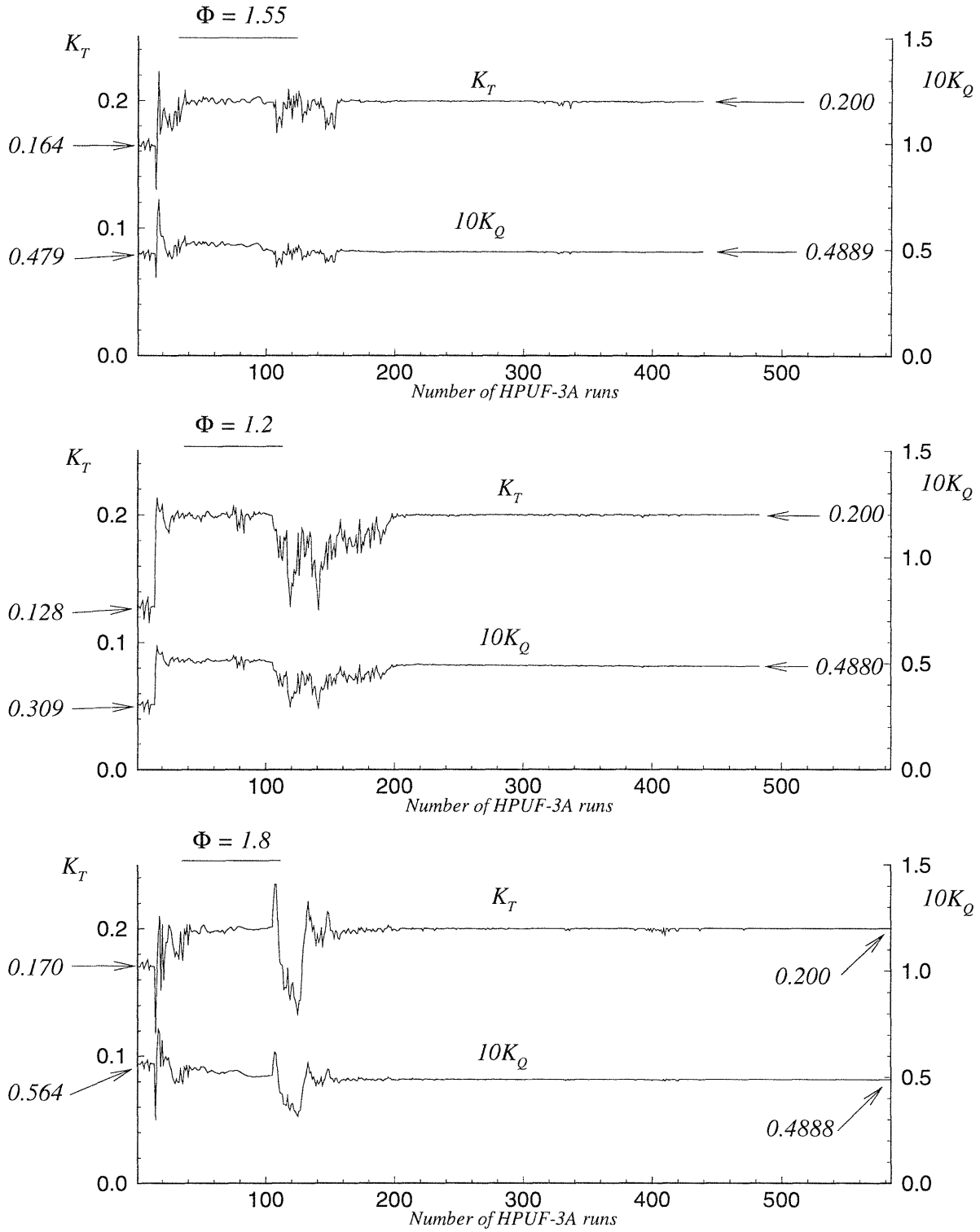

Figure 6-21: Convergence history of K_T and K_Q for different initial geometries : $SKMAX = 45^o$, $CAMAX = 0.3$, $VVMAX = 0.005$, $FAMAX = \infty$

Φ	K_Q
1.20	0.04880
1.55	0.04889
1.80	0.04888

Table 6.2: K_Q resulting from *CAVOPT-3D* for different initial blade geometries

6.3.4 Torque-Constrained Design

There are cases in propeller design where the available torque (power) is given and the maximum thrust (ship speed) is maximized. If lifting line theory were used to determine the optimum circulation distribution, the thrust-constrained problem and the torque-constrained problem would give the identical circulation [10].

Using the present method, the thrust-constrained problem was first solved. Then taking the resulting K_Q as the available torque, the torque-constrained problem was solved. The blade geometries and cavity volume histories from the two problems are shown in Figures 6-22 and 6-23, respectively. The iteration history of K_T and K_Q is shown in Figure 6-24. Starting from the same initial blade, the forces for the two problems converged to the same values, taking different iteration paths. The resulting blade geometries are slightly different. However, the cavity volume histories are very close since the same cavity constraints are imposed in the two designs.

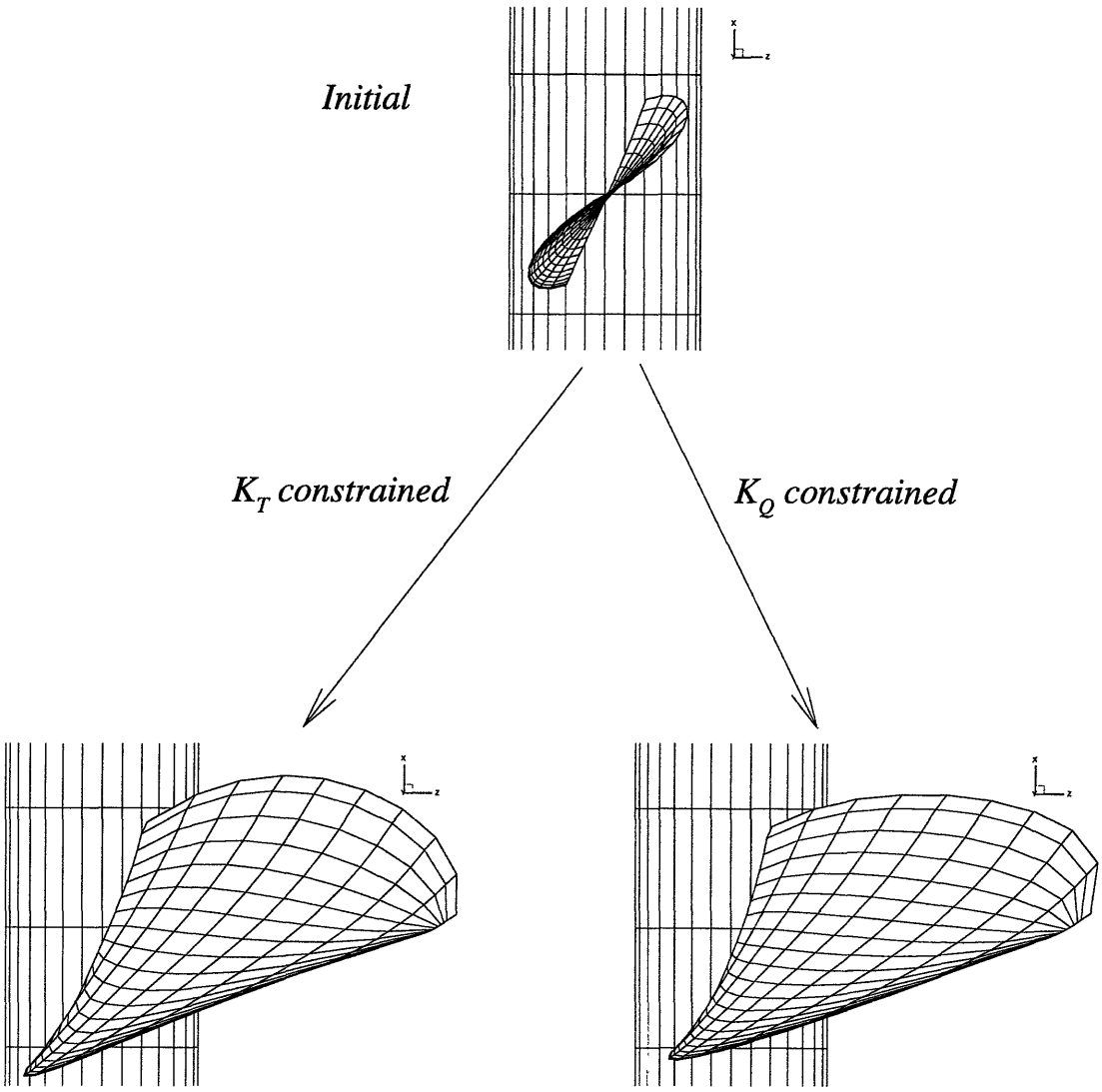

Figure 6-22: Optimum blade geometries from K_T-constrained and K_Q-constrained problems : $SKMAX = 45^o$, $CAMAX = 0.3$, $VVMAX = 0.005$, $FAMAX = \infty$

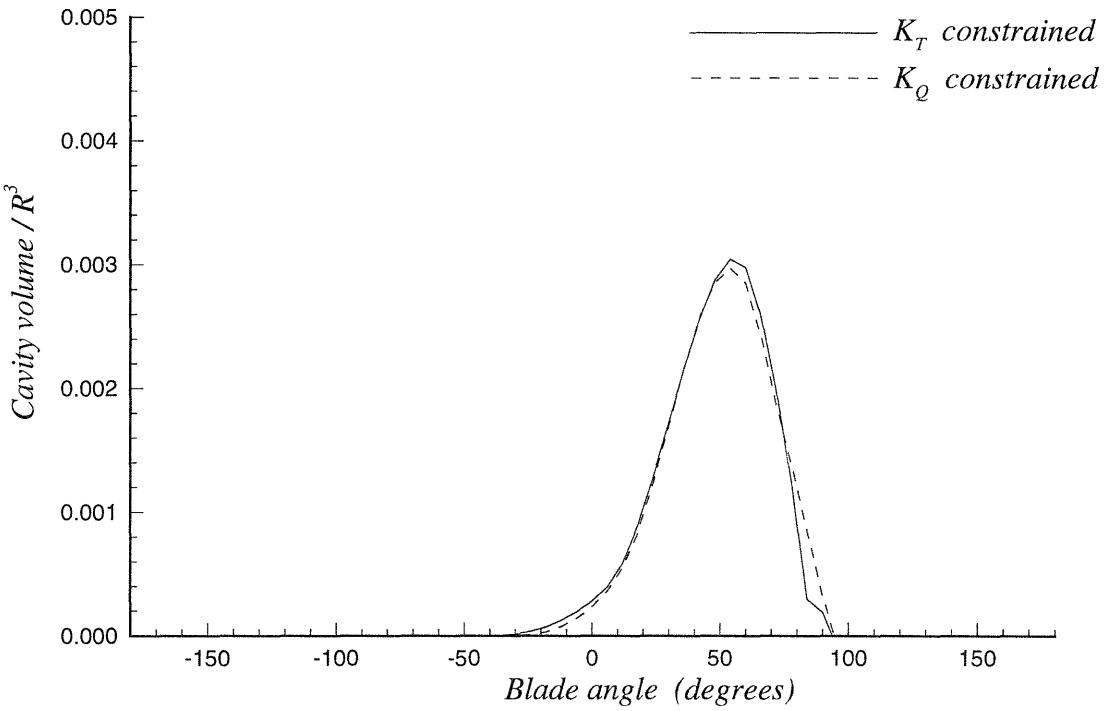

Figure 6-23: Cavity volume history for optimum blade geometries for K_T-constrained and K_Q-constrained problems : $SKMAX = 45^o$, $CAMAX = 0.3$, $VVMAX = 0.005$, $FAMAX = \infty$

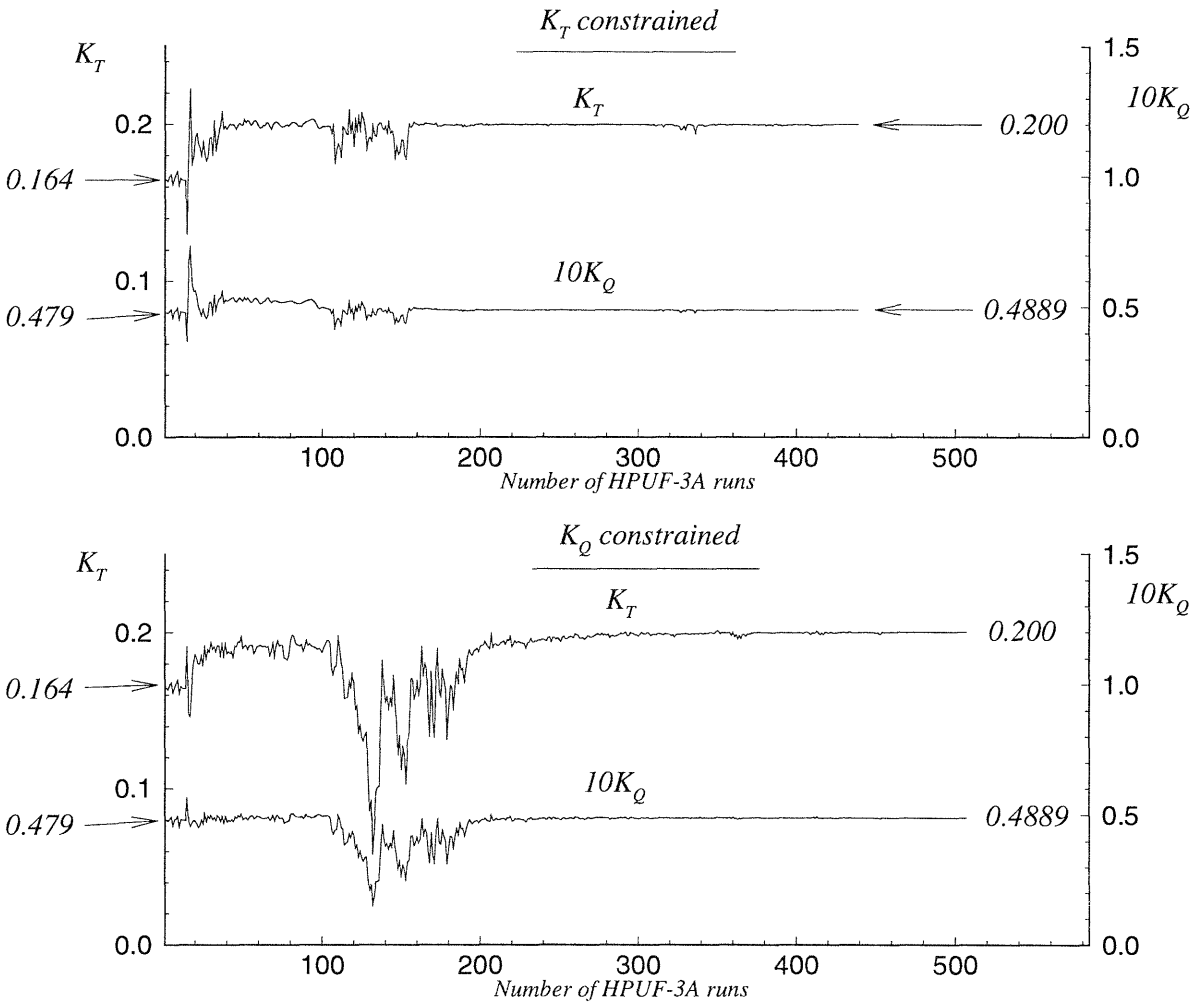

Figure 6-24: Convergence history of K_T and K_Q for K_T-constrained and K_Q-constrained problems : $SKMAX = 45^o$, $CAMAX = 0.3$, $VVMAX = 0.005$, $FAMAX = \infty$

Chapter 7

Conclusions and Recommendations

In this chapter, some conclusions on the work accomplished in this thesis are made and recommendations regarding future research for possible improvements are given.

7.1 Conclusions

In this thesis, a numerical optimization algorithm is developed for the *automated systematic design* of cavitating blades.

The present method, designated as *CAVOPT-3D*, couples a numerical optimization technique with an existing vortex and source lattice method for the analysis of cavitating flows, designated as *HPUF-3A*.

The optimization part employs the method of multipliers, which combines the Lagrangian duality method and the penalty function method. The method can handle general non-linear functions with arbitrary number of both equality and inequality constraints. It has been shown to be efficient and robust when applied on some known test problems.

In the flow analysis part, the blade mean camber surface is defined by a cubic B-spline polygon net in order to facilitate the handling of the geometry, and to reduce the number of design variables (parameters). The B-spline representation of

the blade is shown to approximate a given blade geometry well with a relatively few number of vertices.

In the method developed, the objective and constraint functions are expressed in terms of the design variables, which are the movements of the B-spline vertices. Linear approximations of the results from the analysis method are used in the first stage of the algorithm, and quadratic approximations are used in the final stage. These polynomial approximations are updated at every iteration towards the optimum solution. For each updated solution, this algorithm requires only one function evaluation, which corresponds to one analysis program run, compared to $1 + n$ runs required typically by gradient-based optimization methods.

The present method has been validated extensively by applying it to several known test functions.

The method is first applied to the design of two-dimensional partially and supercavitating hydrofoil sections. The effect of the parameters used in the algorithm on the solution is extensively investigated for the two-dimensional cavitating hydrofoil problems.

Then, the method is applied to the design of three-dimensional propeller blades in uniform flow. The radial circulation distribution obtained by the present method is shown to be consistent with the optimum circulation distribution given by a variational approach based on a lifting line model. The corresponding blade geometry and the pressure distribution on the blade are compared with that determined by using an existing lifting-surface inverse approach.

Finally, the method is applied to the design of cavitating blades in non-uniform flow. The blade geometry, including the blade area and the chord length distribution along the radial direction, is determined by the method to maximize the propeller efficiency by allowing *controlled* amounts of sheet cavitation. Upper bounds on the maximum cavity planform area and the amplitudes of the cavity volume velocity harmonics are incorporated in the optimization algorithm via inequality constraints. The effect of these unsteady cavity constraints on the blade geometry and the corresponding propeller efficiency is shown.

7.2 Recommendations

Some suggestions on the future research related to the present work are given in this section.

Flow analysis method

As stated previously, any improvements in the flow analysis method, *HPUF-3A*, can be easily incorporated.

- *Supercavitating propeller*

Although *HPUF-3A* can treat both partial and supercavitation, it is primarily intended for partial cavities and/or short supercavities. Recently, it was modified to work for supercavitating sections that have a finite trailing edge thickness [45]. Furthermore, the length of the transition wake is extended to allow for a longer supercavity. If a supercavitating propeller for a higher ship speed is to be designed with the present algorithm, further improvements on the modeling of the supercavities will be necessary.

- *Cavity detachment point*

HPUF-3A assumes that the cavity always starts at the leading edge of the blade. This may cause a negative cavity thickness near the leading edge, as shown in Figure 7-1.

This implies that in reality the cavity detaches aft of the leading edge of the blade. Since it is well known that the location of the cavity detachment point may affect the predicted cavity extent, a variable cavity detachment model is desirable for more accurate prediction. For two-dimensional hydrofoils, Franc and Michel [22] found experimentally that the cavity detachment occurs immediately downstream of a laminar separation point. A laminar separation point may be predicted by a strip-wise application of a boundary layer/inviscid flow coupling cavitating flow solver, for

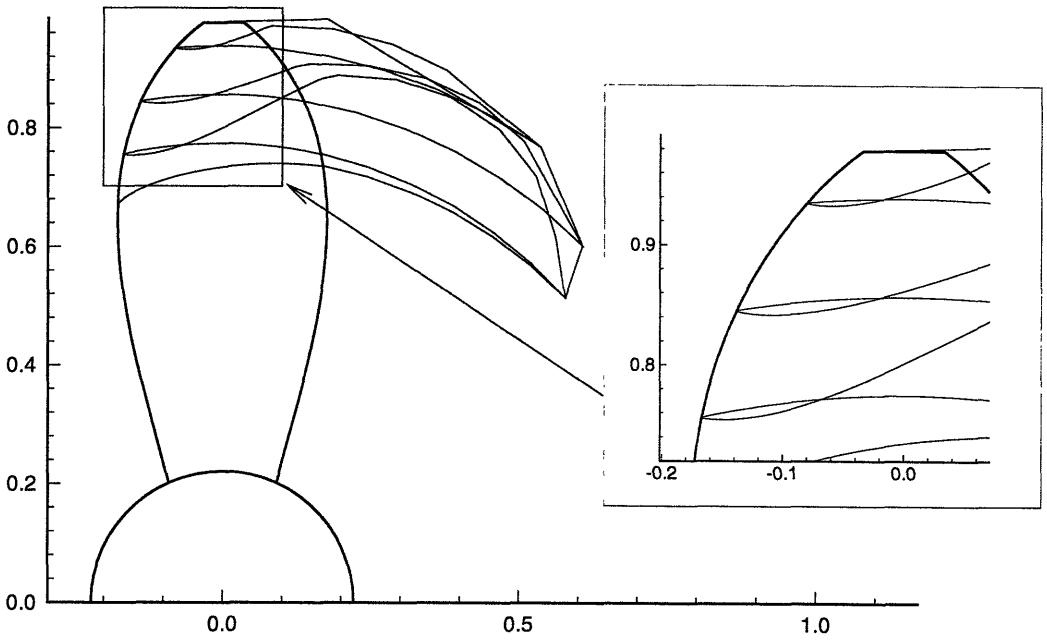

Figure 7-1: Negative cavity thickness near the leading edge of the blade

example developed by Kinnas et al [42]. For a non-cavitating propeller application, this was done by Hufford et al [28].

- *Panel method*

HPUF-3A is attractive for its computational efficiency. However, when faster computers become available, a better modeling of the cavity flow by the panel method, for example PROPCAV by Fine [21], will eventually replace the vortex-lattice method. If one desires to model tip vortex cavitation accurately, panel methods must be used.

Optimization

- *Inclusion of more physical constraints*

Some additional physical constraints which will improve the performance of the current method are:

Unsteady forces acting on the propeller shaft and on the propeller blades

All these quantities are direct outputs from *HPUF-3A* in the form of harmonic coefficients. Depending on the relative importance of each force component to another (e.g. consideration of resonance frequencies of the shaft system), constraints on the weighted sum of the unsteady forces may be imposed.

Margin of the minimum pressure at mid-chord of the blade section

In order to avoid mid-chord/bubble cavitation, a constraint on the margin of the minimum pressure at mid-chord to the cavitation number may be imposed.

Suppression of developed tip vortex cavitation

One possible way of avoiding developed tip vortex cavitation is to impose a constraint on the cavity shape at the tip. The constraint would require that the cavity size decrease towards the tip.

- *Multi-point optimization*

In the present work, optimization is performed for one design condition. For most ship propeller designs, this will be sufficient. However, the overall performance for various operating conditions may not be satisfactory. Drela [16] used the "two-point" optimization for the minimum drag design of low Reynolds number airfoils to overcome this problem. He defined the objective function as a weighted sum of the C_D values at two C_L operating points. This extension is in fact straightforward and can be implemented easily in the present scheme.

- *Application of the present method to other problems*

The present method may be applied to other optimization problems by replacing *HPUF-3A* by any programs. This was demonstrated for the two-dimensional cavitating hydrofoil design problem.

Appendix A

One-Dimensional Line Search Method

In the Quasi-Newton algorithm, one-dimensional unconstrained minimization method to solve the following problem is required at each iteration.

$$\min_{\alpha_k} f(\boldsymbol{x}_k + \alpha_k \boldsymbol{d}_k), \quad \alpha_k \geq 0 \tag{A.1}$$

Since this one dimensional line search routine is called quite a few times, it must be efficient as well as accurate. From a practical point of view, it is often desirable to sacrifice accuracy in this routine to gain in overall computational efficiency. One of such methods is Armijo's rule and is described below [50].

The idea is that the step length α_k must be reasonably large but not too large. Let us define the functions

$$\theta(\alpha) = f(\boldsymbol{x} + \alpha \boldsymbol{d}) \qquad \alpha \geq 0 \tag{A.2}$$

$$\hat{\theta}(\alpha) = \theta(0) + \alpha\sigma\theta'(0) \qquad \alpha \geq 0 \tag{A.3}$$

for fixed $0 < \sigma < 1$.

A step length $\bar{\alpha}$ is acceptable, if

$$\theta(\bar{\alpha}) \leq \hat{\theta}(\bar{\alpha}) \tag{A.4}$$

This is seen in Figure A-1 as the part below the dashed line. To prevent $\bar{\alpha}$ from being too small, Armijo's rule requires

$$\theta(\sigma\bar{\alpha}) > \hat{\theta}(\sigma\bar{\alpha}) \tag{A.5}$$

This is seen in Figure A-1 for $\sigma = 0.5$.

Numerically, m_k is the first nonnegative integer m for which,

$$f(\boldsymbol{x}_k) - f(\boldsymbol{x}_k + \beta^m \boldsymbol{d}_k) \geq -\sigma\beta^m \nabla f(\boldsymbol{x}_k)^T \boldsymbol{d}_k \tag{A.6}$$

where,

$$\alpha_k = \beta^{m_k} \tag{A.7}$$

Starting from $m = 0$, m is increased by 1 until equation (A.6) is satisfied.

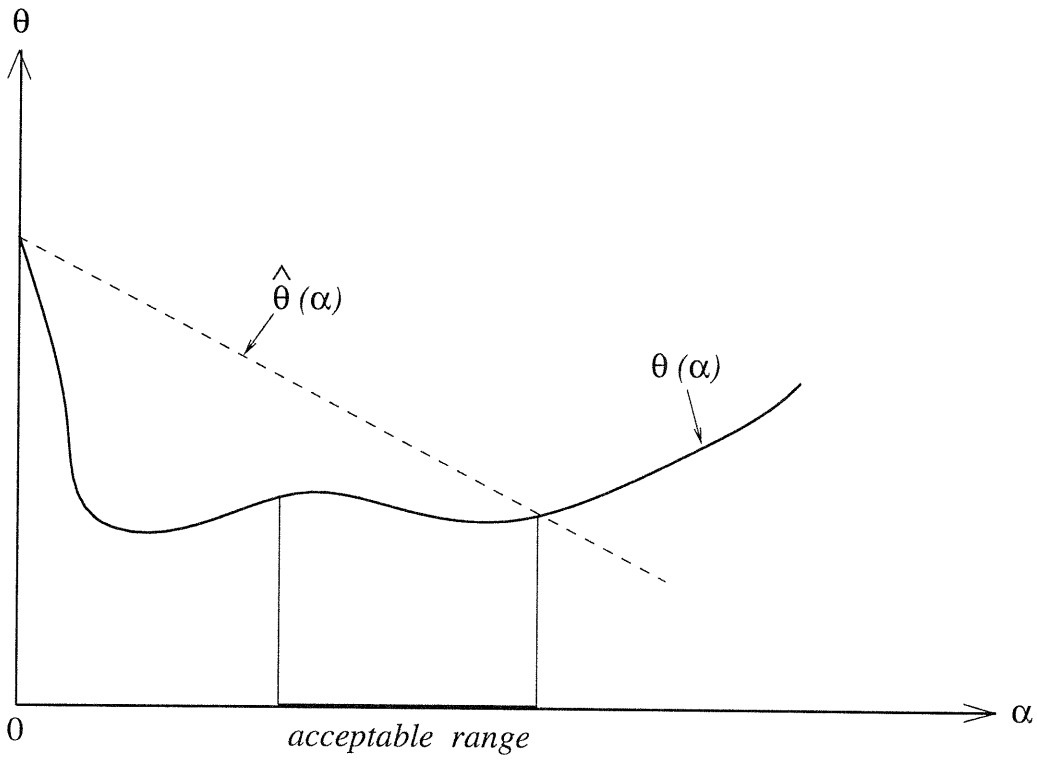

Figure A-1: Acceptable step length in Armijo's rule

Appendix B

Data for the Test Problem

Tabulated data for the test problem No. 2-7 in section 2.5.2 is given in this appendix.

j	1	2	3	4	5	6	7	8	9	10	11	12	13	14	15	16
a_{1j}	1	0	0	1	0	0	1	1	0	0	0	0	0	0	0	1
a_{2j}	0	1	1	0	0	0	1	0	0	1	0	0	0	0	0	0
a_{3j}	0	0	1	0	0	0	1	0	1	1	0	0	0	1	0	0
a_{4j}	0	0	0	1	0	0	1	0	0	0	1	0	0	0	1	0
a_{5j}	0	0	0	0	1	1	0	0	0	1	0	1	0	0	0	1
a_{6j}	0	0	0	0	0	1	0	1	0	0	0	0	0	0	1	0
a_{7j}	0	0	0	0	0	0	1	0	0	0	1	0	1	0	0	0
a_{8j}	0	0	0	0	0	0	0	1	0	1	0	0	0	0	1	0
a_{9j}	0	0	0	0	0	0	0	0	1	0	0	1	0	0	0	1
a_{10j}	0	0	0	0	0	0	0	0	0	1	0	0	0	1	0	0
a_{11j}	0	0	0	0	0	0	0	0	0	0	1	0	1	0	0	0
a_{12j}	0	0	0	0	0	0	0	0	0	0	0	1	0	1	0	0
a_{13j}	0	0	0	0	0	0	0	0	0	0	0	0	1	1	0	0
a_{14j}	0	0	0	0	0	0	0	0	0	0	0	0	0	1	0	0
a_{15j}	0	0	0	0	0	0	0	0	0	0	0	0	0	0	1	0
a_{16j}	0	0	0	0	0	0	0	0	0	0	0	0	0	0	0	1

Table B.1: Data a_{ij} for test problem No. 2-7

j	b_{1j}	b_{2j}	b_{3j}	b_{4j}	b_{5j}	b_{6j}	b_{7j}	b_{8j}	c_j
1	0.22	-1.46	1.29	-1.10	0.00	0.00	1.12	0.00	2.50
2	0.20	0.00	-0.89	-1.06	0.00	-1.72	0.00	0.45	1.10
3	0.19	-1.30	0.00	0.95	0.00	-0.33	0.00	0.26	-3.10
4	0.25	1.82	0.00	-0.54	-1.43	0.00	0.31	-1.10	-3.50
5	0.15	-1.15	-1.16	0.00	1.51	1.62	0.00	0.58	1.30
6	0.11	0.00	-0.96	-1.78	0.59	1.24	0.00	0.00	2.10
7	0.12	0.80	0.00	-0.41	-0.33	0.21	1.12	-1.03	2.30
8	0.13	0.00	-0.49	0.00	-0.43	-0.26	0.00	0.10	-1.50
9	1.00	0.00	0.00	0.00	0.00	0.00	-0.36	0.00	
10	0.00	1.00	0.00	0.00	0.00	0.00	0.00	0.00	
11	0.00	0.00	1.00	0.00	0.00	0.00	0.00	0.00	
12	0.00	0.00	0.00	1.00	0.00	0.00	0.00	0.00	
13	0.00	0.00	0.00	0.00	1.00	0.00	0.00	0.00	
14	0.00	0.00	0.00	0.00	0.00	1.00	0.00	0.00	
15	0.00	0.00	0.00	0.00	0.00	0.00	1.00	0.00	
16	0.00	0.00	0.00	0.00	0.00	0.00	0.00	1.00	

Table B.2: Data b_{ij} and c_j for test problem No. 2-7

Appendix C

Determination of Parametric Spacing for the Blade Geometry

When the propeller mean camber surface is defined by B-splines, the spacings for the parameters, u and w, for the chordwise and spanwise directions, respectively, are determined iteratively so that the resulting physical spacings are the required spacings in *HPUF-3A*.

Suppose that we want NN chordwise by MM spanwise vortex lattice [1], as shown in Figure C-1. Given a B-spline polygon net, a point $\boldsymbol{x}_{ij} = [x_{ij}, y_{ij}, z_{ij}]$ on the blade mean camber surface, may be uniquely defined by specifying the radius, $r_{ij} = \sqrt{y_{ij}^2 + z_{ij}^2}$, and the nondimensional chord length measured from the leading edge, s_{ij} (defined in section 3.2, also in Figure 3-4). Therefore, the problem is to find the parametric spacings, u_{ij} and w_{ij} such that $\boldsymbol{x}_{ij}$ corresponds to the required [2] r_{ij} $(=\mathrm{r}_j)$ and s_{ij} $(=\mathrm{s}_i)$.

A flow chart of the algorithm is shown in Figure C-2.

Step 1 Initially, the parameter values, u_{ij} and w_{ij}, are set equal to the values of the

[1] For another lattice, such as source lattice, the same algorithm works

[2] Although it is not essential, it is assumed in this section that r_{ij} is independent of i and that s_{ij} is independent of j, as shown in Figure C-1.

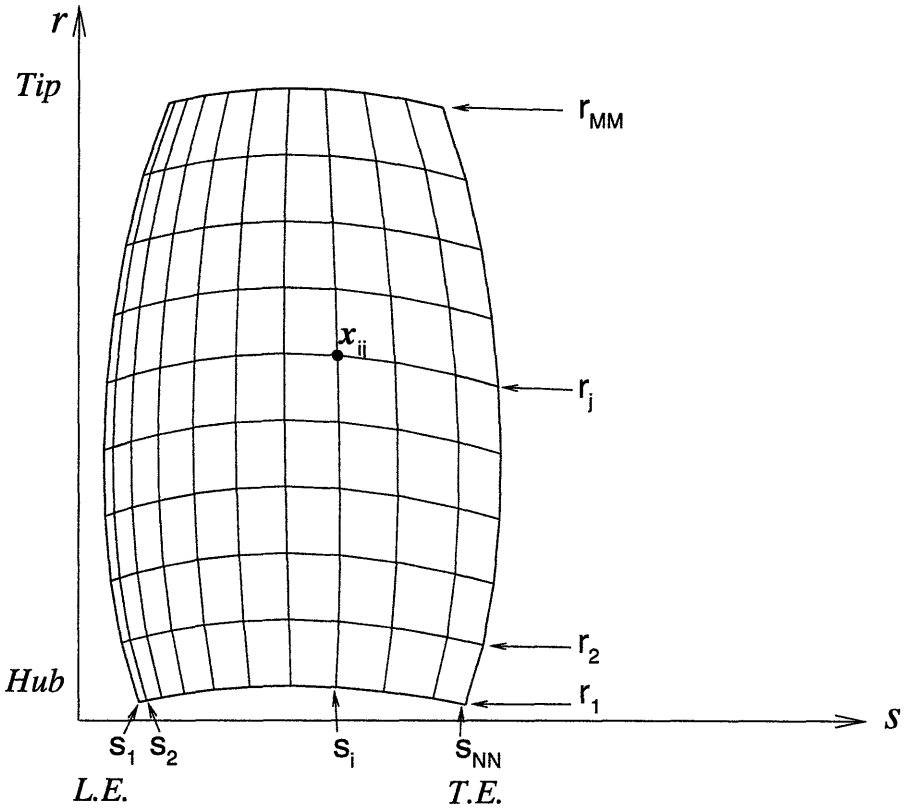

Figure C-1: NN chordwise by MM spanwise vortex lattice

physical spacings:

$$\begin{aligned} u_{ij} &= \mathrm{s}_i \\ w_{ij} &= \mathrm{r}_j \end{aligned} \tag{C.1}$$

In general, this does not give the required spacing in the physical space.

Step 2 For the current u_{ij} and w_{ij}, the corresponding r_{ij} are computed. Then for each spanwise strip i, a cubic spline interpolation of w_{ij} as a function of r_{ij} is

obtained.

$$w_{ij} = \text{spline } w_i(r_{ij}) \tag{C.2}$$

The new w_{ij} is determined by

$$w_{ij} = \text{spline } w_i(\mathrm{r}_j) \tag{C.3}$$

Step 3 For the current u_{ij} and w_{ij}, the corresponding s_{ij} are computed by using equation (3.11). For each chordwise strip j, a cubic spline interpolation of u_{ij} as a function of s_{ij} is obtained.

$$u_{ij} = \text{spline } u_j(s_{ij}) \tag{C.4}$$

The new u_{ij} is determined by

$$u_{ij} = \text{spline } u_j(\mathrm{s}_j) \tag{C.5}$$

Step 4 The convergence of the algorithm is checked by evaluating

$$e = \sum_{i=1}^{NN} \sum_{j=1}^{MM} (r_{ij} - \mathrm{r}_j)^2 + (s_{ij} - \mathrm{s}_i)^2 \tag{C.6}$$

Step 2-4 is repeated until e becomes less than a small specified tolerance (currently equal to 10^{-7}).

A typical convergence history for e is shown in Figure C-3.

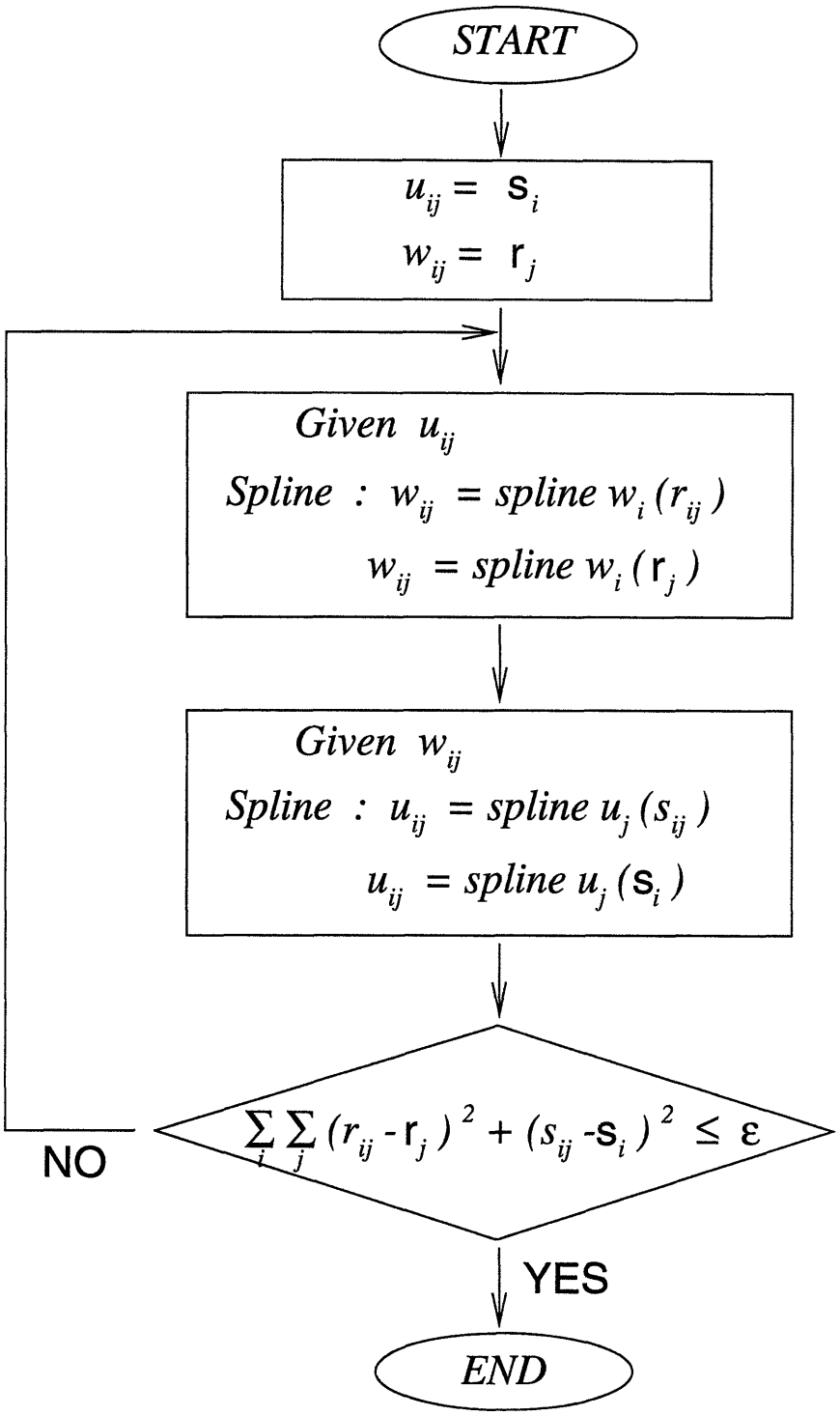

Figure C-2: Flow chart of the iterative method for the determination of u_{ij} and w_{ij}

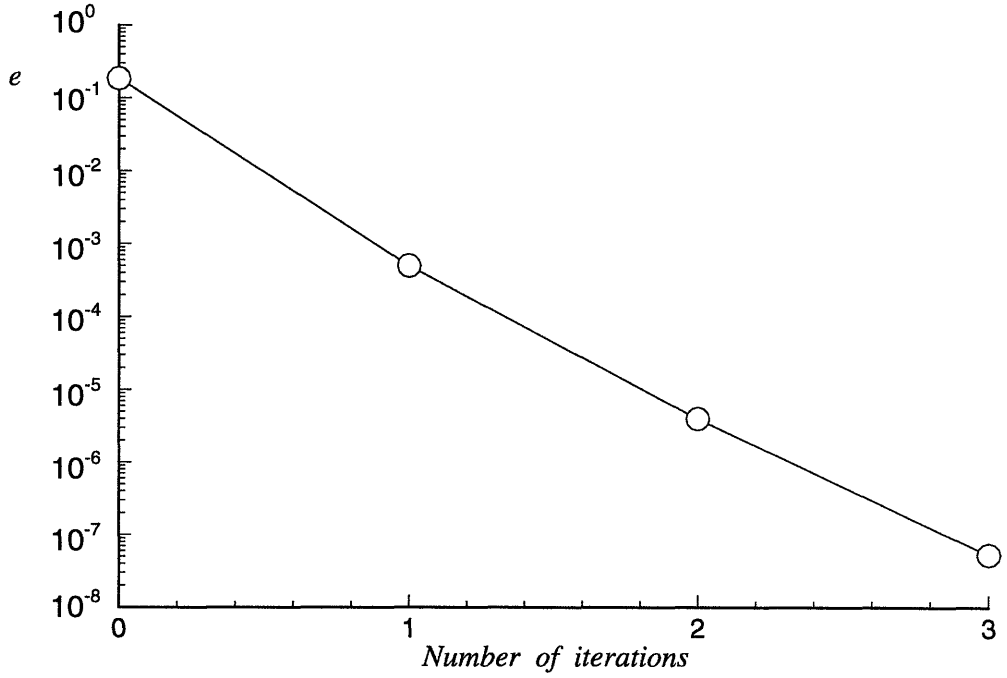

Figure C-3: Typical convergence history of the algorithm : $NN = 20$ chordwise by $MM = 9$ spanwise vortex lattice

Appendix D

B-Spline Vertex Movement

The coordinates of the B-Spline vertices, $\boldsymbol{d}_{I,J} = (x_{I,J}, y_{I,J}, z_{I,J})^T$, corresponding to the design variables using the initial vertices $\boldsymbol{d}^o_{I,J} = (x^o_{I,J}, y^o_{I,J}, z^o_{I,J})^T$, are listed below. The design variables and the vertices movements for 4 by 4 vertices are illustrated in Figure D-1.

1. **Chord length given**

   On the hub $(J = 1)$

$$
\begin{aligned}
x_{1,1} &= x^o_{1,1} + x_{N_u-1}\cos\phi_1 \\
y_{1,1} &= \frac{r_h y^o_{1,1}}{\sqrt{(y^o_{1,1})^2 + (z^o_{1,1} - x_{N_u-1}\sin\phi_1)^2}} \\
z_{1,1} &= \frac{r_h (z^o_{1,1} - x_{N_u-1}\sin\phi_1)}{\sqrt{(y^o_{1,1})^2 + (z^o_{1,1} - x_{N_u-1}\sin\phi_1)^2}}
\end{aligned}
\tag{D.1}
$$

$$
\begin{aligned}
x_{I,1} &= x^o_{I,1} - x_{I-1}\cos\phi_1 \\
y_{I,1} &= \frac{r_h y^o_{I,1}}{\sqrt{(y^o_{I,1})^2 + (z^o_{I,1} + x_{I-1}\sin\phi_1)^2}} \qquad , I = 2, \ldots, N_u \\
z_{I,1} &= \frac{r_h (z^o_{I,1} + x_{I-1}\sin\phi_1)}{\sqrt{(y^o_{I,1})^2 + (z^o_{I,1} + x_{I-1}\sin\phi_1)^2}}
\end{aligned}
\tag{D.2}
$$

Intermediate ($J = 2, \ldots, N_w - 1$)

$$\begin{aligned} x_{1,J} &= x^o_{1,J} + x_{(N_u-1)\times J} \cos\phi_J \\ y_{1,J} &= y^o_{1,J} \\ z_{1,J} &= z^o_{1,J} - x_{(N_u-1)\times J} \sin\phi_J \end{aligned} \tag{D.3}$$

$$\begin{aligned} x_{I,J} &= x^o_{I,J} - x_{(N_u-1)\times(J-1)+I-1} \cos\phi_J \\ y_{I,J} &= y^o_{I,J} \\ z_{I,J} &= z^o_{I,J} + x_{(N_u-1)\times(J-1)+I-1} \sin\phi_J \end{aligned} \tag{D.4}$$

$$, \; I = 2, \ldots, N_u$$

At the tip ($J = N_w$)

$$x_{I,N_w} = x^o_{I,N_w} \cos\left(x_{(N_u-1)\times(N_w-1)+1}\right) + z^o_{I,N_w} \sin\left(x_{(N_u-1)\times(N_w-1)+1}\right) \tag{D.5}$$

$$y_{I,N_w} = \frac{y^o_{I,N_w}}{\sqrt{(y^o_{I,N_w})^2 + \left(-x^o_{I,N_w} \sin\left(x_{(N_u-1)\times(N_w-1)+1}\right) + z^o_{I,N_w} \cos\left(x_{(N_u-1)\times(N_w-1)+1}\right)\right)^2}}$$

$$z_{I,N_w} = \frac{-x^o_{I,N_w} \sin\left(x_{(N_u-1)\times(N_w-1)+1}\right) + z^o_{I,N_w} \cos\left(x_{(N_u-1)\times(N_w-1)+1}\right)}{\sqrt{(y^o_{I,N_w})^2 + \left(-x^o_{I,N_w} \sin\left(x_{(N_u-1)\times(N_w-1)+1}\right) + z^o_{I,N_w} \cos\left(x_{(N_u-1)\times(N_w-1)+1}\right)\right)^2}}$$

$$, \; I = 1, \ldots, N_u$$

2. **Chord length determined**

On the hub ($J = 1$)

$$\begin{aligned} x_{1,1} &= x^o_{1,1} + x_{N_u-1} \cos\phi_1 - x_{N_u} \frac{\sin\phi_1}{2} \\ y_{1,1} &= \frac{r_h y^o_{1,1}}{\sqrt{(y^o_{1,1})^2 + (z^o_{1,1} - x_{N_u-1} \sin\phi_1 - x_{N_u} \frac{\cos\phi_1}{2})^2}} \end{aligned} \tag{D.6}$$

$$
\begin{aligned}
z_{1,1} &= \frac{r_h(z^o_{1,1} - x_{N_u-1}\sin\phi_1 - x_{N_u}\frac{\cos\phi_1}{2})}{\sqrt{(y^o_{1,1})^2 + (z^o_{1,1} - x_{N_u-1}\sin\phi_1 - x_{N_u}\frac{\cos\phi_1}{2})^2}}
\end{aligned}
$$

$$
\begin{aligned}
x_{I,1} &= x^o_{I,1} - x_{I-1}\cos\phi_1 - x_{N_u}\frac{\cos(\pi\frac{I-1}{N_u-1})}{2}\sin\phi_1 \\
y_{I,1} &= \frac{r_h y^o_{I,1}}{\sqrt{(y^o_{I,1})^2 + (z^o_{I,1} + x_{I-1}\sin\phi_1 - x_{N_u}\frac{\cos(\pi\frac{I-1}{N_u-1})}{2}\cos\phi_1)^2}} \\
z_{I,1} &= \frac{r_h(z^o_{I,1} + x_{I-1}\sin\phi_1 - x_{N_u}\frac{\cos(\pi\frac{I-1}{N_u-1})}{2}\cos\phi_1)}{\sqrt{(y^o_{I,1})^2 + (z^o_{I,1} + x_{I-1}\sin\phi_1 - x_{N_u}\frac{\cos(\pi\frac{I-1}{N_u-1})}{2}\cos\phi_1)^2}}
\end{aligned}
\qquad (D.7)
$$

$$, I = 2, \ldots, N_u$$

Intermediate $(J = 2, \ldots, N_w - 1)$

$$
\begin{aligned}
x_{1,J} &= x^o_{1,J} + x_{J\times N_u-1}\cos\phi_J - x_{J\times N_u}\frac{\sin\phi_J}{2} \\
y_{1,J} &= y^o_{1,J} \\
z_{1,J} &= z^o_{1,J} - x_{J\times N_u-1}\sin\phi_J - x_{J\times N_u}\frac{\cos\phi_J}{2}
\end{aligned}
\qquad (D.8)
$$

$$
\begin{aligned}
x_{I,J} &= x^o_{I,J} - x_{(J-1)\times N_u+I-1}\cos\phi_J - x_{J\times N_u}\frac{\cos(\frac{\pi(I-1)}{N_u-1})}{2}\sin\phi_J \\
y_{I,J} &= y^o_{I,J} \\
z_{I,J} &= z^o_{I,J} + x_{(J-1)\times N_u+I-1}\sin\phi_J - x_{J\times N_u}\frac{\cos(\frac{\pi(I-1)}{N_u-1})}{2}\cos\phi_J
\end{aligned}
\qquad (D.9)
$$

$$, I = 2, \ldots, N_u$$

At the tip $(J = N_w)$

$$
\begin{aligned}
x_{I,N_w} &= x^o_{I,N_w}\cos(x_{N_u\times(N_w-1)+1}) + z^o_{I,N_w}\sin(x_{N_u\times(N_w-1)+1}) \\
y_{I,N_w} &= \frac{y^o_{I,N_w}}{\sqrt{(y^o_{I,N_w})^2 + (-x^o_{I,N_w}\sin(x_{N_u\times(N_w-1)+1}) + z^o_{I,N_w}\cos(x_{N_u\times(N_w-1)+1}))^2}} \\
z_{I,N_w} &= \frac{-x^o_{I,N_w}\sin(x_{N_u\times(N_w-1)+1}) + z^o_{I,N_w}\cos(x_{N_u\times(N_w-1)+1})}{\sqrt{(y^o_{I,N_w})^2 + (-x^o_{I,N_w}\sin(x_{N_u\times(N_w-1)+1}) + z^o_{I,N_w}\cos(x_{N_u\times(N_w-1)+1}))^2}}
\end{aligned}
\qquad (D.10)
$$

$$, I = 1, \ldots, N_u$$

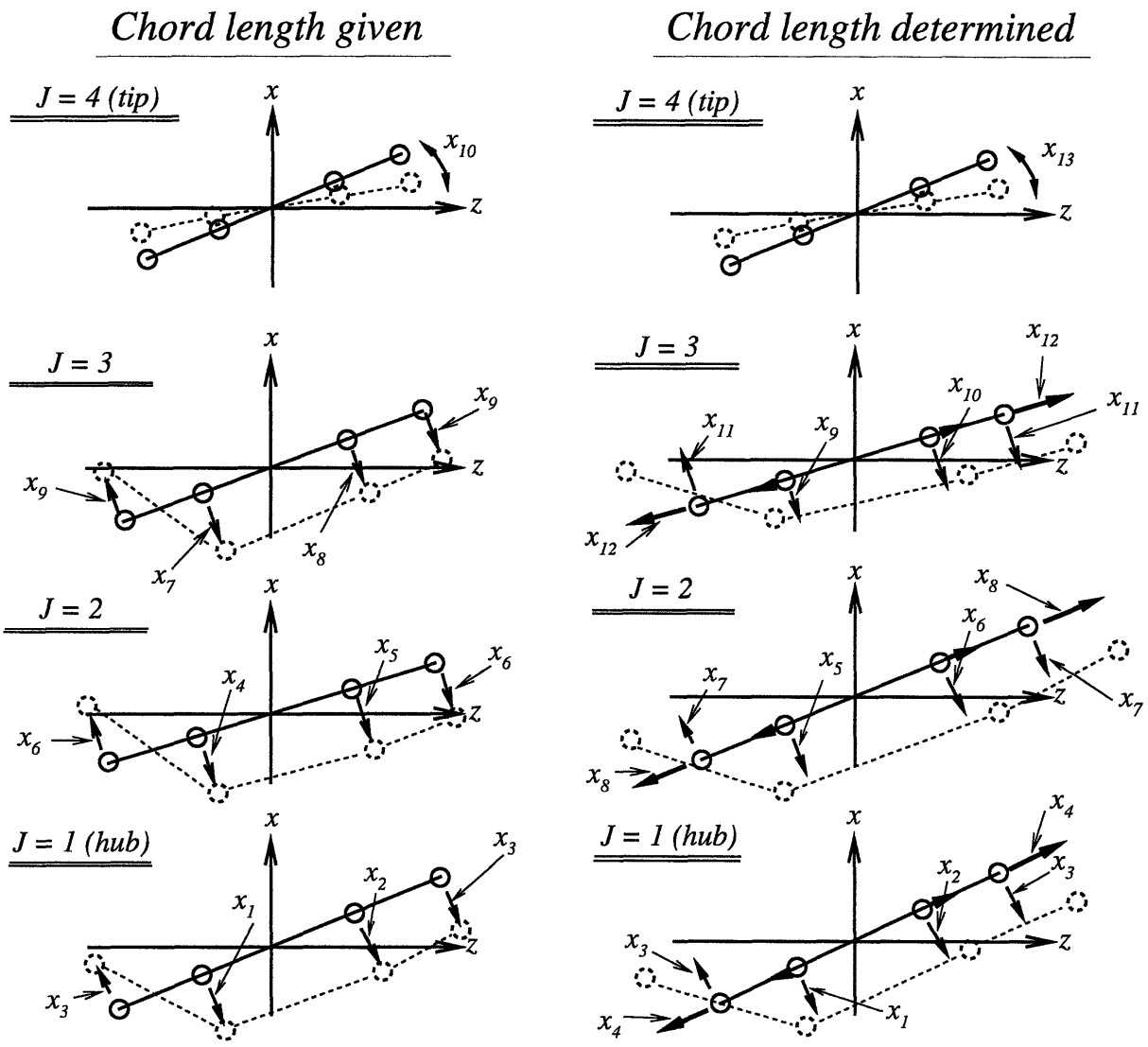

Figure D-1: Design variables and B-spline vertices movement : $N_u = 4, N_w = 4$

Bibliography

[1] I.H. Abbott and A.E. Von Doenhoff. *Theory of Wing Sections.* Dover, New York, 1959.

[2] M.S. Bazaraa, H.D. Sherali, and C.M. Shetty. *Nonlinear Programming.* John Wiley & Sons, Inc., New York, 2nd edition, 1993.

[3] A. Betz. Schraubenpropeller mit geringstem energieverlust. *K. Ges. Wiss. Gottingen Nachr. Math.-Phys. Klasse*, pages 193–217, 1919.

[4] S. D. Black. The Use of Numerical Optimization in Advanced Blade Section Design . In *24th ATTC Proceedings*, Texas, A&M University, College Station, TX, USA, November 2-3 1995.

[5] R. P. Brent. *Algorithms for minimization without derivatives.* Prentice-Hall, Englewood Cliffs, N.J., 1973.

[6] J.P. Breslin, R.J. Van Houten, J.E. Kerwin, and C-A Johnsson. Theoretical and experimental propeller-induced hull pressures arising from intermittent blade cavitation, loading, and thickness. *Trans. SNAME*, 90, 1982.

[7] L. C. Burrill and A. Emerson. Propeller Cavitation - Further Tests on 16in Propeller Models in the King's College Cavitation Tunnel. *Trans. NECI*, 79, 1962-63.

[8] J.P. Comstock, editor. *Principles of Naval Architecture.* Society of Naval Architects and Marine Engineers, 1967.

[9] W. B. Coney. Optimum Circulation Distrubutions for a Class of Marine Propulsors. *Journal of Ship Research*, 36(3):pp. 210–222, September 1992.

[10] W. B. Coney. *A Method for the Design of a Class of Optimum Marine Propulsors.* PhD thesis, Department of Ocean Engineering, MIT, May, 1989.

[11] W.B. Coney. MIT-PLL USER'S MANUAL. Technical report, Department of Ocean Engineering, MIT, November 1988.

[12] C. Dai, S. Hambric, L. Mulvihill, S-S Tong, and D. Powell. A prototype marine propulsor design tool using artificial intelligence and numerical optimization tecniques. *Trans. SNAME*, 102, 1994.

[13] K. de Jong. On the Optimization, Including Viscous Effects, of Ship Screw Propellers with Optional End Plates. In *Proceedings of the Eighteenth Symposium on Naval Hydrodynamics*, pages 585–605, The University of Michigan, Ann Arbor, Michigan, August 19-24 1990.

[14] J.E. Dennis Jr. and Schnabel R.B. *Numerical Methods for Unconstrained Optimization and Nonlinear equations.* Prentice Hall, New Jersey, 1983.

[15] M. Drela. XFOIL: An analysis and design system for low Reynolds number airfoils. In *Lecture Notes in Engineering (Volume 54, Low Reynolds Number Aerodynamics)*, New York, 1989. Springer-Verlag.

[16] M. Drela. Viscous and Inviscid Inverse Schemes Using Newton's Method. *AGARD*, Rep. 9, 1990.

[17] G. S. Dulikravich. Aerodynamic shape design and optimization : Status and trends. *Journal of Aircraft*, 29(6):pp. 1020–1026, Nov-Dec, 1992.

[18] M. K. Eckhart and W. B. Morgan. A propeller design method. *Trans. SNAME*, 63:pp. 325–374, 1955.

[19] R. Eppler and Y. T. Shen. Wing section for hydrofoils - part 1 : Symmetrical profiles. *Journal of Ship Research*, 23(3):pp. 209–217, September 1979.

[20] S. Eyi, J. O. Hager, and K. D. Lee. Airfoil Design Optimization Using the Navier-Stokes Equations. *Journal of Optimization Theory and Applications*, 83(3):pp. 447–461, December 1994.

[21] N. E. Fine. *Nonlinear Analysis of Cavitating Propellers in Nonuniform Flow.* PhD thesis, Department of Ocean Engineering, MIT, October, 1992.

[22] J.P. Franc and J.M. Michel. Attached cavitation and the boundary layer : Experimental investigation and numerical treatment. *Journal of Fluids Mechanics*, 154:pp. 63–90, 1985.

[23] M. B. Giles and M. Drela. Two-dimensional transonic aerodynamic design method. *AIAA Journal*, 25:pp. 1199–1205, 1987.

[24] S. Goldstein. On the vortex theory of screw propellers. In *Proc. R. Soc. London, Ser. A 123*, 1929.

[25] D.S. Greeley and J.E. Kerwin. Numerical methods for propeller design and analysis in steady flow. *Trans. SNAME*, vol 90, 1982.

[26] W. Hock and K. Schittkowski. *Test Examples for Nonlinear Programming Codes.* Springer-Verlag, Berlin, New York, 1981.

[27] T.T. Huang and Groves N.C. Effective wake : Theory and experiment. In *13th Symposium on Naval Hydrodynamics*, Tokyo, October 1980.

[28] G.S. Hufford, M. Drela, and J.E. Kerwin. Viscous flow around marine propellers using boundary-layer strip theory. *Journal of Ship Research*, 38(1):pp. 52–62, March 1994.

[29] V.E. Johnson Jr. Theoretical and Experimental Investigation of Supercavitating Hydrofoils Operating Near the Free Water Surface. Technical Report TR R-93, NASA, 1961.

[30] H. Kamiirisa and D. Aoki. Development of Supercavitating Propeller for Outboard Motors. In *Second International Symposium on Cavitation*, Tokyo, Japan, April 5-7 1994.

[31] J. E. Kerwin, D.P. Keenan, S. D. Black, and J.G. Diggs. A Coupled Viscous/Potential Flow Design Method for Wake-Adapted, Multi-Stage, Ducted Propulsors Using Generalized Geometry. *Trans. SNAME*, 102:pp.23–56, 1994.

[32] J.E. Kerwin. The solution of propeller lifting surface problems by vortex lattice methods. Technical report, MIT, Department of Ocean Engineering, 1961.

[33] J.E. Kerwin. Hydrofoils and propellers, February 1993. Lecture Notes.

[34] J.E. Kerwin, S.A. Kinnas, M.B. Wilson, and McHugh J. Experimental and analytical techniques for the study of unsteady propeller sheet cavitation. In *Proceedings of the Sixteenth Symposium on Naval Hydrodynamics*, Berkeley, California, July 1986.

[35] J.E. Kerwin and C.S. Lee. Prediction of Steady and Unsteady Marine Propeller Performance by Numerical Lifting-Surface Theory. *Trans. SNAME*, 86, 1978.

[36] Y. Kikuchi, H. Kato, H. Yamaguchi, and M. Maeda. Study on a Supercavitating Foil. In *Second International Symposium on Cavitation*, pages 127–132, Tokyo, Japan, April 5-7 1994.

[37] S.A. Kinnas. Leading-Edge Corrections to the Linear Theory of Partially Cavitating Hydrofoils. *Journal of Ship Research*, 35(1):pp. 15–27, March 1991.

[38] S.A. Kinnas and W.B. Coney. The generalized image model - an application to the design of ducted propellers. *Journal of Ship Research*, 36(3):197–209, September 1992.

[39] S.A. Kinnas and N.E. Fine. Non-Linear Analysis of the Flow Around Partially or Super-Cavitating Hydrofoils by a Potential Based Panel Method. In *Boundary Integral Methods-Theory and Applications, Proceedings of the IABEM-90*

Symposium, Rome, Italy, October 15-19, 1990, pages 289–300, Heidelberg, 1991. Springer-Verlag.

[40] S.A. Kinnas and N.E. Fine. A numerical nonlinear analysis of the flow around two- and three-dimensional partially cavitating hydrofoils. *Journal of Fluid Mechanics*, 254:151–181, September 1993.

[41] S.A. Kinnas and S. Mishima. Systematic Design of Optimum Cavitating Sections. In *Second International Symposium on Cavitation*, pages 107–112, Tokyo, Japan, April 5-7 1994.

[42] S.A. Kinnas, S. Mishima, and W.H. Brewer. Non-linear Analysis of Viscous Flow Around Cavitating Hydrofoils. In *Twentieth Symposium on Naval Hydrodynamics*, University of California, Santa Barbara, CA, August 21-26 1994.

[43] S.A. Kinnas, S. Mishima, and C. Savineau. Application of Optimization Techniques to the Design of Cavitating Hydrofoils and Wings. In *The International Symposium on Cavitation*, Deauville, France, May 1995.

[44] K. N. Kramer. Induzierte Wirkungsgrade von Best-Luftschrauben endlicher Blattzahl : English Translation. Technical Report NACA TM 884, NACA, January 1939.

[45] T. Kudo and S. A. Kinnas. Application of Unsteady Vortex/Source Lattice Method on Supercavitating Propellers. In *24th ATTC Proceedings*, Texas, A&M University, College Station, TX, USA, November 2-3 1995.

[46] G. Kuiper and S.D. Jessup. A propeller design method for unsteady conditions. *Trans. SNAME*, 101:pp.247–273, 1993.

[47] C.-S. Lee. *Prediction of Steady and Unsteady Performance of Marine Propellers with or without Cavitation by Numerical Lifting Surface Theory.* PhD thesis, M.I.T., Department of Ocean Engineering, May 1979.

[48] K. D. Lee and S. Eyi. Aerodynamic Design via Optimization. In *17th ICAS Proceedings*, volume 2, pages 1808–1818, 1990.

[49] H. W. Lerbs. Moderately loaded propellers with a finite number of blades and an arbitrary distribution of circulation. In *SNAME Transactions*, volume 60, 1952.

[50] D. G. Luenberger. *Linear and Nonlinear Programming.* Addison-Wesley, Reading, Massachusetts, 2nd edition, 1984.

[51] S. Mishima and S. A. Kinnas. HPUF-3A version 1.1 USER'S MANUAL. Technical Report No. 96-1, Department of Ocean Engineering, MIT, February 1996.

[52] S. Mishima and S.A. Kinnas. A Numerical Optimization Technique Applied to the Design of Two-Dimensional Cavitating Hydrofoil Sections. *Journal of Ship Research*, 40(1):pp. 28–38, March 1996.

[53] W. B. Morgan, V. Silovic, and S. B. Denny. Propeller lifting-surface corrections. *Trans. SNAME*, 76:pp. 309–347, 1968.

[54] M. G. Parsons and J. E. Greenblatt. Optimization of Propeller Skew Distribution to Minimize the Vibratory Forces and Moments Acting at the Propeller Hub. Technical Report No. 206, UM.NAME, December 1978.

[55] N.M. Patrikalakis. Design and implementation of computer-aided engineering systems, 1995. Lecture Notes.

[56] N.M. Patrikalakis and L. Bardis. Feature Extraction from B-spline Marine Propeller Representations. *Journal of Ship Research*, 36(3):pp. 233–247, September 1992.

[57] P.C. Pien. The calculation of marine propellers based on lifting surface theory. *Journal of Ship Research*, 5(2), 1961.

[58] S. Pyo and S. A. Kinnas. HPUF-3AL version 1.0 USER'S MANUAL (same as HPUF-3A Version 1.11). Technical Report No. 96-1, Department of Civil Engineering, University of Texas at Austin, April 1996.

[59] O. Rutgersson. Supercavitating propeller performance. *Publication of SSPA*, 82, 1979.

[60] K. Schittkowski. *More Test Examples for Nonlinear Programming Codes.* Springer-Verlag, Berlin, New York, 1987.

[61] Y. T. Shen. Wing section for hydrofoils - part 3 : Experimental verifications. *Journal of Ship Research*, 29(1):pp. 39–50, March 1985.

[62] Y. T. Shen and R. Eppler. Wing section for hydrofoils - part 2 : Nonsymmetrical profiles. *Journal of Ship Research*, 25(3):pp. 191–200, September 1981.

[63] C.A. Slijper and J.A. Sparenberg. On Optimum Propellers with a Duct of Finite Length II. *Journal of Ship Research*, 14(4):pp. 296–299, December 1970.

[64] J. A. Sparenberg. *Hydrodynamic Propulsion and Its Optimization - Analytic Theory.* Kluwer Academic Publishers, 1995.

[65] J.A. Sparenberg. On Optimum Propellers with a Duct of Finite Length. *Journal of Ship Research*, 13(2):pp. 129–136, June 1969.

[66] A.J. Tachmindji and A.B. Milan. The Calculation of Goldstein Factors for Three, Four, Five, and Six Bladed Propellers. Technical Report 1051, DTMB, 1956.

[67] M.P. Tulin. Supercavitating flows - small perturbation theory. *Journal of Ship Research*, 7(3):pp. 16–37, March 1964.

[68] M.P. Tulin and M.P. Burkart. Linearized theory for flows about lifting foils at zero cavitation number. Technical Report C-638, DTMB, February 1955.

[69] Y. Ukon, T. Kudo, Y. Kurobe, N. Matsuda, and H. Kato. Design of High Performance Supercavitating Propellers Based on a Vortex Lattice Method. In *An International Conference on Propeller Cavitation (PROPCAV '95)*, The University of Newcastle Upon Tyne, England, U.K., May 16-18 1995.

[70] M. Van Dyke. *Perturbation Methods in Fluid Mechanics.* The Parabolic Press, Stanford, California, 1975.

[71] W.P.A. van Lammeren, J.D. van Manen, and M.W.C. Oostveld. The Wageningen B-Screw Series . *Trans. SNAME*, 77, 1969.

[72] G. N. Vanderplaats. Efficient algorithm for numerical airfoil optimization. *Journal of Aircraft*, 16(12):pp. 842–847, December, 1979.

[73] W.S. Vorus and K.W. Mitchell. Engineering of power boat propellers. In *Proceedings of the Propellers/Shafting '94 Symposium*, pages 1–16 (paper No. 12), Virginia Beach, VA, September 20-21 1994. Soc. of Naval Arch. & Marine Engnrs.

[74] F. Yamaguchi. *Curves and Surfaces in Computer Aided Geometric Design.* Springer-Verlag, Berlin, Germany, 1988.

[75] B. Yim. Optimum propellers with cavity-drag and frictional-drag effects. *Journal of Ship Research*, 20(2):pp. 118–123, June 1976.